An Examination of Observed Coronal Structures through Automated Techniques Across Solar Cycle 24

Daniel G Gass

A thesis submitted in partial fulfilment
of the requirements for the degree of
Doctor of Philosophy

Jeremiah Horrocks Institute for Mathematics, Physics and Astronomy
University of Central Lancashire

June 2023

Declaration

Type of Award: Doctor of Philosophy

School: Natural Sciences

I declare that while registered as a candidate for the research degree, I have not been a registered candidate or enrolled student for another award of the University or other academic or professional institution.

I declare that no material contained in the thesis has been used in any other submission for an academic award and is solely my own work.

No proof-reading service was used in the compilation of this thesis.

Daniel G Gass

June 2023

Abstract

The solar corona is an intricate and magnetically dominated plasma environment consisting of closed (eg. active region loops) and open (eg. polar plumes) magnetic structures. Although it is a highly studied portion of the solar atmosphere, little research has been conducted to investigate how the basic nature of coronal structures could vary across an entire solar cycle. While there are numerous studies of specific targeted coronal events, the research outlined in this thesis seeks to broaden the body of evidence by systematically capturing and then analysing a range of coronal structural parameters throughout solar maximum and minimums. The theoretical framework for understanding the parameter distributions of coronal structure was a self-organized criticality (SOC) approach, which predicts certain power law distributions of events given the presence of a non-linear, stochastic, critical process which can be described by the sum of interactions of small-scale elements (such as is expected to be the case for D.C. heating scenarios in the corona). The thesis work involved the development of a modular and scientifically robust algorithm for determining structural details that can be employed upon legacy, current, and future datasets. In this case, COSDA (COronal Structural Detection and Analysis) has been used on four Extreme Ultraviolet (EUV) wavelengths (171, 193, 211 and 304 Å) of the Solar Dynamics Observatory (SDO) Atmospheric Imaging Assembly (AIA) from across Solar Cycle 24 and four EUV wavelengths (171, 195, 285 and 304 Å) of the Solar and Heliospheric Observatory's (SOHO) Extreme ultraviolet Imaging Telescope (EIT) across Solar Cycle 23. Closed magnetic regions (loops) were

examined for both cycles 23 and 24 while open, polar structures (plumes) were also examined using the SDO/AIA datasets. From these investigations, width and positional information was obtained from tens of thousands of coronal structures from within a specially constructed annulus used to control for the effects of differential rotation and image noise.

Width analysis demonstrated the existence of a power law of coronal structural width distributions, whose gradient varied depending on the wavelength, as well as the phase of Cycle 24 in which they were observed. These power law gradients, which ranged from -1.6 to -5.5 in the closed loops and -2.2 to -4.9 in open plumes demonstrated both a changing value depending on the period throughout the solar cycle and the observed wavelength, with the most well populated displaying a resemblance to expected SOC behaviour (-1.5 gradient). These variations may be indicative of change in observational structure formation which are analogous to SOC statistical modelling, such as the ability for reconnection to perturb neighbouring strands being similar to quenching, or varying energy addition mechanisms being more or less stochastic. These results could aid in models of coronal heating and loops/structures by constraining the variables such as width distributions and power law slopes that models would need to be able to replicate for their simulations to be physically accurate.

Coronal structure latitude distributions across Cycle 24 reveal a complex North-South asymmetry. There are more structures detected in the northern hemisphere compared to the southern hemisphere (between 63 to 45 percent of total for closed active region and 68 to 11 percent of open polar regions) while asymmetry indices (defined as the number of northern minus southern structures divided by the total number of structures) lies between 0.26 to 0.45 (closed) and 0.36 to -0.09 (open). Latitude distributions show evidence of two distinct functions of structure latitude versus time for active region loops, as well as latitudinal stratification for plume

populations by wavelength. Across Cycle 23 as seen in EIT, the latitudes of locally normalized coronal intensity peaks generally follow distributions seen in Cycle 24 in closed active and open polar regions, though these profiles were more difficult to discern due to noise, and width distributions were unable to be recovered due to resolution limitations. This indicates that certain latitudinal trends of structure distribution may be characteristic of coronal structure distributions throughout at least two solar cycles.

Future work detailing improvements to the COSDA algorithm, machine learning approaches to data processing, and integrating upcoming datasets such as the EUI of the Solar Orbiter into the body of research are also outlined.

Acknowledgements

I would like to acknowledge Professor Robert Walsh for all of the help and assistance provided through some very interesting times! And would like to give thanks to the Jeremiah Horrocks Institute and the Solar Group for support and suggestions which have contributed to the project. I would also like to acknowledge the University of Central Lancashire for the funding of my PhD and the provision of facilities and resources necessary for the completion of my thesis. I would finally like to thank my family for their continued and ongoing support and understanding, without whom my work would not have been possible.

Chapter 1

Introduction

1.1 Background

1.1.1 Early Sunspot Observations

The Sun has been studied and revered since pre-history, but it is only within the last two to three centuries that the extreme physics which governs our closest star has been explored, and the impacts and risks associated with its phenomena have only grown more compelling. The effects and mechanisms surrounding the Sun and its atmosphere are some of the most important unresolved problems in astronomy, and the exact nature governing the outwardly manifesting phenomena of solar activity is still unknown.

Sunspots were the most obvious outwards manifestation of those internal systems available for human observation, now known to be caused by the presence of strong magnetic field emergence inhibiting convection processes in an area of the photosphere. The first recorded human description of sunspots occurred in the 10th century BC in ancient Zhou Dynasty China, documented in the I Ching manuscript (Xu, 1980) with the first confirmed direct observation of sunspots and other geomagnetic phenomena recorded in the 4th century BC (Schove & Peng-Yoke, 1967).

Further works by medieval Islamic and European scholars (Vaquero, Gallego & García, 2002) confirmed the presence and irregular shapes of sunspots, though these were widely thought to be shapes transiting the Sun by occulting bodies. In the 17th century, Johannes Fabricius described sunspots as occurring upon the solar surface, with their evolution ascribed correctly to rotational movements (Fabricius, 1611). Around this time, in 1611, Galileo Galilei also published his now famous account of sunspots as structures appearing on the surface, part of his wider works disagreeing with the model of the geocentric universe (Galilei & Drake, 1990) which was prevalent in academic and religious thinking at the time. These early descriptions gave hint as to the nature of the Sun as a body which is not a perfectly solid, radiant sphere but one which experienced distortions and other visible defects.

The next period of understanding of the solar activity cycle was delayed by just under a century by the larger Maunder (Hoyt & Schatten, 1998) and lesser Daunton (Silverman, Sam M. & Hayakawa, Hisashi, 2021) Minimums, which began towards the end of the seventeenth century and proceeded until roughly the fortieth year of the eighteenth century. During this period, sunspot observations were exceedingly rare, and little could be inferred from their sporadic appearance. After this period, from the mid 19th century onwards, sunspot activity began to rise again, and more specific observations could be made regarding their appearance. Samuel Schwabe developed the first functional description of the Solar Cycle (Schwabe, 1844) in 1844, an important milestone in human understanding of the processes which governed the appearance and behaviour of the Sun.

It was just over a decade after the description of the solar cycle, in 1859, that the Carrington Event occurred (Carrington, 1859, 1863). This was the largest geomagnetic storm in modern history, estimated to be caused by an X-45 class flare, which would be the highest intensity flare yet observed or evaluated (Cliver, Edward W. & Dietrich, William F., 2013). The impact this had on the developing infrastructure

and the growing understanding of the forces of electromagnetism within this period firmly established the role that the Sun and space weather has had and continues to have on our planet, and the need for understanding the atmosphere of the Sun as an object governed by immense magnetic activity.

1.1.2 Spectral Analysis

In 1800, William Herschel inadvertently discovered the existence of the infrared wavelengths by means of splitting sunlight with a glass prism (Ring, 2000). This experiment was followed shortly thereafter by the work of Johan Ritter, who in 1801 discovered the existence of Ultra-Violet light in a similar manner to Herschel's experiment (Frercks, Weber & Wiesenfeldt, 2009). These and other works eventually formed our understanding of the electromagnetic spectrum, as first described by James Maxwell in his 1865 publication "A Dynamical Theory of the Electromagnetic Field" (Clerk Maxwell, 1865).

The development of more powerful prisms spurred new investigation into the components of sunlight, and the discovery of emission lines corresponding to known elements in solar spectra in 1814 by Joseph Fraunhofer (Fraunhofer, 1814) followed. This demonstrated the viability of spectral analysis for solar phenomena, a technique which would become crucial for examination of specific components of the solar atmosphere in future works.

Analysis of combined spectra of the Sun lead to the discovery of the element Helium and the presence of Sodium in 1868 and 1879 by Jules Janssen and Norman Lockyer respectively (Nath, 2012; Lockyer, 1879). The later invention of the spectroheliograph in 1890 and 1891 independently by George Ellery Hale and Henri-Alexandre Deslandres respectively (Millochau & Stefánik, 1906) allowed for detailed analysis of the Sun by isolating different spectral lines. This novel analysis of specific

wavelengths of light as a means to examine individual components of the solar atmosphere paved the way for analysis of different temperature regimes and altitudes within the solar atmosphere, which along with earlier analyses of solar eclipses hinted at the presence of a rarefied, stratified solar atmosphere.

This was studied further in the late 19th and early 20th century, where green light emitted in the corona was mistaken as the emission line of an undiscovered element dubbed "coronium" (Gruenwald, 1887). It was discovered in 1939 by Walter Grotrian (Grotrian, 1939) and in 1942 by Bengt Edlén (Edlén, 1943) that this light was actually emitted by Fe XIII ions, ionisation which would require coronal plasma to be heated to the order of 10^6 Kelvin, far beyond the temperatures expected by contemporary models of the solar atmosphere. This confirmed the existence of the superheated solar corona and began the study of coronal heating, which first came to be described in terms of Magneto-Hydrodynamics (MHD) and wave motions by Hannes Alfén in 1942(Alfvén, 1942; Peter & Dwivedi, 2014), which continues to be the basis for most descriptions of coronal phenomenon and an active area of interest in solar physics to this day.

1.1.3 Modern Efforts

Modern analysis of the Sun has had a firm focus on the outward manifestation of solar phenomena, and the interaction between the solar atmosphere, the interplanetary medium and the Earth's own magnetic field, and the role played by differing layers of the solar atmosphere. Helioseismology has also allowed an understanding of the internal mechanisms, once hidden from direct observations, to be analysed by means of studying small oscillations on the solar surface allowing a deeper understanding to be attained for inner structure in both the Sun and stars elsewhere (Aerts, Christensen-Dalsgaard & Kurtz, 2010). Furthering direct observation of the solar atmosphere has been primarily driven by rocket and space-based missions,

satellites launched with suites of in-situ and telescopic instruments capturing data otherwise impossible to infer from ground-based observations due to the Earth's atmosphere and rotation.

The first space-based heliospheric observation mission was Explorer-10, launched by NASA in March of 1962 as part of the Explorer program to study the effect of solar flares in a near Earth orbit with in situ magnetometers and plasma probes. (Williams, 2022). This was followed by more sophisticated instrument missions, such as the Skylab space station (Garriott, 1974), a crewed science mission in low earth orbit which performed a number of low gravity experiments and space based observing campaigns, including X-Ray, Radio, visible light and EUV observations of the Sun using the eight telescopes in the Apollo Telescope Mount (Ise & Cagle, 1974). After this, further unmanned missions such as the Ulysses space probe, which recorded in situ measurments of solar wind speeds, magnetic field strengths, and solar energetic particles (Bame et al., 1992); the Solar and Heliospheric Observatory (SOHO) mission(Domingo, Fleck & Poland, 1995), which provided a wide array of EUV, X-Ray and in-situ measurements of the solar corona and outer atmosphere and magnetosphere with eleven instruments across twenty six years of observations ; Yohkoh (Solar-A) (Švestka & Uchida, ????) and its follow up Hinode (Solar-B) (Kosugi et al., 2007), instruments which continued the work of Skylab to provide coverage of the X-Ray and EUV corona in a geocentric orbit, proving many novel science results due to the use of CCD detectors and wireless telemetry of data. These were followed by the Transition Region and Coronal Explorer (TRACE) mission (also part of the Explorer program) which provided some of the first high resolution (0.5 arcsec per pixel) limited field images of coronal loops in visible, lyman-alpha, and EUV (Handy et al., 1999) to name just a few of the recent historical solar data missions.

Missions still involved in cutting edge scientific research include the High Resolution Coronal Imager (Hi-C) sounding rocket missions I and III, which have provided the highest ever resolution images recorded of the solar corona (0.1 arcsec per pixel) in EUV wavelengths and is invovled in many studies of the finest scale structures of the corona (Kobayashi et al., 2014). Additionally, the Solar Dynamics Observatory (SDO) (Pesnell, Thompson & Chamberlin, 2012), further outlined below, has been one of the most extensive solar missions ever launched, with ten optical, EUV and X-ray telescopes as part of the Atmospheric Imaging Assembly recording synoptic image data at 0.6 arcsecond per pixel resolution, as well as information on magnetic fields and helioseismology from the Helioseismic and Magnetic Imager (HMI instrument) and the Extreme Ultraviolet Variability Experiment (EVE instrument) which measures EUV irradiance in situ. This mission produces roughly 1.5 terabytes of data per day, and is currently the leading source for bulk image data for the solar atmosphere. The most recent mission is the Solar-Orbiter (Müller et al., 2020a), which consists of both heliospheric in-situ instrumentation and remote sensing imaging instruments. Launched in February of 2020, its objectives include fine resolution coronal imaging, investigation of the heliosphere, and aiding examination of the solar dynamo, on a mission which will take it as close as 0.28 AU from the Sun, and that will last until at least 2027.

1.2 Solar Cycles and Magnetic Activity

The eleven year solar cycle is considered to be a fundamental property of the sun's magnetic dynamo, part of the larger twenty two year magnetic cycle which is the amount of time required for the sun to reverse its magnetic polarity and back again (Müller et al., 2020b). The specifics of its internal mechanisms and its propagation to observable features of solar activity are still poorly understood (Liu et al., 2019).

The level of activity within a cycle has significant consequences for the impact of

space weather on the Earth's magnetic field. There exists a high degree of correlation between the level of solar activity and the frequency of highly energetic events such as flares and coronal mass ejections (Owens et al., 2021), and these can cause considerable disruption to infrastructure both in space and at ground level if they coincide with the position of the Earth (Eastwood et al., 2017). As of yet, no reliable means of accurately predicting the intensity of upcoming solar cycles has been produced (Yeates, Nandy & Mackay, 2008). This can cause complications when a solar cycle is more intense than predicted, as is apparently the case for Cycle 25. Predictions of solar cycle intensity can frequently be incorrect, such as a prediction of Cycle 24 made using geomagnetic activity indices, which predicted a high amplitude cycle (Hathaway & Wilson, 2006), whereas the cycle in reality was very low in amplitude compared to previous cycles. There have been some successful attempts at predicting the early stages of Cycle 25, such as those based upon predictions of Hale Cycle terminations, a sudden decrease of equatorial bright spots (McIntosh, Leamon & Egeland, 2023).

Several trends and relations tied to the magnetic solar cycle exist within sunspots. Examples include Spörer's Law, which dictates the position of appearance of sunspots throughout the solar cycle, initially appearing displaced up to 30 degrees from the solar equator at the start of the solar cycle, and gradually appearing closer and closer as the cycle progresses (Ivanov & Miletsky, 2014). Other examples include Hale's Polarity Law and Joy's Law, which indicates that sunspot pairs appearing within the same hemisphere appear to posses dominant sunspots of the same polarity (Hale & Nicholson, 1925), and that the orientation of those pairs is always with the trailing sunspot further away from the equator (Dasi-Espuig et al., 2010). Spörer's law in particular can be seen in the classic Maunder Butterfly Diagram Maunder (1904), (see Fig 1.1) These are an indicator of some more complex magnetic activity occurring beneath the solar surface which manifests outwardly, relating to the progression

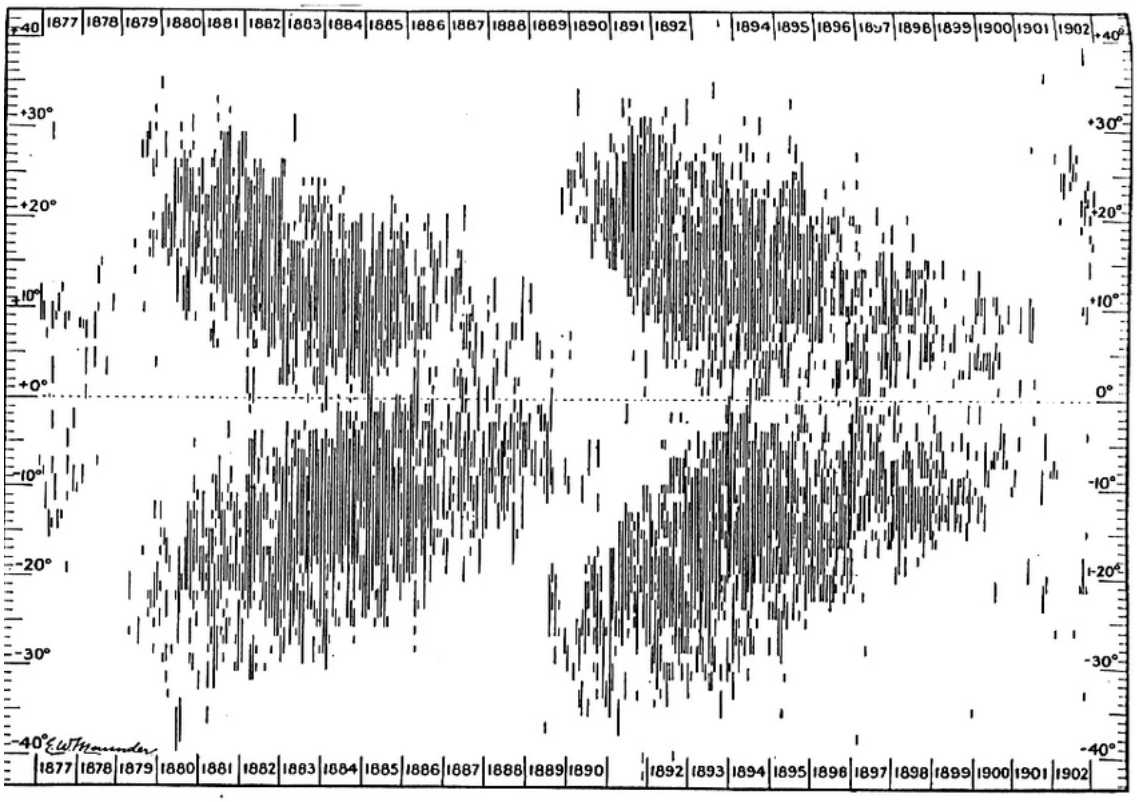

FIG. 8.—DISTRIBUTION OF SPOT-CENTRES IN LATITUDE, ROTATION BY ROTATION, 1877–1902.

Figure 1.1: Figure 20 of Soon & Yaskell (2003), demonstrating the original plots of the Maunder Butterfly diagram published in 1904, with latitude (y axis) versus time (x axis) and coverage indicated by shading.

of the solar cycle and the orientation of the solar magnetic field, and allow sunspots to serve as a basis of comparison for phenomena which occur at higher altitudes in the solar atmosphere.

As the solar dynamo is either northern lead or southern lead depending on the stage of the twenty two year magnetic cycle, there is an imbalance between the northern and southern hemisphere in terms of magnetic activity at any given point. Imbalance in northern and southern solar magnetic activity has been observed for several decades (Bell & Glazer, 1958) and has been explored extensively in a variety

of solar phenomenon such as; sunspot activity (Javaraiah, 2021), interplanetary energetic and geomagnetic indicators (El-Borie et al., 2012), sunspot rotation rates (Xie, Shi & Qu, 2018) among others. The impact that this imbalance has on the rest of the solar atmosphere is not clear, and the degree to which an imbalance might present itself could be greater in other measurable parameters. As part of this thesis, work is undertaken to examine the extent of the north-south asymmetry present within the corona, as part of the investigation into the extent that coronal structures and their positions evolve throughout the course of a solar cycle.

1.3 The Corona

The corona is the outermost layer of the solar atmosphere, lying above the chromosphere and transition region thousands of kilometers above the photosphere, where the magnetic field emerges, from internal dynamo processes in the convection zone, just above the radiative zone. This region of the solar atmosphere is typified by extremely high-temperature, low-density plasma, heated to the the order of 10^6 degrees Kelvin and radiant in extreme ultra violet and X-ray wavelengths due to the emission of highly ionised species of metals (such as iron). In this region of the solar atmosphere the magnetic field dominates the low plasma pressure, possessing a very low plasma beta (defined as the ratio of plasma pressure and magnetic pressure, typically around 0.01 in the corona). As this portion of the atmosphere is highly rarefied, much of it is optically thin.

Coronal structures (sometimes called plumes or loops) are pervasive fundamental structures of the solar corona (Reale, 2014), and form when magnetic flux bundles or tubes propagate from the solar dynamo and out of the photosphere. These flux tubes are connected to a footpoint at the photosphere, and tied to a particular region of plasma by the "frozen in" theorem, by which the magnetic field is held in stasis by a plasma. If these magnetic fields are moved, such as by footpoint

motions, MHD waves within the photosphere, or by the torsion introduced by footpoint rotation, then this magnetic tension builds until it reaches a critical threshold. When this threshold is reached, magnetic diffusion dominates magnetic induction, the Reynolds number (the ratio of magnetic induction to diffusion) approaches zero, and the magnetic fields reform in a new configuration, and magnetic reconnection occurs. This potential energy stored in the form of tension then excites the plasma stuck at the footpoints of these regions, heating up and filling the flux tubes with incandescent plasma, forming visible coronal structures. These filaments can interact with one another during magnetic reconnection, and energy released in one reaction can cause a neighbouring bundle to undergo its own magnetic reconnection. As these cascading reconnections occur within a region of many flux tubes. Because the size of the resulting structure is indicative of the size of the cascade and how many of these flux tubes underwent reconnection at once, the widths of these structures are important for understanding the distribution of the scale lengths for coronal structures and the magnetic interactions which produce them. These structures vary greatly in length, from a few hundred kilometers in very small loops to several solar radii for extended plumes, formed from plasma heated by magnetic reconnection and supported by magnetic flux tubes emerging from the solar interior. The extremely high temperatures and low pressures that typify the corona have been subject to extensive study by solar astrophysicists. There are a variety of models utilizing a wide range of MHD based heating scenarios (such as DC filament (Heyvaerts & Priest, 1984) and AC Wave Heating (Milano, Gómez & Martens, 1997)), though more limited is extensive observational data to compare these models to. This is despite the existence of several long term continuous solar missions, many of which include instruments such as EIS, AIA and Solar Orbiter that observe the corona. Many previous studies have focused on specific aspects of coronal structural

properties in limited and semi-automated studies - such as the cross-sectional profiles and morphology (Klimchuk & DeForest, 2020), lengths (Dahlburg et al., 2018), intensities and temperatures (Xie et al., 2017), and the interaction of complex magnetic regions (Rappazzo, 2015), but these are typically limited and only utilize small portions of the data available to researchers. The evolution of these properties with the changing solar magnetic activity is not fully appreciated, and a chance to study the connection between the corona and the solar cycle is not properly utilized. The question of how these structures are created and sustained at such high temperature and modeling the connection between the magnetic field and the solar atmosphere requires an extensive range of observational data to compare to modelling efforts and to further understanding of long term trends.

Statistically significant quantities of observations could be enhanced by statistical modelling efforts such as Self Organized Criticality (SOC) modelling (Bak, Tang & Wiesenfeld, 1988). These are useful in analysing the behaviour of nonlinear, size invariant systems with high degrees of complexity by approximating the contributions of a wide variety of effects and local conditions as a local requirement of exceeding some critical threshold in some parameter(s), alleviating the requirement for the entire system to be solved analytically for predictions of observational parameters. SOC and its application to the corona is discussed more fully in Chapter 2.

A summary on existing coronal loop observations made with various instruments is provided by Aschwanden & Peter (2017); they outline the decreasing minimum observable loop width that is brought about as a consequence of improving instrumental resolving power. Some of these can be mitigated by choosing loops visible at the coronal limb, but others such as the point spread function and charge spreading effects are nontrivial to deconvolve from images (Poduval et al., 2013) and can effectively destroy information of smaller structures. They describe an observed

loop width as a combination of the true width size and any possible perceived loop broadening which are observational effects. Observed width w is described as the following;

$$w_{obs}^2 = w_{psf}^2 + w_{true}^2 + w_{noise}^2 \tag{1.1}$$

where w = observed loop width, w_{true} = the "true" loop width, or how large the structure would appear if viewed without any limiting effects, w_{psf}= the point spread function caused by the diffraction pattern of the specific instrumental layout. For the AIA, this psf is a combination of the entrance filter, the primary and secondary mirrors, the focal plane filter, and the CCD (Grigis, Su & Weber, 2012). w_{noise} = broadening caused by noise effects such as Poissonian photon noise, dark current, readout noise, etc. For EUV wavelengths in shutterless instruments such as TRACE, this is approximately 2.7 pixels (Gburek, Sylwester & Martens, 2006), but is more difficult to compute directly for more complicated instruments with many pixels such as the AIA (Poduval et al., 2013).

1.4 Instrument - SDO/AIA

The Solar Dynamics Observatory (SDO) is a satellite owned and operated by the National Aeronautics and Space Administration (NASA), and houses a multi-instrumental space-based solar observing mission, covering the periods of the early Solar Cycle 24 (2010 to 2020) and continuing on into Solar Cycle 25 (2020 - Ongoing). SDO was launched in February 2010, as part of the Living With a Star program, and began science operations in June of 2010. The satellite is in continuous circular geosynchronous orbit with an orbital radius of approximately 42,000 km, allowing for uninterrupted, low latency, high throughput connection to the fixed ground terminal at White Sands New Mexico, USA. The purpose of the mission was to continue analysis of the solar atmosphere and magnetic fields, and how the heliosphere

interacts with the Earth's magnetic field within the Sun-Earth system.

Onboard, SDO houses three major instrument assemblies (layout detailed in Fig 1.2) ;

- **The Atmospheric Imaging Assembly (AIA)** which consists of ten filters and telescopes (see Fig 1.3), which captures light in the visible (4500 Å), ultraviolet (1700, 1600 Å), extreme-ultraviolet (335, 304, 211, 193, 171, 131 Å) and soft X-Ray (94 Å) wavelengths. These capture the photosphere, transition region/chromosphere and corona in high spatial and temporal resolution. (Lemen et al., 2012a)

- **The Extreme Ultraviolet Variability Experiment (EVE)** which consists of the Multiple EUV Grating Spectrographs (MEGS)-A, the EUV SpectroPhotometer (ESP), and the MEGS-Photometer. These instruments capture EUV irradiance data which is important for monitoring the heating of the Earth's upper atmosphere (Woods et al., ????).

- **The Helioseismic and Magnetic Imager (HMI)** which observes the solar disc in the 6173 Åwavelength, continuously at high cadence (1 image every 4 seconds). It produces dopplergrams of surface flows, continuum images of the solar surface, and magnetograms of both line of sight and vector based magnetic activity. These allow for detailed analyses of solar magnetic intensities and helioseismological modelling (Scherrer et al., 2012).

Of particular relevance to coronal physics research, AIA represents the most extensive spatially and temportally well resolved coronal image dataset to date, with over 10 years of continuous EUV solar observations in multiple wavelengths and a physical resolution of 0.6 arcseconds per pixel every twelve seconds. Many prior studies have been limited to short periods of time and narrow fields of view, around

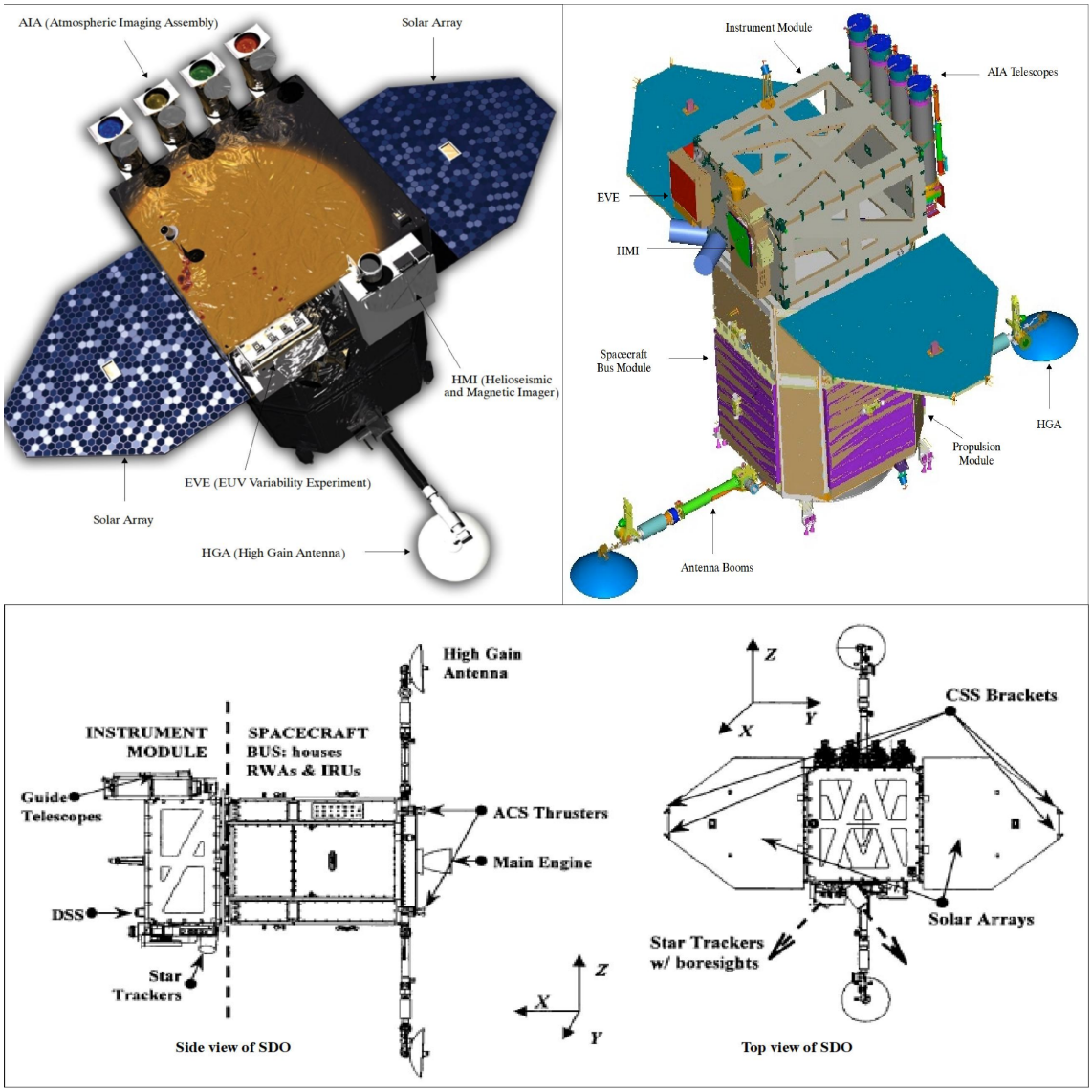

Figure 1.2: Figures 2, 3, and 5 of the SDO Satellite Mission Overview (Kramer, 2012a), outlining the layout of the satellite and its component science instruments from various angles.

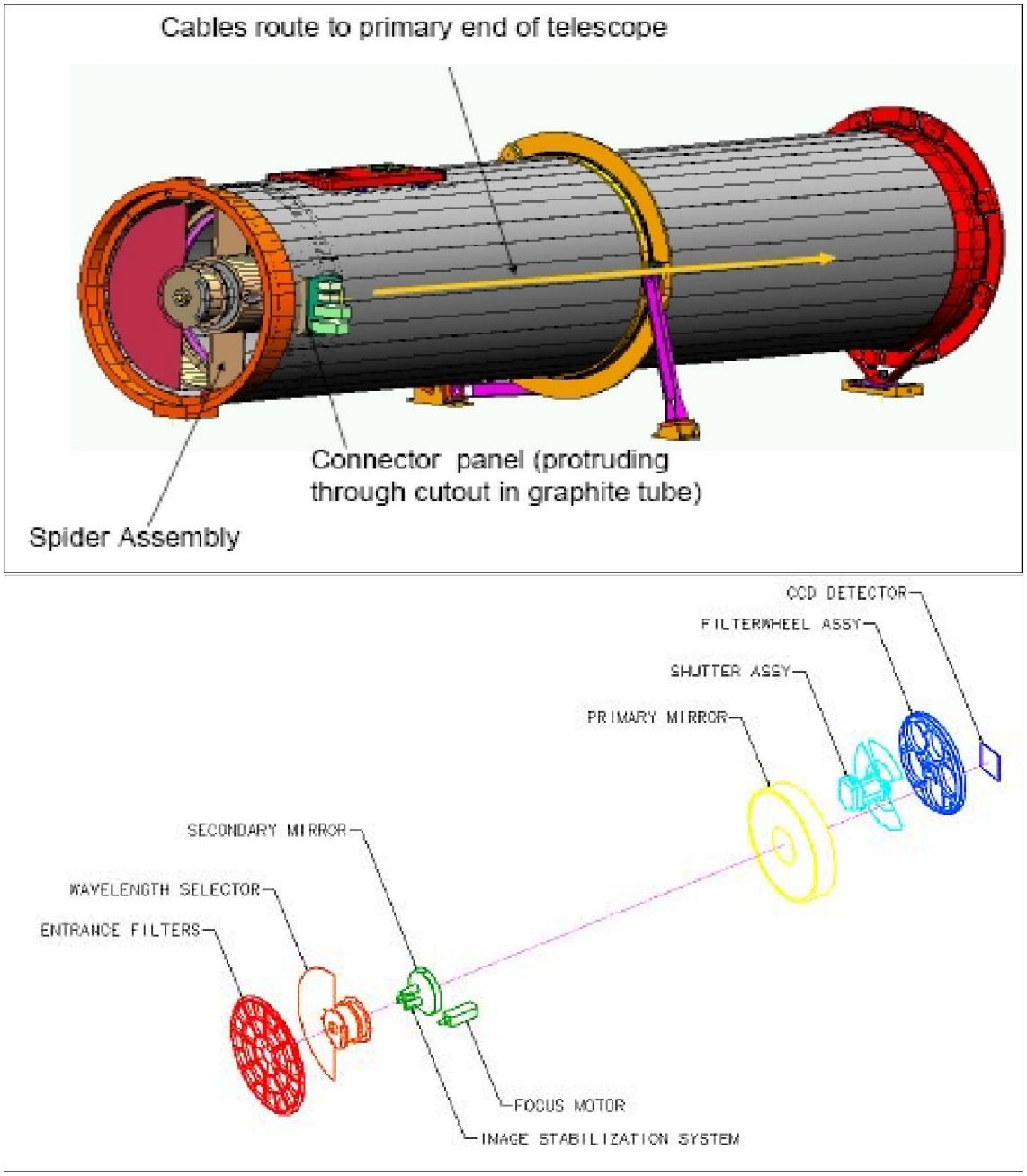

Figure 1.3: Figure 44 and 46 of the SDO Satellite Mission Overview (Kramer, 2012a), outlining an example of one of the AIA telescopes and a simplified diagram detailing of the working components of the detector and filters.

events like coronal mass ejections or single active regions, and do not properly exploit the full range of potential information. Given the quantity of data (roughly 1.5 terrabytes of data produced daily), more advanced data processing and analysis techniques are required to support solar physics research going forwards, and provide a larger body of observational statistics for robust analysis. The utilization and analysis of the EUV passbands of AIA will be crucial in forming a better understanding of structures present within the corona at this time. An example of images from four of the AIA EUV filters is provided in Fig 1.4, demonstrating the varying viewing conditions that will need to be controlled for to constrain coronal structures above the limb.

The temperature response of filters in AIA is defined in detail in Lemen et al. (2012b) , and is a measure of how narrowly a filter can detect plasma of a specific temperature which is distinct to certain species of emitting ion. Typically this is predominantly emission from one ion in the EUV channels, but contamination can occur from lower lying H and He transition emission, or from iron emission in a very similar wavelength (as is the case with the 193 Åfilter, which is sensitive to both Fe XII and Fe XXIV to a lesser extent, with characteristic log T of 6.2 and 7.3 respectively.) By choosing filters with sensitivity to single temperatures and ions, specific layers of the corona can be isolated and measured without interference from others in line of sight. Of additional consideration is the fact that AIA has experienced standard degradation of its detecting CCDs due to continuous exposure to solar radiation and energetic particles, which has affected some channels more severely than others (such as the 304 Åchannel), which will cause the response function to become worse over time. This degradation can be accounted for to an extent by localized normalization and detection, but the range of possible intensity values has probably decreased. This has likely not decreased the probability of successfully observing structures, but may affect the detected widths of structures

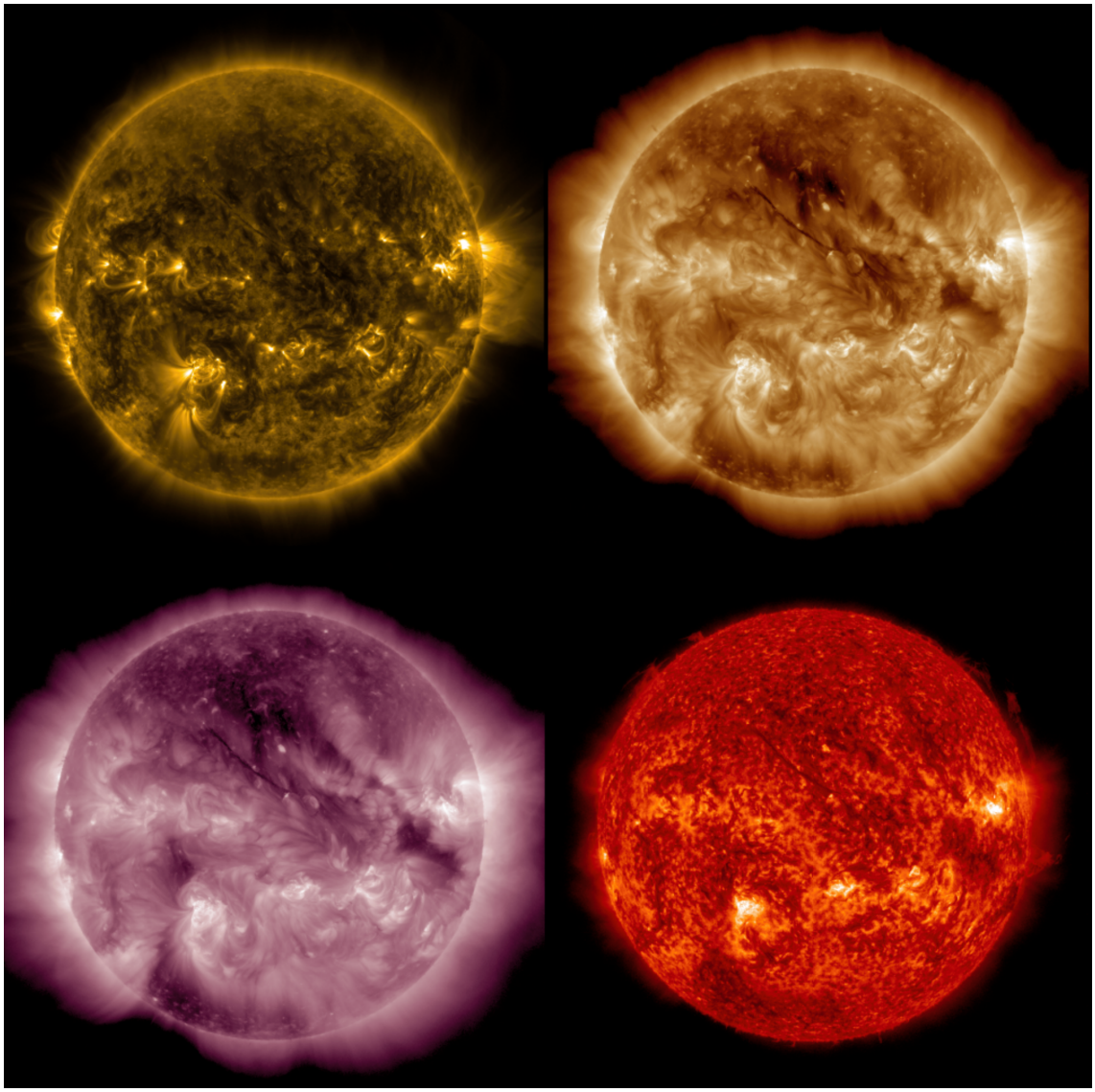

Figure 1.4: Images of four full resolution EUV AIA images in 171 Å(top left), 193 Å(top right), 211 Å(bottom left) and 304 Å(bottom right), demonstrating the differing visual properties and altitudes of the varying coronal structures above the limbin these varying wavelengths.

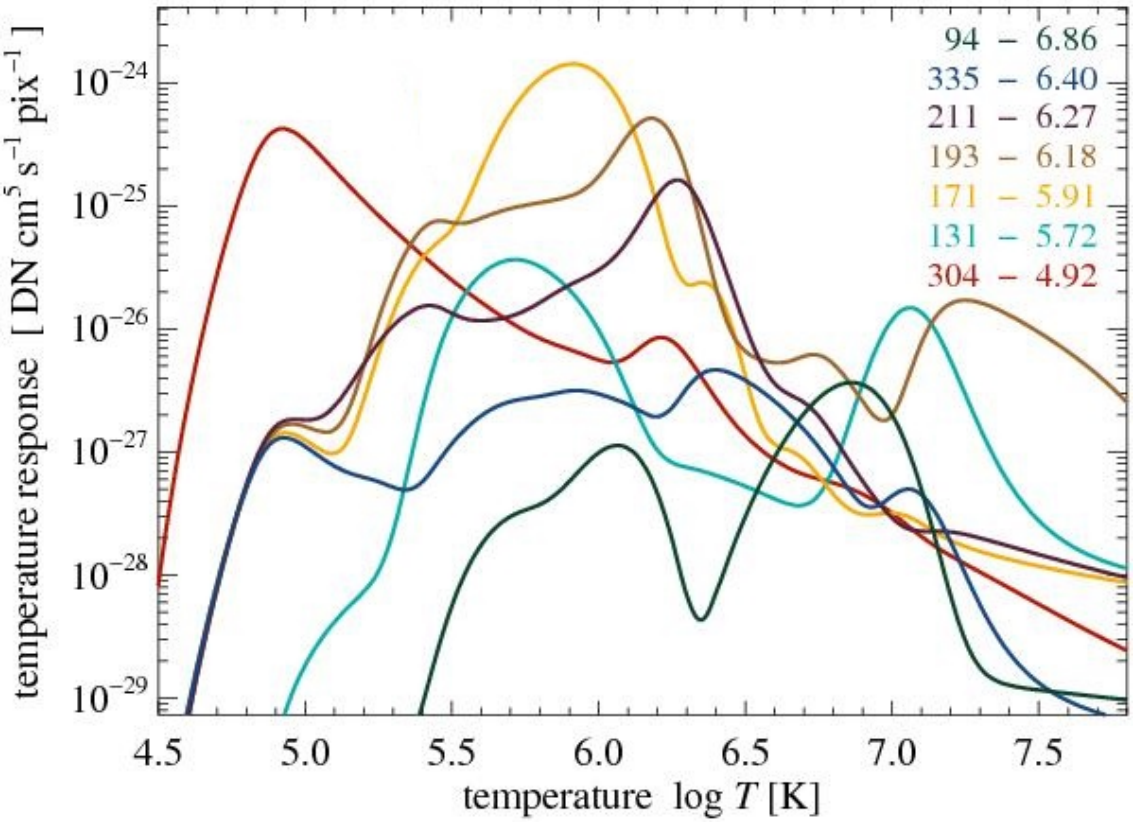

Figure 1.5: Figure 1 of Peter, Bingert & Kamio (2012), utilizing data from Boerner et al. (2012), indicating the Temperature Response Functions of the AIA filters by wavelength. Note the presence of broad (335) or multi-peaked (131, 94) wavelength filters.

with narrow widths and high intensities. (Dos Santos et al., 2021)

A temperature response profile is seen in Figure 1.5

The wavelength response of AIA filters is defined in Boerner et al. (2012), and is an indicator of the efficiency of a particular filter and attached detecting instrument at filtering light from unrelated wavelengths. This contamination can occur due to degradation of the CCD and other instrumental equipment over time, "crosstalk" of light from filters attached to the same detector housing structure, the quantum efficiency and gain of the CCD, as well as a number of other factors. The spectral

resolution of a filter determines how much unwanted light is present in the final image, and can effect the resolution of structures imaged in that band. The normalized wavelength response function for coronal AIA bands as of Jan 1st 2015 is shown in Figure 3.

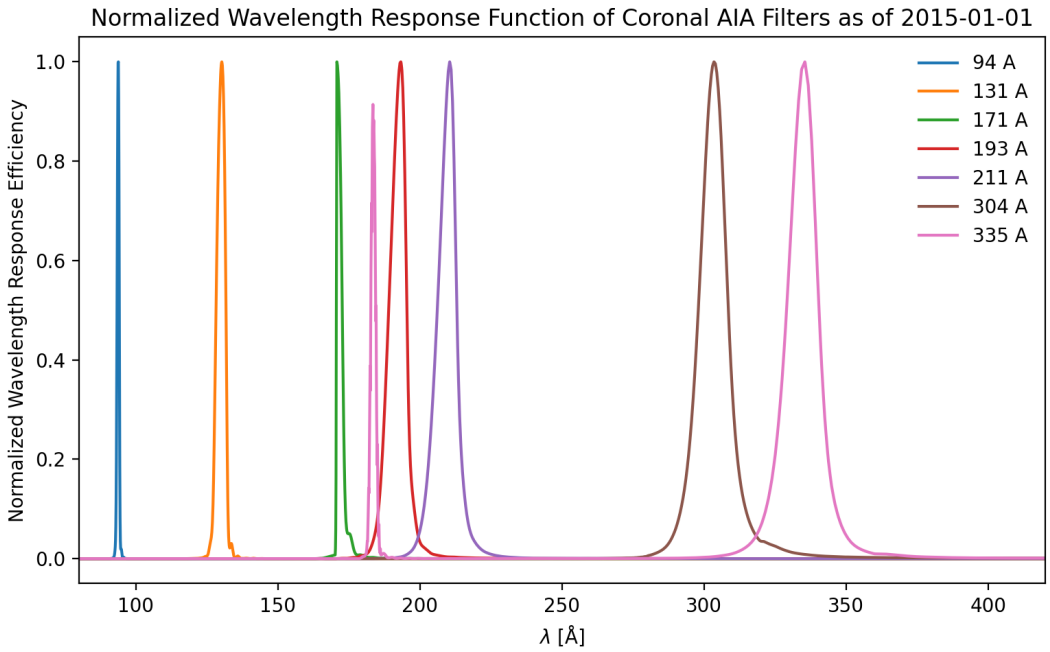

Figure 1.6: Normalized wavelength response efficiency (y axis) versus wavelength (x axis) of AIA EUV Filters.

The **171 Å** wavelength band of the SDO AIA is sensitive to emission from Fe IX at roughly 600,000 K, corresponding to the quiet corona and upper transition region. This is one of the most spectrally well resolved filters of the instrument, and is the most favourable for detection of coronal loops. Consequently the width frequency distributions are the most populated, and confidence in assessments of the power law slopes are higher than those of other wavelengths. 171 Åis used as a base of comparison for other wavelengths.

The **193 Å** wavelength filter is sensitive primarily to Fe XII , though a small

amount of Fe XXIV emission (1-5 percent sensitivity of Fe XII) is also detected. Fe XII has a characteristic temperature of 1,000,000 K, and is representative of the hotter upper corona.

The **211 Å** filter is sensitive to characteristic Fe XIV emission at roughly 2,000,000 degrees K and represents the high energy corona. This filter is singly peaked in both the wavelength response efficiency and temperature response, making it a good candidate for measurement of hot coronal structures.

304 Å is primarily a chromospheric filter, with a characteristic emission of He II at 50,000K. It therefore represents plasma a much lower temperature than other lines, and the only line which is not an ion of iron. 304 Åis additionally of interest to coronal studies in that is is the only filter along with 171 Åwith coverage in all three instruments covering Solar Cycle 23 with SOHO EIT, Solar Cycle 24 with SDO AIA, and the upcoming Solar Cycle 25 with Solar Orbiter. As this line represents much cooler plasma, the structures observed by this channel are likely to vary from those seen in other EUV channels. This means that images could possibly contain optically thick material, which could alter the observed geometries of structures depending on its placement.

In light of these factors, the filters of particular interest to this study in order of increasing wavelength are; 171 Å, 193 Å, 211 Å, and 304 Å. These filters were chosen due to their temperature and wavelength response functions - they possess relatively narrow wavelength response functions (spectral resolution), and singly peaking temperature response functions (predominantly single ion emission). This data is reduced to level 1.5, where the image is corrected for pointing and degradation of the CCD over time. Level 1.6 data, which is data which has had a precalculated PSF deconvolved from the image after pointing corrections was not used in this project for a number of reasons. Firstly, the process of producing level 1.6 data is computationally expensive, requiring ten to fifteen minutes per image using CPU

based processing or specialized GPU processing which was not available at the time of the project. This would have added up to additional 2000 computing hours to the time required to process the full data set. Secondly, the techniques as described in subsequent sections require positional information which is still possible to obtain with the level 1.5 image data. As coronal structural intensity data would need to be extracted from an image which was not altered by a deconvolution process, it was not necessary to use level 1.6 data to achieve the science objectives of this project.

As of yet, no large scale study of coronal structures from across a solar cycle has been made. Though expected to be strongly related to sunspots by their shared emerging magnetic flux tubes, it is difficult to definitively determine the relationship between simple emerging flux tubes present at the footpoints of coronal loops and more complex structures higher in the solar atmosphere without direct observation. The aim of this work then is to identify and record the largest possible population of coronal structures across Solar Cycle 24 by measuring the evolution of coronal loop width and colatitude by wavelength. This will allow for novel analysis of the corona - measuring specific changes to these parameters across temperature regimes and time and contrasting them to other well known indicators of solar activity such as sunspots, models of predictions of coronal loop parameter distributions.

In this thesis, work will be broken down as follows. Chapter 2 will cover an outline of the theory used to examine the distribution of coronal structures in terms of their widths, demonstrating the theory of Self Organized Criticality. Chapter 3 describes the methodology involved in the detection and analysis of coronal structures above limb for both the active region and polar regions, and statistical analysis of the resulting distributions of their width and colatitude parameters. Chapter 4 will describe the development and design processes behind the algorithm used to perform the image analysis of coronal structures within Solar Cycle 24, and detail some of the aspects of software development of the COSDA algorithm. Chapters 5 and 6 detail

the science results of the investigations into equatorial active region and polar region coronal structures above the limb, compiling the widths into power law profiles and analysing the north-south asymmetries. Chapter 7 details an investigation of Solar Cycle 23 using SOHO EIT data, and the variations in method necessitated by the change in the technical profile of the instrument. Chapter 8 provides an overview, discussion and conclusion of the work carried out.

Chapter 2

Theory of Self Organized Criticality

2.1 Introduction to Self-Organised Criticality.

Self-Organized Criticality is a property of some dynamical systems possessing a global critical instability, non equilibrium, many degrees of freedom, and local critical thresholds that are driven by stochastic energy addition, causing dynamic, nonlinear cascades. This property displays itself in predicted distributions of the scale lengths, energy dissipation, and the size of these events which occur. As outlined in Bak, Tang & Wiesenfeld (1987) and detailed more thoroughly in Bak, Tang & Wiesenfeld (1988), this was originally devised as an explanation for flicker or 1/f noise observed in a wide range of settings such as recorded audio or images. It is described as emerging from "dynamical systems with spatial degrees of freedom, naturally evolving into a self organized critical point". It is more specifically defined by Aschwanden, M. (2014) as "a critical state of a nonlinear energy dissipation system that is slowly and continuously driven toward a critical value of a system-wide instability threshold, producing scale-free, fractal-diffusive, and intermittent

avalanches with power law–like size distributions."

This model explains how cascading processes such as landslides and avalanches can develop from small scale interactions of fundamental components ie; grains of sand and grow to cascade throughout much larger scale lengths than the initial event. When a local critical condition such as force on an individual grain of sand is met, this causes a local change which can affect other nearby points ie; the grain of sand falls and increases the force on other nearby grains. This can trigger a cascading reaction, from which larger observable behaviour can be observed. Systems with the potential to experience cascades throughout the size of the system are said to be in a state of least stability, as any perturbation to the system anywhere can trigger system wide cascading behaviour, wholly describable as the composite result of these small cascading events. The strength of this model is that it requires no underlying physical understanding of the process being approximated, as the exact underlying mechanisms for criticality can be approximated.

It has been investigated thoroughly for its applicability in the field of astrophysics in general (Watkins et al., 2016) and solar physics in particular (Sharma et al., 2016; McAteer et al., 2016) for its relevance in describing a range of nonlinear scaled relations, and an example of this method applied to X-Ray flaring regions is shown in Fig 2.1, where SOC model lattice grids of varying sizes (right) are shown to approximate flaring behaviour sampled at varying pixel sizes (left) to differing degrees of spatial accuracy.

The formal relationship between frequency and scale adopted by the SOC model is described as;

$$D(s) = As^{-\alpha} \tag{2.1}$$

Where D(s) describes the distribution of the frequency of events as a function of their size (s) (in terms of number of individual local critical events which comprise it),

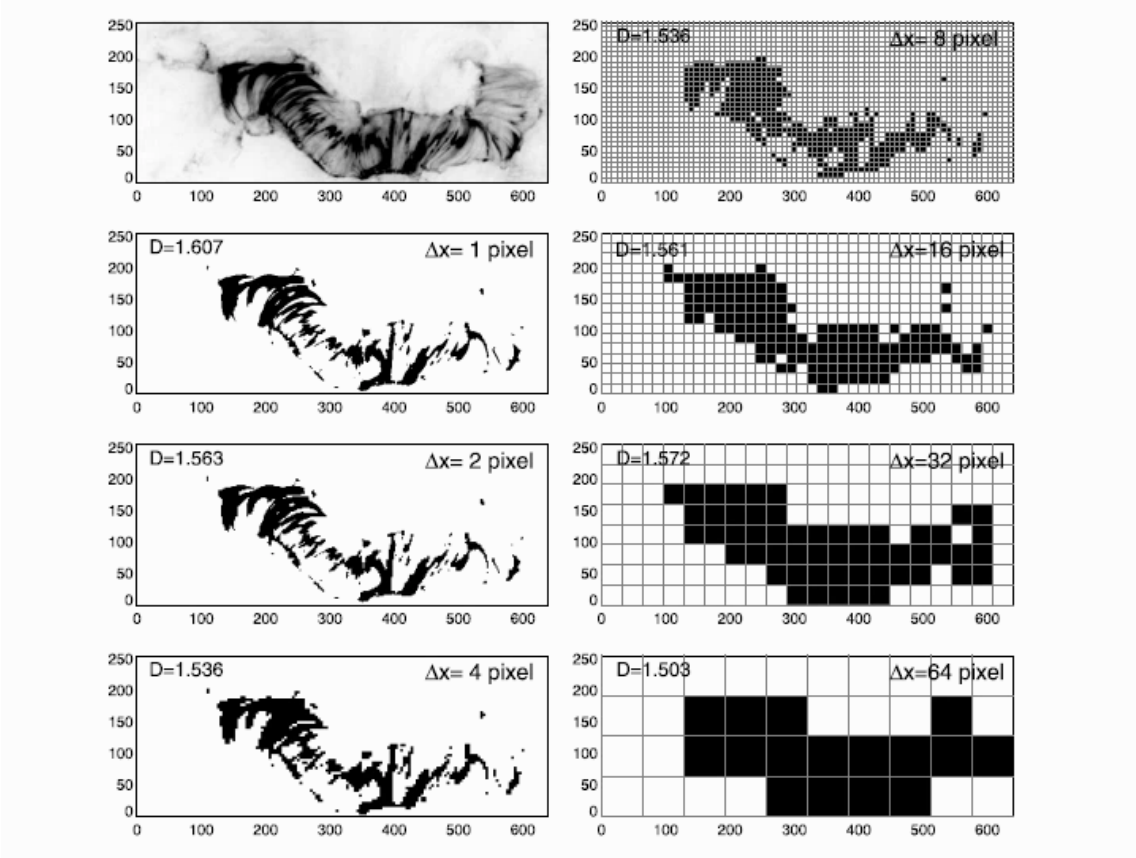

Figure 2.1: Figure 4 of Aschwanden & Aschwanden (2008) demonstrating different approximations for activity within a coronal active regions with different fractal dimensions and SOC lattice grid sizes. Real image of TRACE 171 A active region(top left) downscaled to various pixel resolutions (left), and SOC lattice grids of varying sizes (right).

where A is some constant specific to a particular distribution and -α is the exponent, measurable as the slope of a power law fit to the distribution. These processes are described as scale invariant and fractal, as they occur over many orders of magnitude in scale length.

The distribution of other descriptions such as D(A) Area, D(T) Time Duration, D(P) Peak Flux similarly describe the frequency/probability distributions of the parameters of events that occur within a given space. They are statistical descriptions of the general behaviour of parameters within that space and are described by the Standard FD-SOC (Fractal Diffusive SOC) model and their relationship to D(s). These have predicted values based upon parameters such as diffusivity and spatial/fractal dimension. In the case of D(s), this predicted value is 1.5, as will be demonstrated in a derivation outlined in Watkins et al. (2016) and recreated as follows,

If, in a continuous grid of SOC space, the amount of energy dissipated in one continuous avalanching event (E) is proportional to the number of cascading cells which experience a local criticality (S), and that the total number of events which can occur is proportional to the total effective space ($L^{D_d+2/\beta}$ (Where L is the one dimensional length, D_d is the fractal dimension, and β is the diffusion constant), then the relationship between energy, events, and space can be simply described as

$$E \propto S \propto A \propto L^{D_d+2/\beta} \tag{2.2}$$

Where E is energy, S is scale length, A is area, and D_d is the fractal dimension of the system (Aschwanden, 2012), and can be defined as

$$D_d = \frac{(1+d)}{2} \tag{2.3}$$

Where d is the spatial dimension of the system.

By substituting this expression into an expression for the the scale free probability conjecture (Aschwanden & Freeland, 2012), which is the length scale distribution of events within this SOC space ie; the "density" of the number of events of a particular scale length occurring, the fundamental length scale equation is described as,

$$N(L)dL \propto L^{-d}dL \tag{2.4}$$

for L $\leq L_{max}$

Where $N(L)$ is the distribution of the size of scale lengths for avalanches within the space, L is the size of a singular avalanche, d is the euclidean dimension of the system, and L_{max} is the size of the space (ie; the maximum possible avalanche length). Given that the relationship between energy dissipated E is proportional to the avalanche size S, the following scaling law can be created (McAteer et al., 2016).

$$E \propto S \propto L^{D_d+2/\beta} \tag{2.5}$$

By substituting this scaling law into the fundamental length scale equation 2.4, the distribution of energies from cascading events within a system can be described as

$$N(E)dE = N(L[E])|\frac{dL}{dE}|dE \propto E^{-1+(d-1)/(D_d+2/\beta)}dE \tag{2.6}$$

We can present this expression with the following substitution,

$$N(E)dE \propto E^{-\alpha_E}dE \tag{2.7}$$

In this form, the exponent α_E can be expressed as

$$\alpha_E = \alpha_S = 1 + (d-1)/(D_d + 2/\beta) \tag{2.8}$$

If it is assumed that the spatial dimension d is equal to 3 and a diffusion constant β of 1 (classical diffusion), the expression evaluates as

$$\alpha_E = \alpha_S = 1 + (3-1)/(2+2/1) = 1.5 \tag{2.9}$$

Thus, a predicted value of α_E, and therefore α_S, the slope of the distribution of dissipated energies and the number of events which occurs within avalanches is 1.5, assuming three dimensional space and classical diffusion for the standard Fractal Diffusion SOC model.

2.2 SOC and the solar corona

As described previously, SOC or Self Organized Criticality refers to the phenomenon of often complex macroscopic behaviour emerging from small scale interactions between individual elements, Such behaviour is said to be self-organizing due to a lack of a larger influencing relation, with criticality referring to the critical threshold required to trigger a local change. Such phenomenon are localised energy dissipation processes. In coronal physics, the formation of coronal flux tubes can be considered to be the result of perturbation of magnetic field carrying plasma in structure footpoints. These perturbations cause localised heating events, which can cascade to nearby plasma resulting in the formation of a visible coronal loop as heated plasma expands to fill the flux tube (Török & Kliem, 2003; Inoue et al., 2018a).

SOC then can be taken as a type of statistical probe of emergent behaviours in the corona. As it takes no assumptions or is informed by any physics within the region of loop formation, it cannot directly provide information as to physical conditions or which specific mechanism or threshold condition is required to produce the observed collection of loops. However, observation of these structure populations applicability of can provide evidence as to the degree with which these non-linear dissipative processes are applicable to the observed phenomenon of coronal structures.

The power law predicted by the ideal FD SOC is indicative of the presence of coupled, driven oscillators and the dissipative non-linear avalanching behaviour, which spreads across all available scale lengths given a stochastic driver. As it can be safely assumed that the simple SOC approach is not wholly descriptive of the physical phenomenon occurring in the environment of the solar corona during loop formation, deviations from this ideal value can be described as combinations of observational effects, and specific variations as described above. These variations can also be described by modification of the simple ideal case.

In the context of this work, if coronal structures do follow SOC like distributions, then a collection of their physical widths should be describable by a power law. By measuring a wide variety of coronal loops in varying conditions, a profile can be developed and a power law fit and measured.

Prior results in studies of active regions such as NOAA 11158 and demonstrate SOC distributions within coronal loop populations found that power law slopes of widths from these coronal loops range from roughly 2.7 - 3.3 for active regions viewed in multiple AIA filters and around 1.39 in Hi-C populations. (Zhiming et al., 2019; Aschwanden & Peter, 2017) This compares to an "ideal" FD-SOC slope of 1.5

Gradients for varying wavelengths at various points in the solar cycle can be compared and measured, and the exact difference between α_{w} in various stages of the solar cycle and with α_{s}, the power law exponents of observed width and theoretical event distributions respectively, can be quantified and analysed. The closeness of fit of these observed profiles to the previously mentioned power-law will be used to analyse loop widths, comparing different populations of loop widths from various points across the entire recent solar cycle in the first instance. In subsequent chapters, these power laws form a basis for analysis of coronal structure populations across varying time periods and wavelengths.

CHAPTER 2

Coronal structural widths follow their own distribution, which has been demonstrated but not examined in terms of similarity to SOC models. (Aschwanden & Peter, 2017), using Self Organised Criticality as an approximation for coronal loop behaviour, describes the distribution of loop widths as a nonlinear dissipative process is demonstrated by a power law distribution constrained by a lower observational limit described by Eq. 2.1 They approximated coronal width frequency $N(w)$ distribution measurements to the FD-SOC N(E) or energy dissipation distribution. Their results indicated that loop widths could be modelled by an SOC approach, but variances between the ideal slope value of 1.5 and the observed slope values of roughly 3 in multiple AIA bands indicated some divergence from the absolute FD SOC prediction.

The reasoning for these widths being analogous to D(s) is because of the physics of their formation. If each coronal structure is comprised of thin subresolved filaments of magnetic flux tubes, which has been supported by a large body of observational and theoretical works (Williams et al., 2021; Peter et al., 2013; Xie et al., 2017; Reale et al., 2016), then these assumptions of interacting strands or filaments might comprise a potential SOC space within the coronal footpoint. As each filament undergoes some degree of magnetic reconnection, plasma at the footpoint of the flux tube is heated, and fills the filament which can then be seen by observation. The size of the observed width then is directly proportional to the number of these filament strands which undergo criticality in a single event, as each one contributes to the total observed width of the structure.

If the distribution of widths was truly scale invariant, the distribution of events would follow an exponentially decreasing frequency from the smallest to the largest available scale lengths. The actual distribution of coronal loop width cross sections D(w) seen in observable populations is a thresholded power law, as demonstrated in Fig 2.2. Though the power law seen in this work is higher than the expected 1.5,

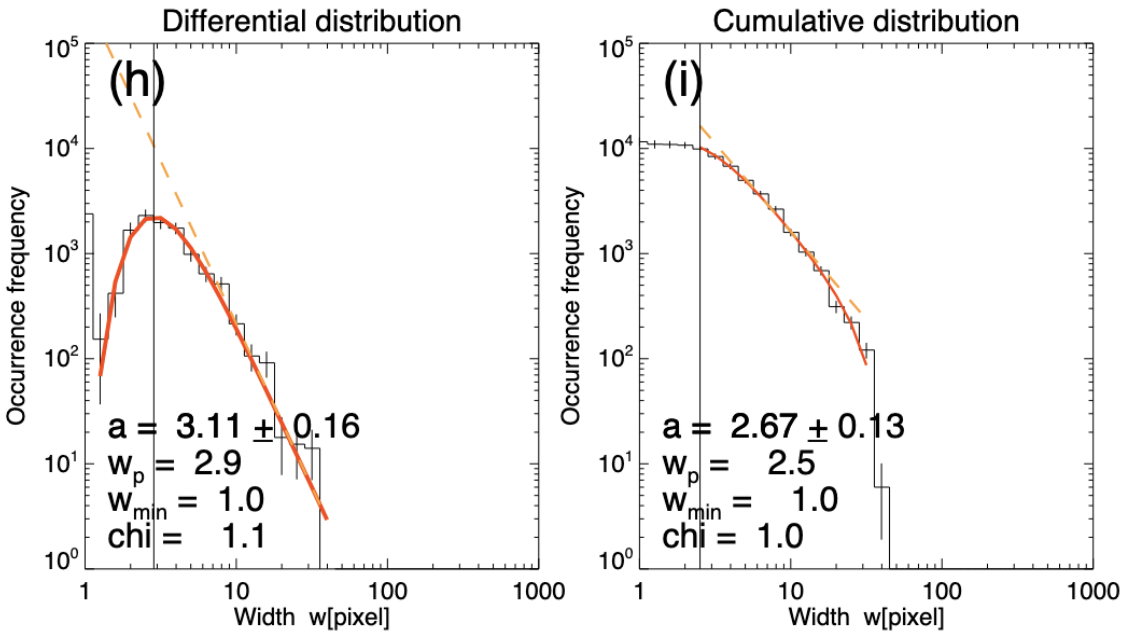

Figure 2.2: Figure 10 h and i of Aschwanden & Peter (2017), demonstrating the thresholded power law distribution of loop widths. These loop populations were collected from an active region imaged in 193 A using the AIA.

at around 3.11, this is a limited selection of coronal structures from a single active region observed in one wavelength, and does demonstrate that coronal widths can be described as a power law distribution.

2.3 Thresholding Effects and their Applicability to the Corona

2.3.1 Scaling Effects

Finite size scaling effects are caused when the scale length of an SOC system is constrained. The scale invariance of the SOC system which causes the continuous size distribution is truncated when the scale length of the system is limited. This can

affect both the frequency of small events and larger events, as the system lacks the space for numerous small cascades and simultaneously limits the space over which larger events can occur. As most physical systems are not infinite in size, some level of thresholding towards larger scale lengths is to be expected, in terms of the assumptions which inform SOC model predictions, scaling limits would negatively impact the maximum scale length of the space (L_{max}, in terms of Eq. 2.4), and would therefore negatively affect the distribution of $N(E)$. This would result in a lower maximum scale length (less large scale events), as well as less events overall. Similarly, if there was a minimum scale length which was not many orders of magnitude smaller than the largest scale length, the distribution would similarly appear to be truncated at the lower ends.

This could apply to the corona in a few ways. Primarily, a smaller SOC space is analogous to smaller footpoint regions, or regions in which "global" criticality can be sustained. If some sections of active regions have more areas with sufficient magnetic potential or free energy, then it is more likely that a larger number of filaments are available for cascades to spread across. This would result in more wider structures than would be seen in regions where less filaments were close to or approaching a critical state. Inversely, if there are periods where less footpoint regions are in a critical state, then the total available space for producing larger events will be similarly curtailed.

2.3.2 Quenching

Quenching, as outlined by (Bak, Tang & Wiesenfeld, 1987, 1988) is the process by which energy cannot be equally distributed within an SOC space, as might occur when energy is preferentially distributed along a certain axis when local criticality is exceeded and the excess energy dissipated into neighbouring cells. This can be caused as a result of non-universal critical thresholds, or by a greater amount of

energy escaping the system rather than by being transmitted to other cells. This is primarily a feature of physical rather than purely statistical systems, as the degree of energy inefficiency and the ability for energy to transfer within the SOC system rather than be transported away by the dissipation process is largely dependent on which physical system is being described. In this manner, the diffusion constant β might be affected, resulting in a system which is not properly described by classical diffusion. The effective fractal dimension of a system can also be affected by quenching, as energies may not be as easy to spread in one direction as compared to another, reducing the effective scale lengths in different spatial dimensions. The effect these can have on resulting power law slopes of events within this system are shown in Fig 2.3

The discussion and examples presented so far assume variations to variables within an established SOC model, which is presented to be analogous to DC heating. These are very unlikely to be the only physical effects which determine the effective addition and dissipation of energy within the corona, even accounting for effects which are known to occur, such as by wave heating or a host of other potential physical effects.

Given that SOC is primarily a statistical model which is uninformed by the physics of a particular phenomenon, it is likely that physical systems can deviate from these simplified assumptions, and the contribution of non-SOC processes to an underlying SOC process is likely to alter the observed distribution of events $N(E)$ or $N(S)$. An example by which a physical process could alter a resulting distribution is by change to the assumption of stochastic addition. SOC relies upon the random addition of energy to individual elements within the SOC space, but this may not necessarily be the case for all physical systems. Under linear addition (see bottom rows of Fig 2.4 and 2.5), the energy is added to a single position within the SOC space, and cascades occur as a result of energy dissipating from this point. This

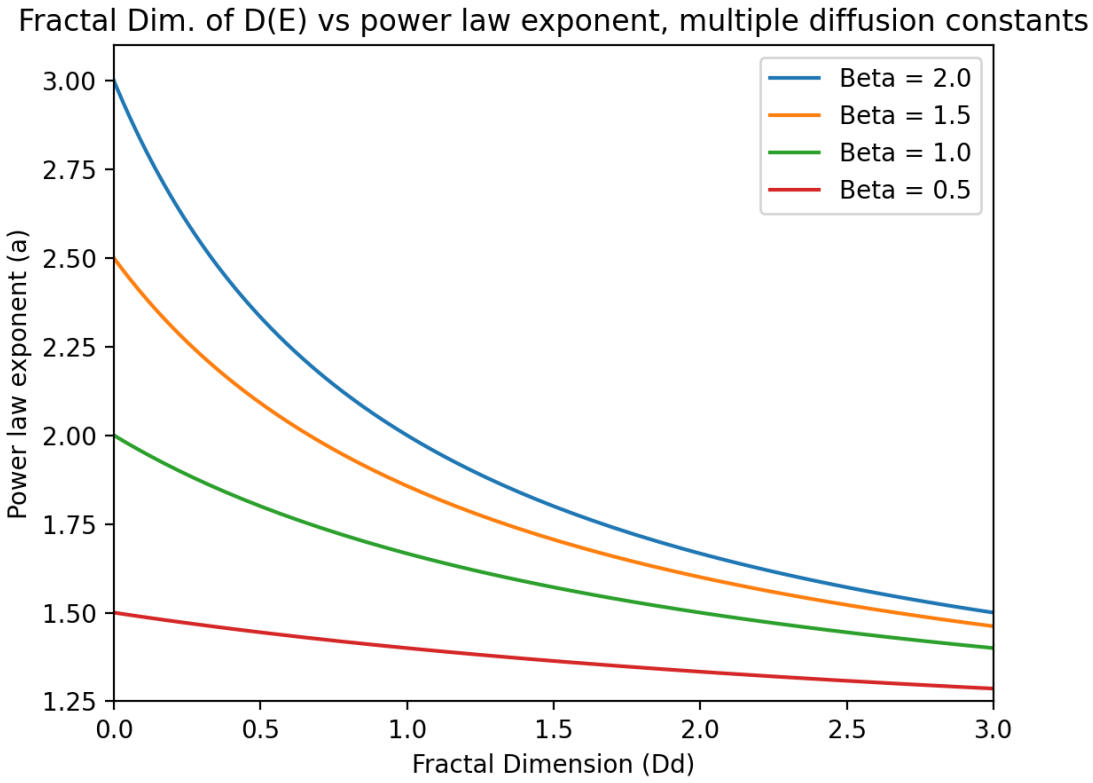

Figure 2.3: A diagram demonstrating the effect of (diffusion constant) (colours), and Fractal Dimension D_d (x-axis) on the power law exponent α (y axis), according to Eq 2.8. High diffusion constants and low fractal dimensions result in high slopes, whilst low diffusion constants and high fractal dimensions result in low power law slopes.

has implications for the shape of the resulting $N(E)$ distributions and the resulting distribution, as seen in results in simulated sand pile models in Fig 2.4 and Fig 2.5. Note the change from an exponential distribution of $N(E)$ under stochastic addition versus a linear distribution under linear addition. It is likely that the energy contribution mechanisms present within the corona is not entirely stochastic nor linear, and so a more complicated distribution of N(E) than ideal SOC models may result.

Lastly, the assumptions of a large number of events with which to populate the profiles. This is exclusively a concern for the observational results of physical systems, as it is primarily caused by an undersampling of events which occur within an SOC space, or by a less than sufficient number of events to properly populate the N(E) profile. If these distributions are under sampled, it can lead to incomplete estimations of the function space. This is most likely to affect phenomena which are difficult to examine, as many events will not be captured. This could affect events at the higher end of the N(E) scale, as not enough events may occur to properly populate these regions. This can also be seen in Figures 2.4 and 2.5, which are distributions of a simulated 1-D sandpile toy model as outlined by Bak, Tang & Wiesenfeld (1987) developed as part of this thesis and performed as an exploratory probe of distributions and sand pile shapes with varying addition mechanisms (random top, linear bottom) and completion states (left allowed to reach global least critical state, right for less than global least critical state).

The measurement of the statistical distribution of observed loop widths should inform us as to whether the simple FD SOC approach is sufficient to approximate adequately the conditions underlying within loop forming regions, or if there is a degree of variation which must be accounted for by either observational effects or by fundamental physics which cannot be approximated. Physically, it indicates a fractal dimension density (see Eq. 2.7) of the distribution, and if this is greater

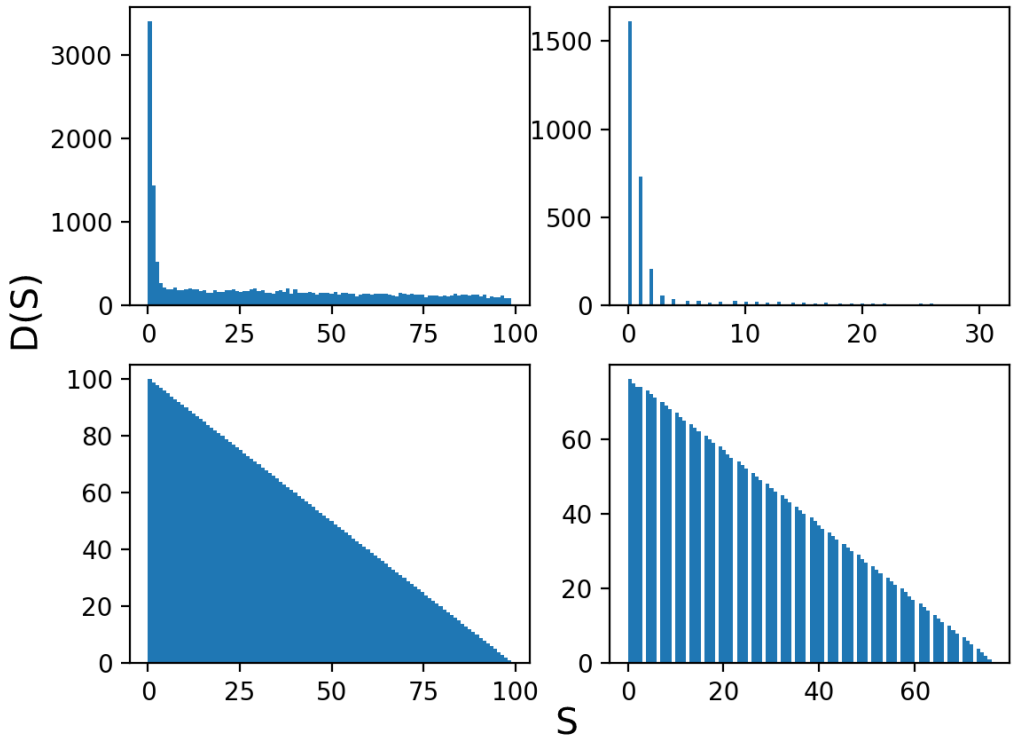

Figure 2.4: A figure demonstrating the profile of $D(S)$ (frequency along y, for a simple, simulated sandpile as per (Bak, Tang & Wiesenfeld, 1988), evolved to fulfill global least stability right, and not allowed to evolve to fulfill global stability left, for both stochastic addition (top) and linear addition (bottom).

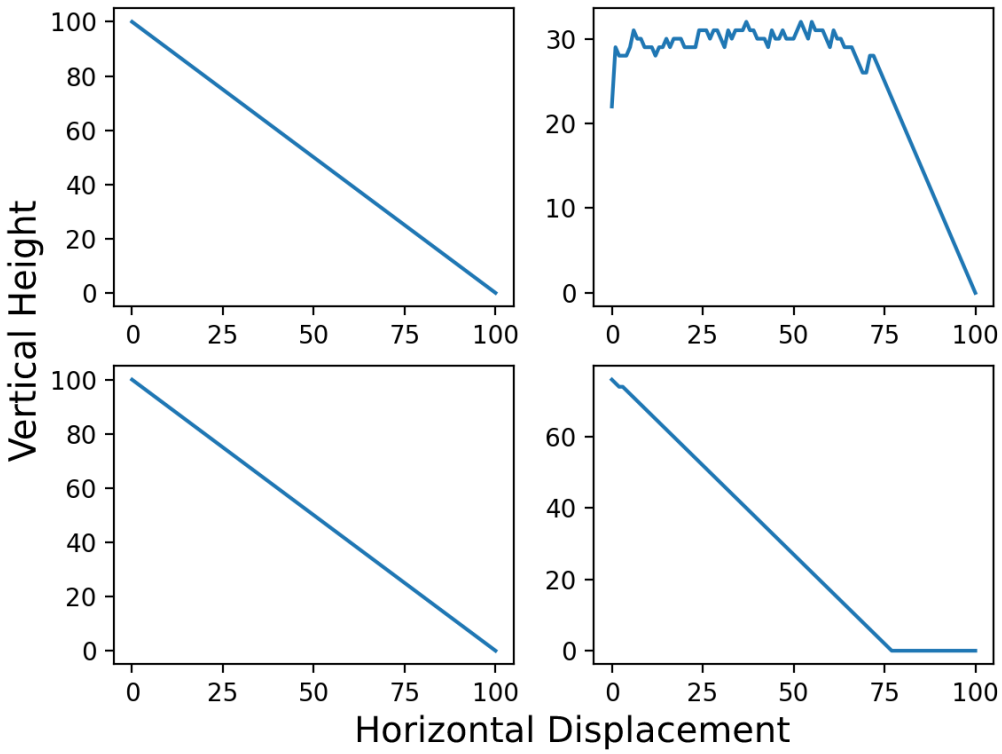

Figure 2.5: Diagram demonstrating the physical profile of the 1-D sandpile model with stochastic addition (top) and linear addition (bottom). Complete profiles (left) are identical, whilst incomplete profiles (right) show differences characteristic to the energy addition method.

or lower than the predicted value, this may inform us as to the changing physical conditions within the corona.

In conclusion, SOC can enable a wide variety of useful scientific analyses for observed coronal structural width data, despite a lack of knowledge for the exact physics occurring in these structure forming regions. By evaluating the change of the observed coronal widths in comparison to the ideal FD SOC power law slope of -1.5, and how these results may vary in time, insights into physical processes may be obtained, as well as understanding of how the variances and deviations from ideal SOC assumptions described above may be descriptive of real physics within the Corona. The following section will better detail the methodology used to obtain these results for study.

Chapter 3

Method and Error Propagation

To analyse structures of interest within the corona, they must first be identified and traced. Identifying coronal loop structures can be challenging. Difficulties of variable geometries owing to the relative angle of the observed structure to instrument mean that geometry and width determination must be considered. This is not always feasible to perform in all visible portions of the corona in an automatic fashion, as there are a number of assumptions which must be made about the underlying loop orientation and background, which involve very complex magnetic and structural topologies (Beveridge, Priest & Brown, 2004), which can introduce errors to subsequent measurement. (Mikić et al., 2013)

Additionally, the contribution of background/foreground emission along the integrated line of sight can be significantly greater than the emission of coronal loop structures, and attempts to properly isolate loop intensity from background measurements can be challenging. (Reale, 2014)

To mitigate these issues, coronal loops at the limb were chosen as the basis of study for further measurement and analysis. Limb loops are by definition observed away from the bright solar disc, thus simplifying issues relating to contaminating background and foreground emission, hence allowing for measurements of loop width and intensity to be undertaken with minimal background subtraction. In densely

clustered areas (around active regions for instance), it is possible that loops overlap visually, as optically thin coronal plasma would not block emission from loops further away from the instrument in the same line of sight. This is also possible in limb measurements, but the relative orientation means that it is less likely for loop structures to completely occlude one another as would be the case in nested loops. Note that measurement of width of these clusters of loops and intensity may be difficult to differentiate from wider, brighter singular loops. Additionally, it can also be difficult to differentiate closed coronal structures (coronal loops) from open coronal structures (streamers), especially at latitudes away from the solar equator. Steps such as restricting identification and analysis to certain latitudes will help to minimise these issues as much as possible.

3.1 Defining time periods across the solar cycle

Solar magnetic activity of cycle 24 occurs from 2010 to 2020. To examine the overall cycle was broken down into three main time periods.

- The **"Rise"** phase is defined as the time of rising solar activity, starting from a base level of minimal activity and extending to the time when the first peak of solar sunspot activity for cycle 24 is recorded. The Rise period is relatively short, beginning 13/05/2010 (the earliest captured data within the AIA database) and extending to the end of 15/11/2011.

- The **"Peak"** phase is defined to be the period of maximum solar activity from 15/11/2011, where sunspot count is slowly but consistently increasing, until 15/11/2014, after which activity begins to decline consistently. This period contains the solar maximum for cycle 24, and corresponds to he highest quanity of observed sunspots within the cycle.

CHAPTER 3

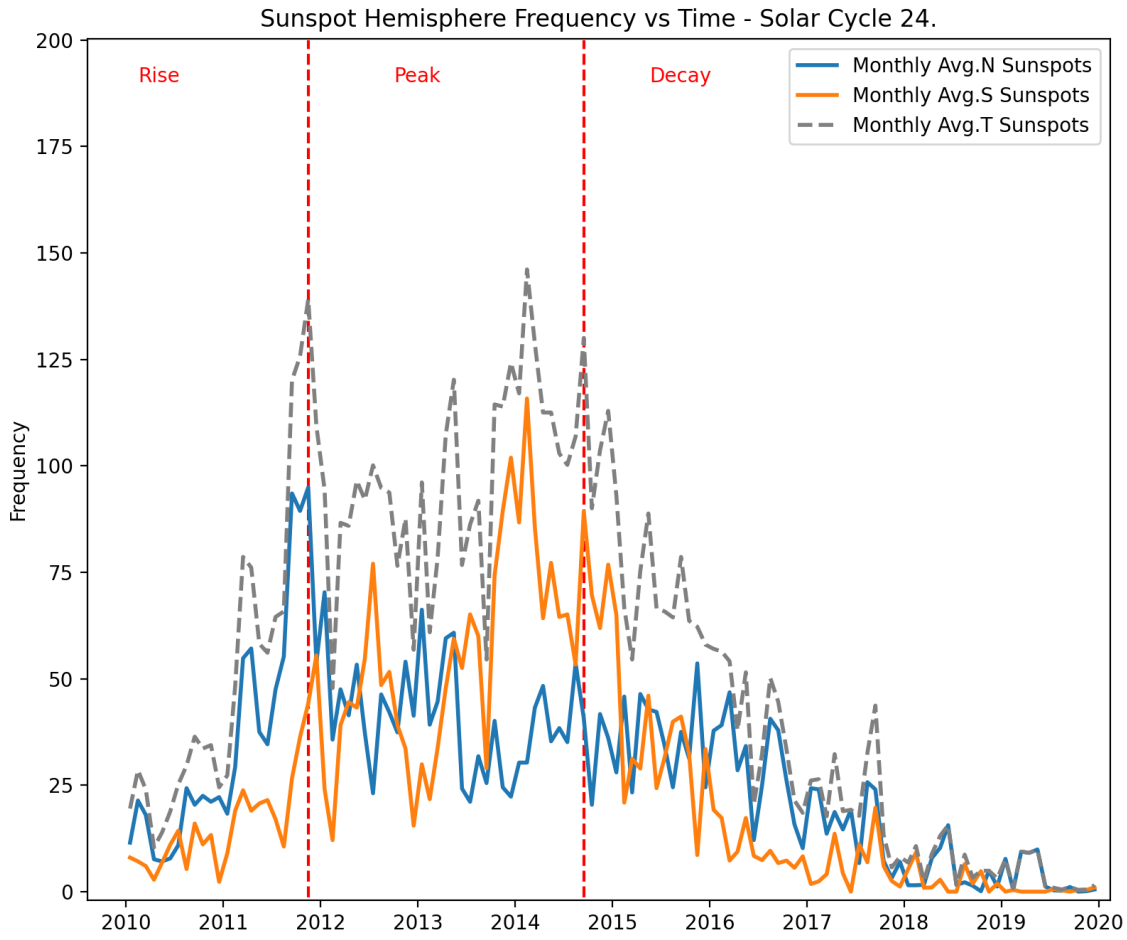

Figure 3.1: Sunspot hemispheric activity (y axis) vs time (x axis). Blue indicates northern activity, orange indicates southern activity. Grey dashed line indicates total combined activity from both hemispheres. Data is obtained from the Sunspot Index and Long-term Solar Observations (SILSO) index(SILSO World Data Center, 2010-2020). Red dashed lines indicate the rise, peak, and decay phases of the solar cycle.

- Finally, the **"Decay"** period is defined to be the long period of decline in solar activity, from 15/11/2014 and extending to the end of 2019. This is the longest phase of solar activity by time, but contains years of very low solar activity.

Variation between the decay and rise phase will be of interest in determining how the slope of change in solar magnetic activity is reflected in parameters of coronal structures observed within those periods ie; do coronal structures observed at similar but rising or falling magnetic activity have different measurable properties?

In subsequent sections, the solar cycle will be discussed by reference to the three phases mentioned above, and coronal structure populations analysed within each phase.

Quantitative measurement of solar hemispheric imbalance has been helped by the creation of N-S activity indexes, first created by (Oliver & Ballester, 1993; Carbonell, Oliver & Ballester, 1993) and expressed as

$$AS = \frac{N - S}{N + S} \tag{3.1}$$

where the activity index AS is expressed as the quotient of the difference between activity in the northern hemisphere (N) and activity in the southern hemisphere (S) and the total amount of activity in both hemispheres. Though this was originally applied to the context of sunspot activity, further examinations of N-S asymmetry have been performed using indices of other solar activity parameters, such as solar wind speed (Nair & Nayar, 2008), solar flares (Joshi et al., 2015), atmospheric solar plasma density (El-Borie et al., 2017), etc. Of these, the sunspot activity index is the most well known and documented indicator of solar magnetic activity, and will be used as a basis of comparison for future analysis of coronal structure activity.

This index can be used as an analogue for magnetic field activity within northern

and southern hemispheres, and analysing the N-S as it pertains to coronal loops provides a unique opportunity to examine differing energy/temperature regimes which might be difficult for other indicators of solar activity.

Measuring and analysing N-S coronal loop indexes as they change throughout time and as they vary from wavelength to wavelength may be beneficial for creating a more nuanced understanding of North-South asymmetry in coronal magnetic fields themselves.

3.2 AIA instrument and image processing.

3.2.1 Image enhancement and MGN processing

As previously mentioned, identifying coronal loops above background noise can be challenging. "Background" noise in AIA images is a combination of diffuse black body radiation from plasma at a lower depth than an emitting structure of interest, and the "dark current" inherent to the detector without any imaged source, as well as contributions from more minor sources such as charge spreading, which is a greater concern for older instruments such as The Transition Region and Coronal Explorer (TRACE) (Gburek, Sylwester & Martens, 2006). This is a combination of difficult viewing conditions and limitations of CCD based image detectors, but the effects of this noise can be minimized with careful image enhancement techniques.

To properly highlight local contrasts whilst preserving global spatial information, a specialized method of image processing must be used. Simple methods of image enhancement involve square root processing where all pixel intensity values are square rooted, or logarithmic processing where all values are expressed as the log of 10 or e. These methods are effective at preserving global features, but are less effective at preserving the features of coronal loops of varying intensity, which is required for effective measurement of these structures.

CHAPTER 3

In the field of machine vision, Gaussian filtering approaches are used frequently for edge detection by filtering out noise and diffuse structures, and this can be applied to solar physics for detecting outlines of coronal loops and other solar structures. This works by convolving a two dimensional image array with a kernel approximating a gaussian function to some number of standard deviations, effectively blurring the image. Several approaches have been created and refined for this purpose; though applying these to AIA images introduces high computational requirements for timely processing. The technique required here should produce a high quality of output, noise reduction, and be computationally efficient.

Multi Gaussian Normalization (MGN), developed and outlined by Morgan & Druckmüller (2014), was chosen to aid in detection of coronal loop structures whose widths are subsequently examined using the level 1.5 image. MGN is a process by which Gaussian filters are applied to an image which is then combined with a weighted gamma transformed image, creating a composite image I, demonstrated in Fig 3.2 and expressed mathematically as

$$I = hC_g' + \frac{(1-h)}{n}\sum_{i=1}^{n} g_i C_i' \tag{3.2}$$

where h is a global weighting value, 0.7 in the case of MGN applications to EUV, though others may potentially be used, $C_{\mathrm{g}}{}'$ is the global gamma transformed image. This is given by multiplying the base image by $\frac{1}{\gamma}$, where γ is some constant, approximately 3.2 in the case of MGN processes. This causes the image to become thresholded, reducing the difference between the brightest and dimmest pixel. C_{g} is the arctan transformation of the base image C, $k$is a weighting variable to determine the severity of the arctan transformation between 0 and 1, and n is the number of unique Gaussian kernel widths used weighted by g_{i} weights.

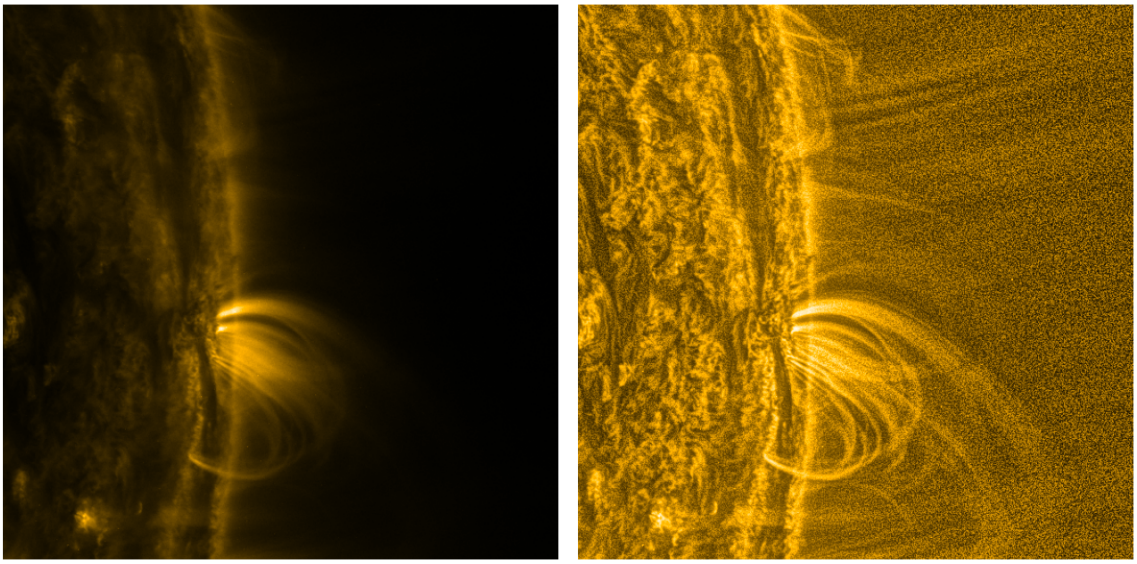

Figure 3.2: A section of the coronal limb and low disc as imaged in 171 Å(left) vs MGN processed level 1.5 (right). Contrasts in coronal structure are evident, local enhancements in the diffuse limb loop structure are highlighted with their structure visually preserved to greater height above the photosphere.

An advantage of using a technique involving multiple Gaussian filters is that background subtraction can be performed using local averages based on the width of the kernel of the filters. Larger filters will be better at smoothing out diffuse signals of intensity and background noise, while small filters are better at detecting and magnifying compact emitting objects. In the context of EUV observations, this technique has been used successfully in studies of Hi-C 2.1 mission data, compared to data of the same time period and region as AIA; greatly enhancing the local contrast and reducing image noise. (see Williams et al. (2020b), Williams et al. (2020a))

Although MGN is used for highlighting local contrast, this can also magnify some preexisting noise in quiet regions of an image (due to poissonian or dark count noise etc). This can be alleviated by performing a time average of multiple MGN images

in sequence. These time averaged images are created from three images sampled 12 seconds apart. These composite images are combined once every three days, allowing for structures to rotate into and out of the viewable annulus in between images, reducing the number of duplicate detections. This results in approximately 1200 composite images per wavelength across the solar cycle. Subsequently, MGN images are be used as a "diagnostic" layer where tracing of loops is performed, but whose coordinates are then employed to reference the corresponding pixels in the matched level 1.5 data itself. This is to avoid the effects of MGN filtering introducing nonphysical structures or altering the geometries of legitimate sources. Each EUV telescope in AIA captures images roughly twelve seconds apart (including exposure time), so although time averaging can lead to a "blurring" of structures which change position or intensity rapidly in this time window, the vast majority of coronal structures visible above the limb are stable within the span of hours, and hence should not be greatly affected. .

3.3 Constraining image data

Each observed image was cropped between 60 and 120 degrees from the solar north pole as in Fig 3.3 (from north, including both east and west limb) as outside of this range the predominance of coronal holes and open plume-like structures increases beyond this range (examined later in Chapter 6). (Antonucci et al., 2020).

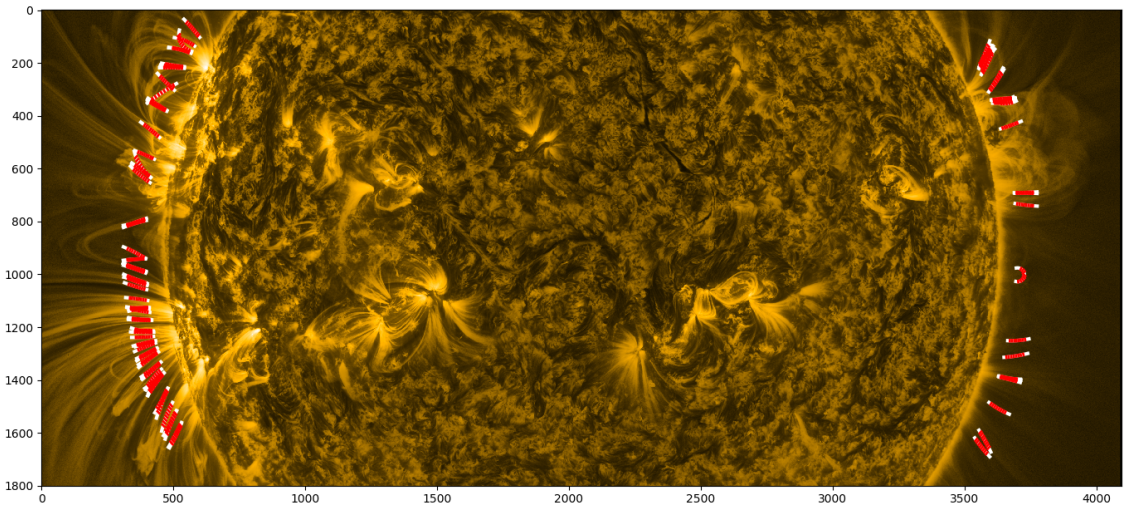

Figure 3.3: Diagram of traced loop structures superimposed on corresponding MGN image of the solar limb and disc in 171 Å. Traced structures (white lines) are used to measure loop widths with an average of cross sections across their length (red dashed lines).

Limb images are constrained to an annulus of a fixed width between 1.05 and 1.10 solar radii (35000 km) above the photosphere. This height also allows for loops to be distinguished from their footpoints, and any emission close to the limb from visually indistinct sub resolution loops and low lying coronal activity (such as from coronal moss and limb brightening effects). This provides optimal conditions for loop fitting procedures outlined below and in Chapter 4.

Within this annulus, normalization can highlight prominent features separately from background noise which would otherwise be present in structures imaged on the coronal disc, ensuring that captured structures are isolated.

The exact relation between latitude, distance from the inner annulus and time taken to clear the annulus is given as

$$t = \frac{\tau}{\pi}\left(1 - \frac{r - r_1}{2(r_2 - r_1)}\right)\left(\frac{sin^{-1}(x_1) - sin^{-1}(x_2)}{cos(\theta_c)}\right) \tag{3.3}$$

where τ is the rotational period at latitude θ_c, r is the pixel position of the object, r_1, x_1 and r_2,x_2 is the radial and cartesian position coordinate of the inner and outer annulus at that latitude respectively. This equates to a time of three days or less for the highest latitudes within the cropped image, and so a time cadence of three days between images will ensure that no structures will appear twice in two consecutive annuli. An example of this annulus fit to a section of the limb is shown in fig 3.4

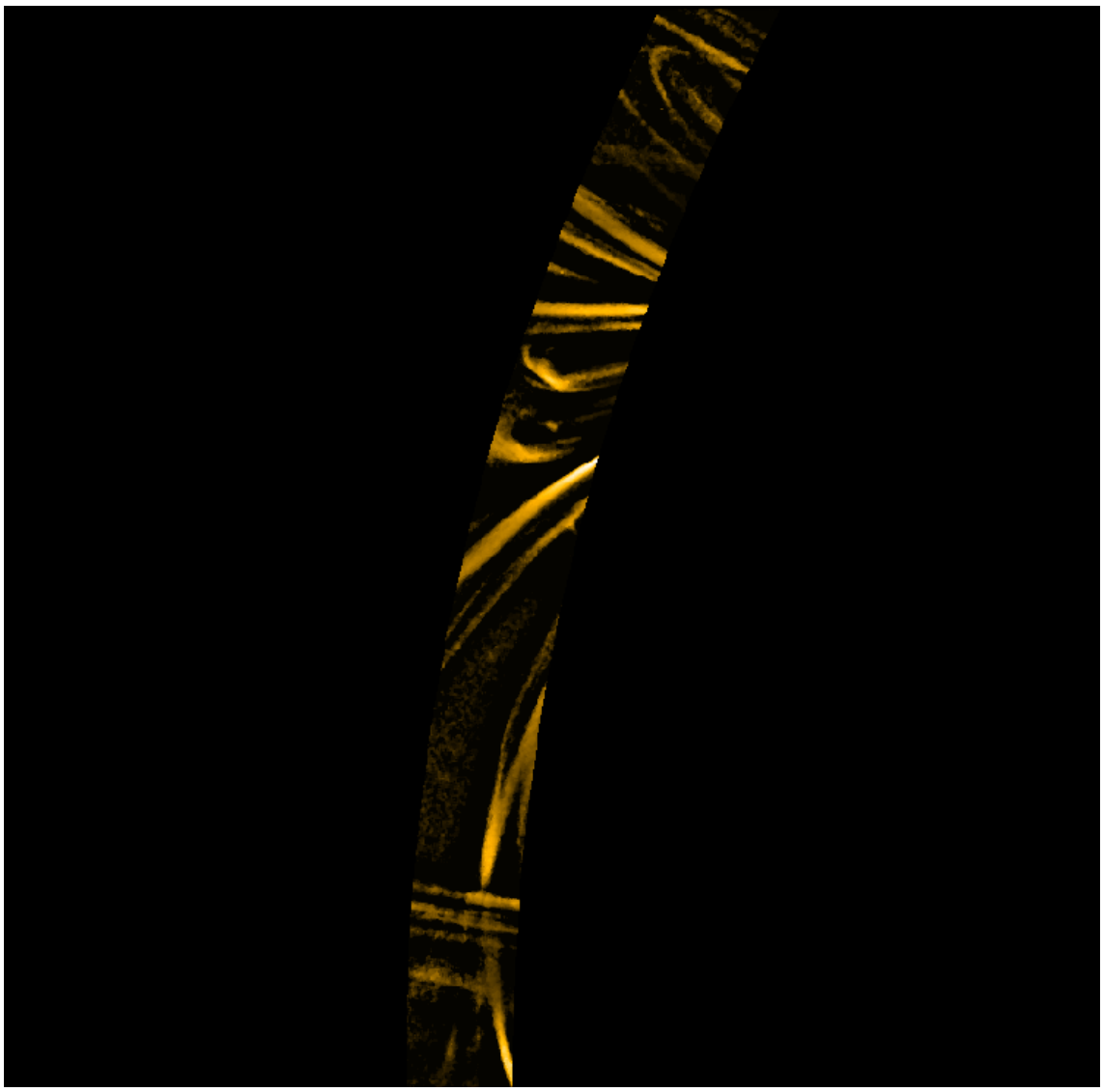

Figure 3.4: A section of the coronal annulus fit to an MGN filtered 171 A image and locally normalized and filtered to highlight coronal strands and other features. This image is used to trace geometry, and is not measured directly for structural properties.

Due to the variable lifetimes of coronal structures (which can range from hours to days or more depending on the openness and degree of interaction with other nearby structures) (Nakariakov & Kolotkov, 2020; López Fuentes, Klimchuk & Mandrini,

2007) it is necessary to confirm if a structure is no longer present along the line of sight in subsequent images. The height of the annulus and the time sampling of images (3 days based on eq 3.3) allows for structures to pass out of the from the field of view from one selected dataset to the next, regardless of the differential rotation rate at its particular latitude or the lifespan of the emitting structure.

3.4 Width measurements

The prerequisite for determination of power law profiles of bulk width measurements is a clear definition of "width" and reliable method of measuring them. In this work width is defined as as the derived width of some function fit between measured minima of cross sectional brightness profiles from identified structures.

As there is some uncertainty with regards to the "expected" cross sectional shape of a coronal loop , an alternative method which was explored but not then used is to employ spline fitting between minima of intensity cross sections to approximate loop geometry. This has the advantage of making no assumptions about the underlying morphology of the coronal structure being measured, and is generally better at dealing with asymmetrical formations.

One major disadvantage of fitting splines is that no consideration is made for noise or uncertainty in the data to which the spline is being fit. Interpolating splines between small numbers of data points can be unreliable, leading to asymmetrical intensity profiles, especially relevant in this case when most coronal structures are measured between 2 and 4 pixels wide in the 0.6″ resolvable limit of the AIA SDO instruments. Additionally, measurements of width are mostly subjective using this method, based on estimates of full width half max rather than values derived from a function. It can also be challenging to estimate uncertainties of spline fitting compared to function fitting.

Thus in the following a Gaussian approach to loop geometry is introduced, which

has the advantage of precise parameter fitting with uncertainties easily calculated from least squares iteration. By assuming a coronal loop is consistent with a Gaussian profile, the various parameters of the profile such as amplitude and width can be fit and extracted by automatic fitting routines. This will benefit examination of trends in loop populations by providing a realistic uncertainty in their derived parameters.

If coronal loops are considered to be Gaussian in cross sectional density profile; then the intensity of emission as a function of x displacement from the center of the profile can be described as

$$f(x) = a.\exp\left(-\frac{(x-x_p)^2}{2w^2}\right) \tag{3.4}$$

where a is the height of the Gaussian profile, x_{p} is the central position of the loop profile, x is the position away from the central position, and c is the standard deviation of the Gaussian profile. Though it should be noted that there are other possible interpretations of the morphology of coronal loops (Klimchuk & DeForest, 2020), Gaussian profiles are well fit to observed loop cross sections, even down to Hi-C resolutions; where it is possible to attempt to fit multiple Gaussian profiles to single cross sectional profiles due to the high pixel resolution of the instrumental data. (Williams et al., 2020a).

In many studies of coronal loops, identification and tracing is performed by hand, or semi-automatically in pre-defined regions of interest around active regions. To fully utilise the full extent of the AIA dataset over Solar Cycle 24, it is necessary for identification and tracking to be performed fully autonomously upon an image. In this case, the investigation of coronal geometry utilises a modified version of the OCCULT algorithm (Aschwanden, 2010), that is OCCULT-2, (Aschwanden, De Pontieu & Katrukha, 2013), which performs well in coronal loop detection in multiple EUV wavelengths. By approximating coronal loops as curvilinear segments,

geometries can be fit by the OCCULT-2 method; iterating through all possible loop parameters in a predefined range for an optimal approximation of loop geometry. The annulus based approach can constrain some issues of complex loop geometry by fitting shorter, well defined loop segments, but cannot account for closed structures which re-enter the annulus at a different location. This is a consequence of using coronal limb image data instead of coronal disc data, but this effect can be seen even in the use of advanced, contemporary loop tracing algorithms applied to both real and synthetic active region data.(Aschwanden & Peter, 2017; Zhiming et al., 2019) An example of a region of traced loops on a region of a composite MGN annulus is shown in Fig. 3.5.

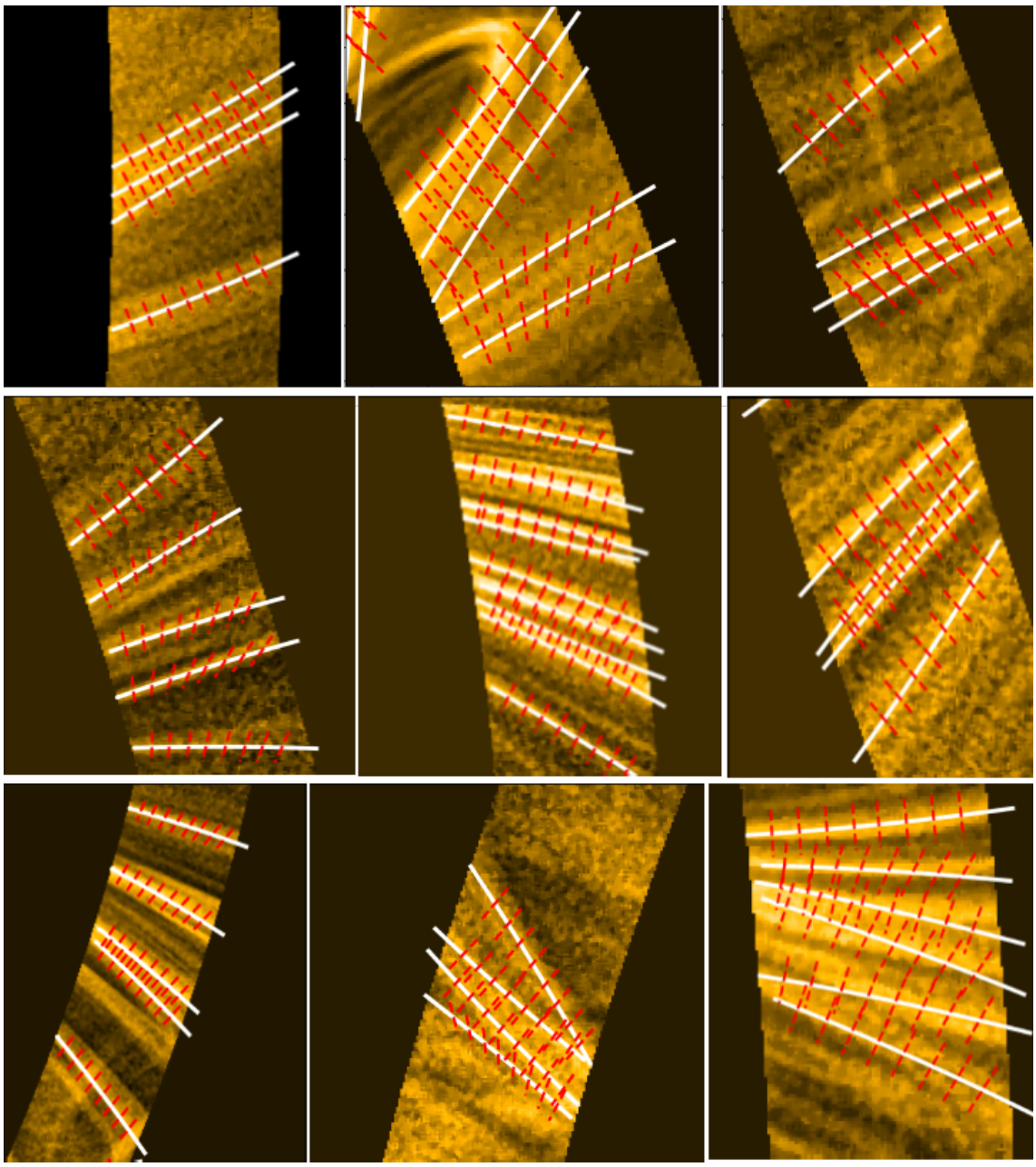

Figure 3.5: Multiple subsections of the coronal annulus overlaid on post-processed MGN image data containing traced curvilinear structure in white, and the corresponding width cross section coordinates in red dashed line. Cross sectional coordinates used to measure intensity in corresponding unaltered level 1.5 images.

Once a loop segment is traced, eight equidistant cross sections are used to measure intensity values taken from level 1.5 and averaged. Background is estimated by linear interpolation between local minima, and a Gaussian profile fit to the reduced profile to estimate width. After this, a corrected profile is produced, which subtracts the value of the calculated background from the corresponding cross section. A gaussian profile is then fit to the peak which appears closest to the center of the cross section, taken to be the structure closest to the traced geometry.

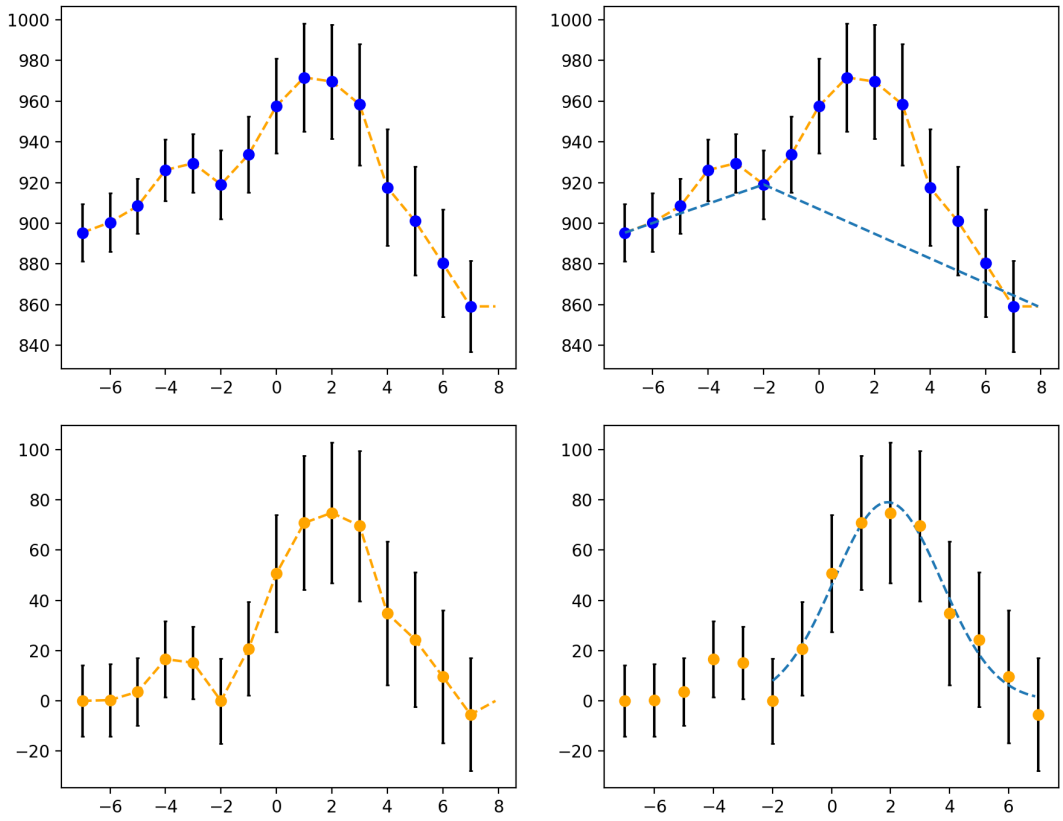

Figure 3.6: A coronal loop flux profile created by averaging 8 cross sectional segments (a), linear background applied between minima (b), background subtracted profile (c), and gaussian fit profile (d). Standard error for each point indicated by uncertainty bars.

Uncertainties in histogram bins used to explore possible power law slopes are calculated according to the errors associated with the fitting of individual Gaussian profiles to loop cross sections. Uncertainty in loop width measurements originates in the closeness of the fit of the optimal Gaussian profile utilizing a least squares best fit algorithm, and uncertainties of that fit are based upon the standard error of the covariance matrix of the sum of difference between actual profile and fit profile. From these uncertainties of loop widths, errors in width bin frequency (number inside a given bin) - used to calculate the power law slope of the distribution - are calculated by determining the probability that a single width value falls into an adjacent bin assuming a normal distribution of potential values within its error range. The mean average of these probabilities for all widths within a bin constitute the percentage uncertainty of a particular bin, meaning the numerical error is equal to the uncertainty probability p multiplied by the number of structures in that bin N. A standard error of square root n is also applied as a "safety" for uncertainty to frequency; to ensure that measurement errors better represent a process of image tracing and width extraction in which uncertainty can be difficult to quantify. The final uncertainty for each bin frequency is then represented by Equation 3.5

$$\Delta N = \bar{p}N + \sqrt{N} \tag{3.5}$$

where ΔN is the uncertainty of the frequency, $\bar{p}$ is the mean average probability of falling outside of a bin threshold, and N is the total frequency of coronal structures within a bin.

3.5 Colatitude Measurements

Measurements of angular position for structures in this work are denoted by their polar colatitude ϕ, defined as the angular distance from the North Pole. Some angles

provided as in excess of 180 or less than 0 are indicative of structures towards the East limb from the South or North pole respectively.

Chapter 4

COSDA Design and Development

4.1 Introduction and Requirements

This chapter describes and documents the development of the scientific code COSDA (COronal Structure Detection and Analysis) employed to process and evaluate solar images for automatic structure location determination and parameter measurement and recording. It will outline the decisions made during this design process and aid the reader in understanding the methodology employed in the project.
The technical requirements of the code can be summarized as follows; in order to satisfy the research aims of this research,

- The approach must be capable of reading EUV fits images from a number of sources, but primarily 171 Å, 193 Å, 211 Åand 304 ÅEUV AIA images throughout Solar Cycle 24.
- The code must be capable of isolating regions of interest for identification and examination, extracting structures within that region consistently without manual intervention.
- The examined structures must be curated to prevent spurious and nonphysical detections from contaminating the dataset.

- Resulting datasets must contain structural widths, latitudes and intensities for all coronal structures detected and recorded.
- The approach must be able to process image data of sufficient quantity to be both statistically significant and allow for adequate comparison to other indicators of solar activity.
- The code will utilize Python 3, to allow for ease of accessibility, and standardization of techniques with libraries such as SunPy(The SunPy Community et al., 2020; Mumford et al., 2020), AstroPy(Astropy Collaboration et al., 2013, 2018, 2022), Numpy(Harris et al., 2020) amongst others.
- Code must be modular, allowing for different techniques and parameters to be utilized and hence increasing the flexibility and utility of the resulting code for current and future work.
- Code must be computationally efficient, and hence maximize the amount of useful statistics which can be analysed, and allow for large quantities of image data to be analysed on desktop PC environments.

An overview of the main functional operation of the algorithm is demonstrated visually in Figure 4.1, divided into into two sections, Image Processing and Structure Detection. Of these two sections, four subsections (Pre and Post Processing, Geometry Tracing and Function Fitting) are described in the following, detailing each of the steps qualitatively. More detailed breakdowns of sections 4.3 and 4.4 in the style of Figure 4.1 are available in the Appendix (see Figures 1, 2).

4.2 Pre-Processing

The stage of pre-processing involves the opening and handling of AIA EUV image files, the process of calibrating these files up to level 1.5, and in MGN processing

Figure 4.1: Workflow diagram of one iteration of the COSDA program, equivalent to processing one day of data.

each of these individually to form a time averaged MGN image ready for further manipulation.

These files are in the form of .fits and are handled using SunPy and Astropy fits handling procedures. The time cadence of the survey is once per three days (as mentioned previously in Chapter 3), but for each three day snapshot, three images are chosen in close succession. These images are each prepared using the standard AIAprep calibration procedure, which is performed using the AIApy library (Barnes et al., 2020). MGN (see Chapter 3) is chosen due to its high computational efficiency and its performance in enhancing faint structures and local contrasts. This is performed on each of these images individually, as the MGN process enhances the effect of random noise present within each image, and so time average of three distinct MGN images will reduce the S/N ratio of this random noise compared to signal from coronal structures which are persistent in all three images. As the images are taken within 40 seconds of each other (12 second time cadence between AIA images in most wavelengths), the effect of structural evolution or disappearance is minimized. The time averaging process then minimizes the effect of the MGN enhanced random noise of the image, and though three images were chosen for the basis of the composite, more images can be used depending on the storage and computing capacity available, and the sensitivity of the chosen parameter to time. A copy of one of the level 1.5 AIA images (the middle of the series of three images) is preserved and will be used for determinations of structural widths, positions, and intensity measurements. All MGN image products and their derived images are used exclusively for the purposes of identification and determination of structure location. The modular components of this substage include the image enhancement/time averaging process, which could be altered/improved depending on the exact requirements of the data surveyed and improvements to image enhancement packages widely available.

4.3 Post Processing

The stage of Post Processing involves further image enhancement techniques to refine the dataset and extract useful features. In the case of this work, the presence of coronal structure was emphasized. To isolate certain regions, the latitude of the images is cropped to create submaps between certain pixel ranges depending on which of the regions are required, preserving either the closed active region or the open polar region (1148:2948 vertically for Closed Active Region; 2948:1148 horizontally for Open Polar Region). Once cropped, the time averaged MGN images are constrained with an annulus between 0.05 and 0.10 solar radii above the limb, to further constrain the dataset and control for distinct coronal structures. This does not allow for structural heights to be determined. The annulus allows for structures to pass out of the survey from one three day period to the next, regardless of the lifetime of these structures. Data within the annulus is normalized and the normalized annulus segment is further enhanced by subtraction of broad 80 pixel kernel, (representing a gaussian function with a FWHM of 80 pixels) to allow for very broad blurring) Gaussian filters, which highlight the sharpness of continuous coronal structures and minimize diffuse noise by means of Gaussian subtraction, which subtracts an image which has been convolved with a gaussian kernel from its unconvolved image, sharpening structures of interest and preserving positional information. This causes pixel intensity values in areas without significant structure to become negative, which is used to judge the quality of fit in subsequent tracing. The result of these processes is an edge optimized annulus layer, with positive pixel values corresponding to the luminous centers of structures, and negative pixel values corresponding to more dim background regions. This layer is used exclusively as a diagnostic tool to aid in geometric tracing described more fully in the next section,

Bright points close to the inner boundary of the annulus ring are considered as potential starting points for loop segments. These points are iterated through and

the tracing performed on each point. From these traced loop segments, structure width measurements are made at eight points equidistant from each other along the traced path. These are performed using cross sections, perpendicular to the coordinates of the coronal segment. An average intensity profile is then constructed by averaging the values of the cross sections passed back to the level 1.5 image.

4.4 Geometric Tracing

The geometric tracing step has been primarily adapted from methods discussed and developed in the OCCULT, OCCULT-2, and other prior algorithms created for the detection of curvilinear geometries in solar image data (Aschwanden et al., 2008; Aschwanden, 2010, 2016; Aschwanden & Peter, 2017) This stage of geometric tracing involves the initialization of the construction of the inner annulus of the Edge Optimized Annulus Layer, which includes all pixels within a three pixel band of the innermost annulus within the range of normalized pixels. These points are then examined for intensity, and arranged in numerical order from highest to lowest in value.

An example of the intensity values of a typical inner annulus region is demonstrated in the form of a histogram in Figure 4.2. From the peak of the histogram, a value of 0.4 is chosen as the threshold for new structures to be traced; ie, pixels are used as the basis of potential starting points until their normalized intensity is 40 percent of the brightest pixel in that range. This value was chosen as it represented a point below which which new positive detections were not found in large quantities. Future work may involve examining these threshold values more carefully in different wavelengths and time periods.

From there, these brightness values are used as the starting points for potential structures, and the initial fitting process is employed. This process detects the latitude of the bright point, and begins to iterate through line segments of a fixed

length (usually 15 pixels long) at varying angles in a range around the recorded angle of the potential structure, using the intensity of the edge optimized annulus layer to determine which angle results in the greatest recorded intensity.

Once this has been determined, the angle of this line is used as the basis for structure tracing. In the open polar regions, where straight lines are used as approximations for plume geometry, then iteration begins. If a curvilinear (circle segment) geometry is used as the basis for structure tracing (as is the case in the active/closed regions), then a further iterative step is performed to find the optimal direction and radius of the linear segment, again selecting the parameters of the segment with the optimal intensity. The function of this structure is extrapolated, adding one more pixel to the structure at a time, and determining the intensity of the coordinate specified. A structure is considered "completed" when the new pixels have reached the outer edge of the annulus. As each pixel intensity is measured, it is possible that new pixel intensity values are negative. A "buffer" of allowed negative pixel values is tolerated, so that structure tracing can continue so long as the number of negative pixels does not exceed a total or continuous amount (such as 15 total or 5 continuous for active regions), the specific value depending on the region and instrument used. This allows for tolerance of noise introduced in the image processing section, or smoothing effects, which might interfere with a successful structure detection, whilst simultaneously screening most spurious structure detections.

If a point is found to be unsuitable for tracing (by reaching a number of continuous or total negative pixel values chosen arbitrarily), the structural tracing attempt is discarded and this point is removed from subsequent tracing attempts. If tracing is performed to one of the boundary edges of either the inner or outer annulus, the structure is considered successfully traced at this stage and the pixel locations of the structure are recorded. This is typically the outer annulus, however. Subsequently,

the values of intensity in the coordinates of the corresponding MGN reference frame are discarded to prevent multiple tracing attempts of the same structures.

Unsuccessful traces at this stage have their starting coordinate and five pixels surrounding it deleted from the edge optimised annulus layer (intensity set to -1), and the next geometry tracing attempt is made on the next brightest pixel. Successful traces have eight equidistant cross sections determined from the start to the end of the structure to prevent coincidental overlappings or other incidentally coinciding emission from distorting the profile of the structure along its length, whose coordinates are used to reference intensity values from the initial level 1.5 image. These successful structures have every coordinate from their structure and some range surrounding them deleted from the edge optimized annulus layer, to avoid many repeat detections within the same area. A more detailed breakdown of this section in a visual format is available in the Appendix (see Figure 1).

4.5 Profile Fitting

After the intensities of the eight equidistant cross sections are retrieved from their corresponding positions within the level 1.5 image, they are averaged to produce a composite cross sectional intensity for the structure along its entire length. This cross section is fifteen pixels across, and may capture many adjacent structures, or structures which are not fully resolved from the prominent brightness. To ensure that only one structure is measured from a single cross section, points are interpolated between the available raw data pixels with a spline, and then background subtraction is performed by means of linear interpolation between minima of this profile. This essentially assumes a linear slope of intensity between the two minima of the cross section which is simpler than other methods such as cubic or spline fitting, but this makes fewer assumptions about the underlying conditions in the line of sight and cannot reduce the intensity of any point of the profile below zero. Only the positions

of the reduced profile which correspond to the positions of the original measured intensity profile are selected for geometry tracing, producing a reduced cross section.

A Gaussian profile is then fit to this reduced cross section, fit by a least-squares best fit algorithm using the Levenburg-Marqardt damped least squares method (LM-DLS; Levenberg (1944)), implemented with the scipy optimize library, which was chosen due to the high degree of robustness and reliability, capable of fitting Gaussian functions accurately to profiles that are not well centered or possess an unusual shape. This ensures that as many of these profiles have as well fit functions as possible.

Once the profile has been fit, parameters such as the full-width half maximum, the amplitude, and the uncertainties are extracted using the covariance matrix. The width of the structure is defined as two times the full width half maximum of the Gaussian fit by % of profile, as this is a good approximation for the full size of a Gaussian profile, and is straightforward to extract from function fitting software with attached uncertainties. Uncertainties for these widths are also used for determination of uncertainties in the histogram bins of loop width distributions as described in Chapter 5, and are extracted from the covariance matrix of the fitting procedure. Once a fit structure has been found and the parameters recorded, the coordinates and several surrounding coordinates are deleted from the edge optimised annulus layer. Once all points within the inner annulus down to the 0.4 normalized intensity threshold have had an attempt at geometry and profile fitting, then all stored structure parameters (width, uncertainty of width, latitude, intensity, and date) are exported, and the run is completed. A more detailed diagram of this stage of the code is provided in the Appendix (see Figure 2).

If a series of days are specified, then the program will run on the next day in the given list. The program outputs a standard CSV format text file, and so the results are easily accessible to all editors and interpreters. Links to copies of these results

are included in the Appendix (see Appendix B; Section 9.2).

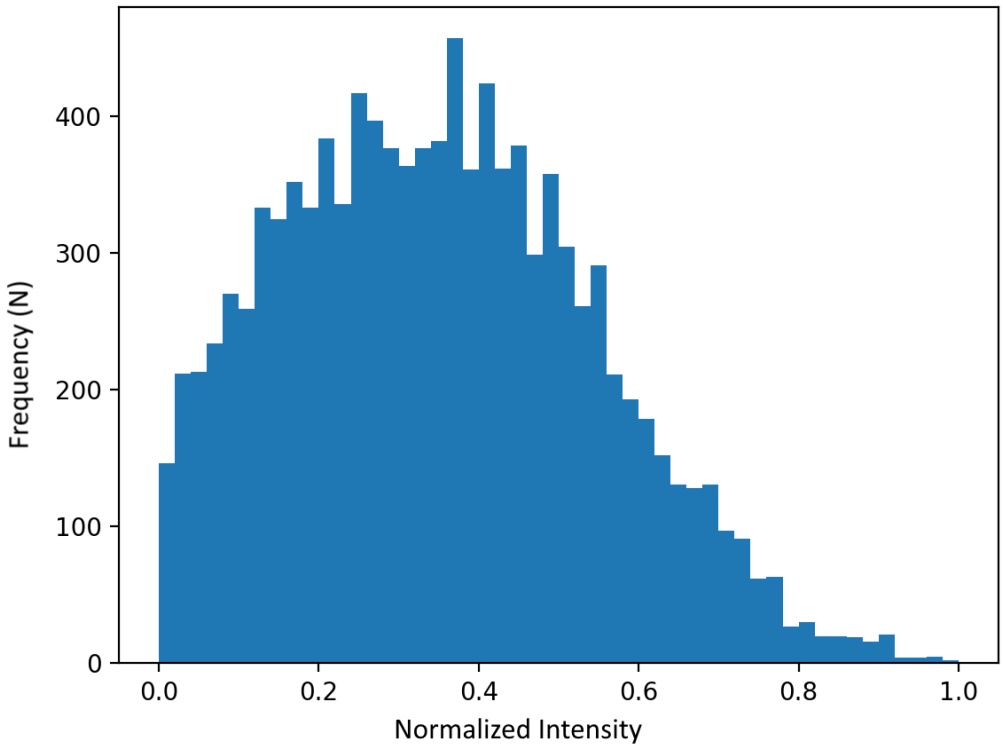

Figure 4.2: Histogram of the normalized intensity values (x axis) vs frequency (y axis) of pixels within a typical inner annulus region, used for the starting position of potential structures for later tracing attempts. Note the peak at around 0.4 and the distribution skewed towards lower values of intensity.

4.6 Efficiency and Optimization

Standard Python libraries such as Numpy have been supplemented by implementation of bridging libraries such as Numba (Lam, Pitrou & Seibert, 2015), and the OpenCV library (Bradski, 2000) which bridge between Python, Assembly, and C++/C respectively. These implementations have sped up native Python routines

considerably (a factor of 10 - 100), especially for the MGN portion (20 seconds per iteration to 2 seconds per iteration on standard AIA resolution images), resulting in full dataset processing reduced from 3.5 days to 8 hours, plus other calculation and image steps (such as structure fitting and tracing). Further optimization is attained using extensive parralelization of the initial dataset by means of loading each day of the cycle as an individual process to be completed by a large array of individual cores (12 - 16 cores utilized in a standard run of the COSDA algorithm). Parallelization in this way is much more efficient than other methods, as there is no synchronization requirement between processes. This method should continue to increase in efficiency with larger CPU capacity, and can scale effectively from personal device scales (laptops etc) to desktop environments, to high performance computing clusters. Future optimization could include smaller kernel sizes, layers, and subtraction steps. Other packages used include; Sunpy, Aiapy, Astropy and Scipy.

The COSDA algorithm used for the production of data used in this thesis is hosted at `github.com/DanGass/ThesisCode`.

Chapter 5

Active Region Structures

In this Chapter, the methods and techniques introduced in the previous Chapters are employed to perform a study of coronal structures imaged within a selected range above and below the solar equator, typically aligning with the active region belts. This is performed across the entirety of Solar Cycle 24, and the results are used to analyse a characteristic distribution of coronal structural widths within this predominantly magnetically closed region. Code and Results provided. [1]

5.1 Introduction

Active regions are areas of predominantly closed magnetic activity, and the active region belts are areas occurring roughly thirty degrees above and below the line of the equator (van Driel-Gesztelyi & Green, 2015) populated by active regions. These are affected by the phases of magnetic activity of the solar cycle (as described with sunspot activity see Figure 3.1). The solar magnetic field can vary in strength drastically by region and altitude, and this can be seen in the active region and the corona above it. This region of the corona experiences very strong magnetic flux, with the field associated with some structures showing 600-700 Gauss composed of

[1] `https://github.com/DanGass/ThesisCode`

both transverse and lateral magnetic components (Kuckein et al. (2009)), compared to average field strengths in the range of 60-150 Gauss for most structures (Brooks, Warren & Landi, 2021) within the active region. These regions are also associated with a high degree of dynamism with high temperature and velocity variations within plasmas and structures, which makes it a particularly compelling region for research into the interactions of plasma with these strong magnetic fields. (Seaton et al., 2021; Higginson et al., 2017)

Regions of magnetic activity can exhibit highly complex braiding behaviours within magnetic filaments on a wide variety of spatial scales, which may contribute to coronal heating (Chitta et al., 2022). Magnetic flux tubes emerging from around sunspots show high degrees of interaction and complex magnetic topologies. A combination of motions from photospheric Alfvén waves contributing to AC Heating, (Milano, Gómez & Martens, 1997) to the magnetic tension causing local reconnections and realignments of the magnetic field and dissipation between current sheets contributing to DC nanoflare (Moriyasu et al., 2004) and Joule heating (Kanella & Gudiksen, 2019), is likely to contribute to the heating of coronal plasma. As heated plasma fills the flux tubes which contain them, this plasma radiates at specific wavelengths, and observable coronal structures are formed. The placement and observed width of these structures may therefore be informative of the physical processes and the magnetic conditions which produced them.

In the following Sections, the automated procedures described in the previous Chapter are applied to a dataset of approximately 1000 images per wavelength, representing one image every three days across Solar Cycle 24 and the results described and analysed. Results will be organized into structural width profiles, positional distribution profiles, and other results and correlations which are used to verify the validity of the method and the approach used. Subsequent Chapters will analyse and discuss the results in context with each other, as well as statistical examinations

of data correlations and their physical significance for the study of coronal physics.

5.2 Results

5.2.1 Structural Widths

The total number of loops detected by wavelength is demonstrated in Figure 5.1, and Table 5.1. This represents every positive detection of a structure which was recorded by the COSDA algorithm described in Chapter 4.

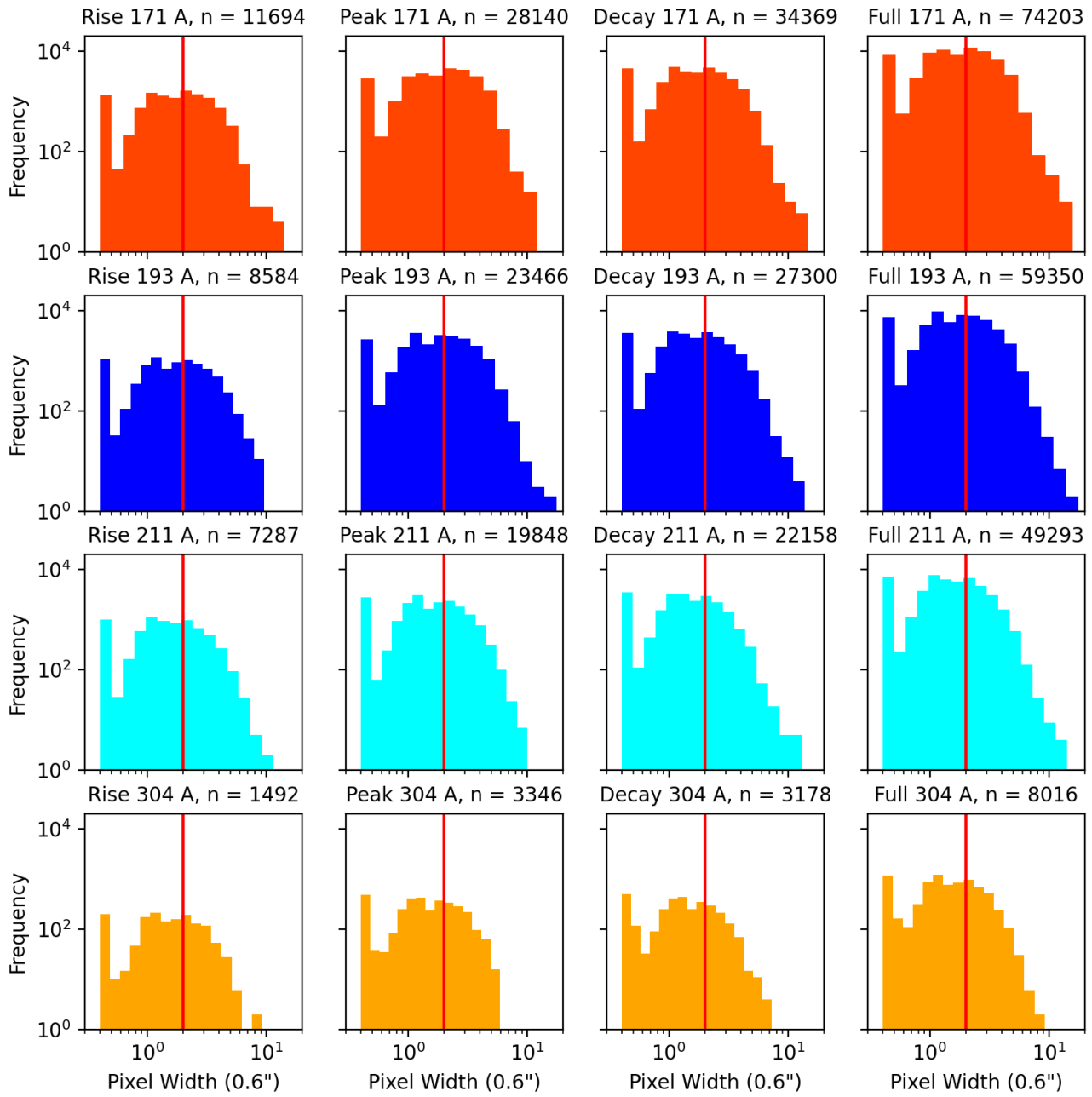

Figure 5.1: Width frequency diagram of all AIA structure widths (AIA pixels). Red line at 2 pixels shows the peak of the thresholded population. Total range unsuited to fitting with power law description, with widths "missing" from high and low width ranges. Note "spike" in left hand side, likely an artifact of Gaussians fitting across narrow peak ranges (see Chapter 4).

Table 5.1: Loop frequency by wavelength and phase.

Wavelength (Å)	Rise	Peak	Decay	Total
171	11694	28140	34369	74203
193	8584	23466	27300	59350
211	7287	19848	22158	49293
304	1492	3346	3178	8016

A peak of 2 pixels (red line in Figure 5.1) is imposed by a combination of technical instrumental resolution limits such as diffraction scattering and noise such as CCD charge spreading which causes loop width broadening effects as defined by Equation 1.1, which leads to thresholding of the distribution. As a result, structural widths recorded from AIA data have a lower confidence limit of 2.7 pixels (Aschwanden & Peter, 2017), roughly 1.6", or 2300 km. As seen in analyses of Hi-C data (Williams et al., 2020b,c), coronal structures can possess widths smaller than this, but these widths cannot be confidently measured and accepted in the overall distribution in the AIA distribution. The full histogram has fifty bins between log(2) and log(10), which are maintained in subsequent ranges and analysis. This ensures that binning effects are controlled for as much as possible.

More detailed examinations of loop populations and their power laws can be made by restricting the sample to the range of 3 - 6 and 2.7 - 5 pixel widths; where the physical and observational effects described above are minimised, and so more accurate examination of power law slope slopes can be carried out. See Tables 5.2 and 5.3 for 3-6, and 2.7-5 pixel ranges. 3-6 range is shown to demonstrate what impact that constraining the range of width values to avoid thresholded regions can have on fit power law slopes.

Table 5.2: Loop frequency by wavelength and phase. Loop widths between 3 and 6 pixels.

Wavelength (Å)	Rise	Peak	Decay	Total
171	2262	6496	5522	14302
193	1417	4350	3397	9971
211	874	2497	2043	5431
304	156	361	91	608

Table 5.3: Loop frequency by wavelength and phase. Loop widths between 2.7 and 5 pixels.

Wavelength (Å)	Rise	Peak	Decay	Total
171	2730	7787	6890	17430
193	1774	5509	4965	12280
211	1124	3302	2840	7285
304	234	495	340	1071

Figures 5.2 and 5.3 present the distribution of the loop populations derived, organised by wavelength and by phase of solar activity. This collection represents one of the largest set of coronal loop data available for analysis across Solar Cycle 24.

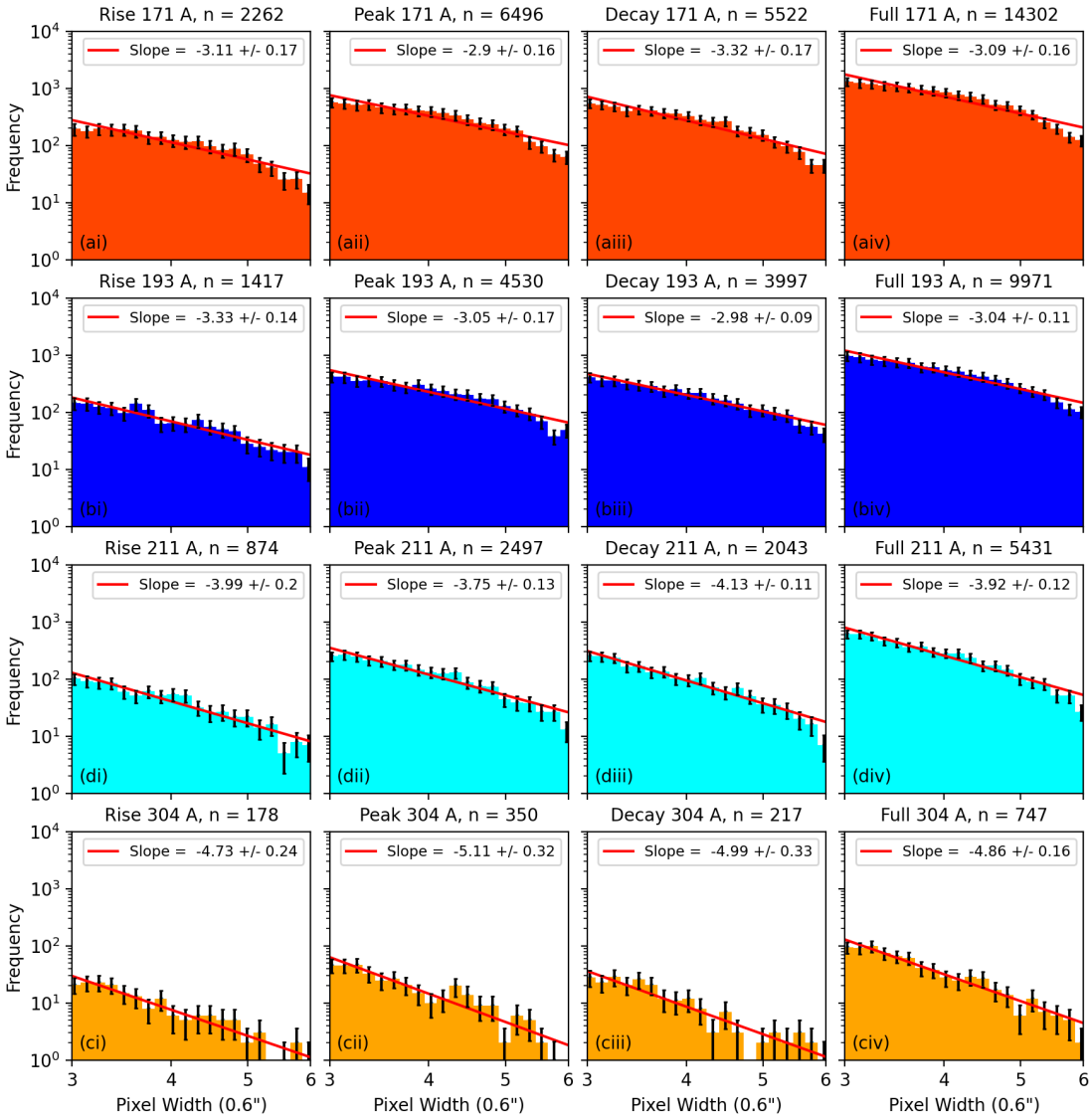

Figure 5.2: Width frequency diagram with a cutoff from 3-6 pixel widths. Fitted slopes are steeper than the other range, and the differential slope is closer to (2.9 - 3.3). Variation throughout solar cycle persists throughout different wavelengths.

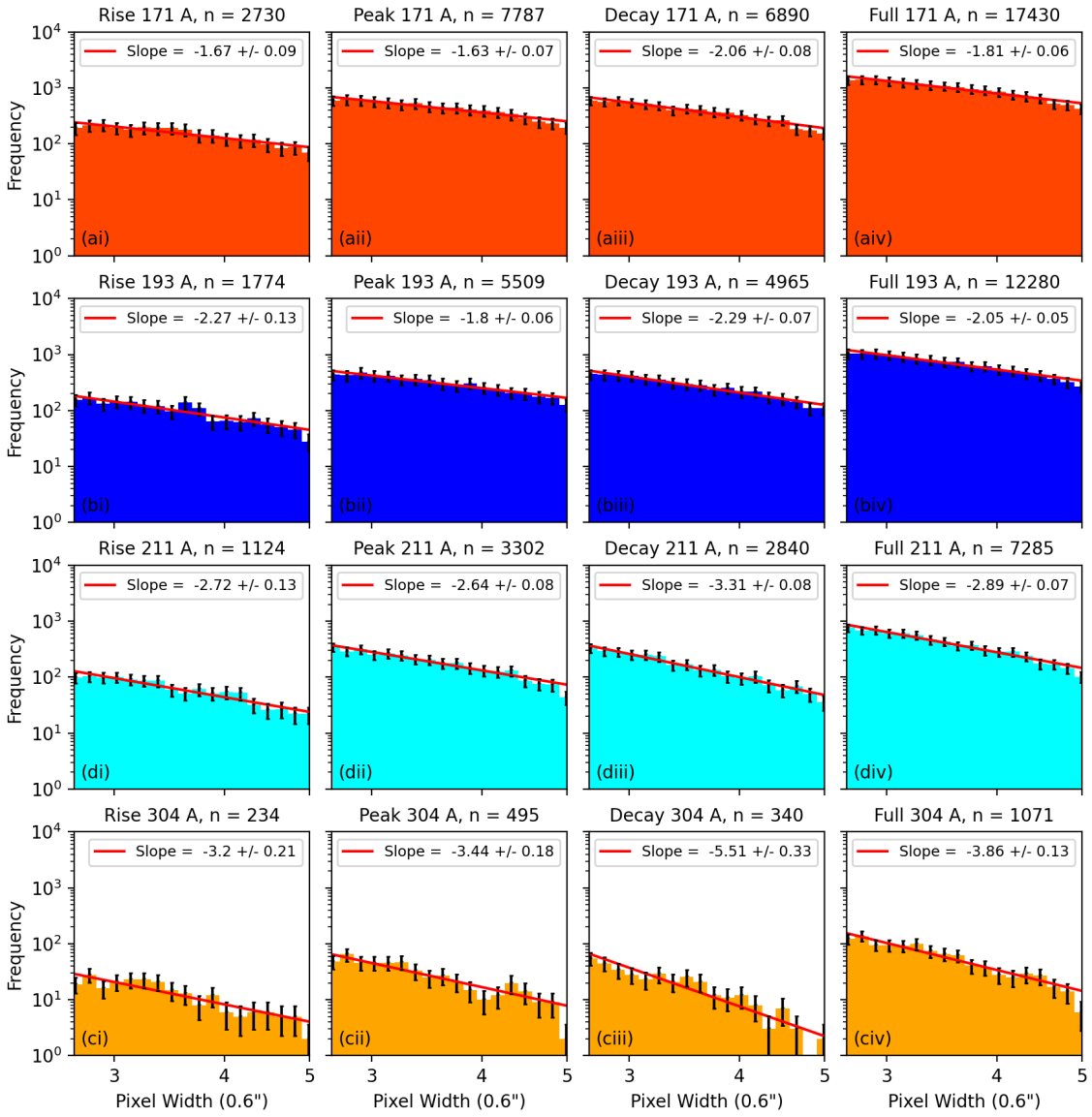

Figure 5.3: Width Frequency Diagram with a cutoff from 2.7-5 pixel widths. At this level the differential slope is closer to the ideal SOC case of around 1.5. Variation throughout solar cycle is persistent through different wavelengths but shows more consistency than the wider range.

In Figure 5.3, there are a few specific discrepancies between these observations and the fit power law, namely a lower frequency of loops that are 2-3 pixel widths

and greater than 4 pixels in width. Though the phenomenon of loop emergence and its reliance on underlying coronal conditions is difficult to approach analytically, the value of the slope of the line of best fit of a population of loop structures is an emergent property of these structures that can be measured and analysed. It can be considered to be comprised of the characteristic value of the underlying SOC power law and the cumulative influence of applicable physical and observational effects that can influence observed loop widths.

Values for the 3-6 case (Figure 5.2) are more similar to previously obtained works by Aschwanden & Peter (2017) and Zhiming et al. (2019), who obtained power law profiles with slopes of 2.7 to 3.1 in populations of one active region in AIA 193 Åusing automated tracing algorithms. This combined with results from Williams et al. (2021) could suggest that steeper slopes may be a result of thresholds caused by observational effects.

Results of SOC slopes presented in Table 5.5 are fit between 2.7 to 5 pixels, the range of highest confidence. Though the variation between these populations is only a few hundred for most wavelengths and time phases, the thresholding of the distribution results in large changes to the resulting slopes.

Table 5.4: Width frequency power law slope by time phase and wavelength - 3-6 pixel widths

Wavelength (Å)	Rise	Peak	Decay
171	3.11 ± 0.17	2.90 ± 0.16	3.32 ± 0.17
193	3.33 ± 0.14	3.05 ± 0.17	2.98 ± 0.09
211	3.99 ± 0.20	3.75 ± 0.13	4.13 ± 0.11
304	4.73 ± 0.24	5.11 ± 0.32	4.99 ± 0.33

Table 5.5: Width frequency power law slope by time phase and wavelength - 2.7-5 pixel widths

Wavelength (Å)	Rise	Peak	Decay
171	1.67 ± 0.09	1.63 ± 0.07	2.06 ± 0.08
193	2.27 ± 0.13	1.80 ± 0.06	2.29 ± 0.07
211	2.72 ± 0.13	2.64 ± 0.08	3.31 ± 0.08
304	3.20 ± 0.21	3.44 ± 0.18	5.51 ± 0.33

In 171 Å; the power law slope slope was recorded in the rise phase as 1.67 ± 0.09 between 2.7 - 5 pixels. By contrast, the peak phase has a shallower slope than the rise phase, with a value of 1.63 ± 0.07 This value is close to agreement with the ideal FD SOC case of 1.5. The decay phase has a steeper slope of (2.06 ± 0.08) than both rise and decay, corresponding to lower frequency of high width structures visible within this phase. The decay phase is marked by a lower frequency of sunspots, and a lower overall number of detected loops in 171 Åper time unit. The trend between phases, with rise slopes being higher than peak slopes, and peak slopes lower than decay slopes is notable if it is assumed that the widest coronal loop populations should occur when sunspot (and hence magnetic activity) is highest in the peak phase, rather than the decay phase.

In 193 Å; it is expected and observed that due to similarities in temperature of the majority of loops seen in this wavelength and those of 171 Å, power law distributions derived from these two wavelengths are similar in trend, though the values are steeper. The rise phase power law slope is 2.27 ± 0.13, which is steeper than the same phase in 171, which seems to indicate a lower number of wide structures in this phase in 193. The peak phase slope of 1.80 ± 0.06 is similar, if slightly steeper than that produced by the same phase in 171 Å. This is more in agreement with earlier expectations that a higher temperature loop population should display similar properties. This phase also coincides with a high degree of active corona activity and flaring. Finally, the decay phase slope of 2.29 ± 0.07 is steeper than that of the same phase in 171. This appears to be due to relatively more wide widths observed. Overall, the 193 Åis in agreement with the trends present in 171 Å, the power law slope of rise is steeper than peak, but shallower than decay. The number of loops seen in 193 is lower than in 171 by roughly 1-2 thousand in each phase, though the relationship indicated by the power law slopes is still similar.

In 211 Å;The power law slope for the rise phase is 2.72 ± 0.13 , indicating an increase of close to one above rise values in 171 and consequently lower relation between high width and frequency. The peak phase for 211 Åhas a steeper slope (2.64 ± 0.08) than the rise phase, steeper even than those seen in the decay phases of 171 and 193. This might indicate that peak phase magnetic activity is more conducive to the creation or detection of wide, high temperature structures than the rise phase. The decay phase shows similar trends in power law slope (3.307 ± 0.082) to the other wavelengths in that it is steeper than rise, and appears to be more well fit than the Rise phase with a lower uncertainty. This deviation may be due to a lower number of wide loops in the Rise phase owing to small statistical effects, or it may indicate that high temperature structures of higher widths are rarer in the earlier and later stages of the solar cycle.

304 Åloops, given their low population compared to other wavelengths, cannot provide the same analyses or level of discussion that can be made with other wavelengths and this is reflected in high uncertainties. The Rise phase slope (-3.199 ± 0.206) is shallower than the Peak phase slope (-3.441 ± 0.184), and the Decay slope slope (-5.513 ± 0.327) is steeper than both. In general, the relationships between phases seem to mirror those seen in other wavelengths, but exact values such as power law slope slopes are based on much lower loop frequencies and have large uncertainties, indicating poor fitting.

The phases of peak and rise contained lower slopes than the decay phase. These trends are examined in more detail in discussion below. Of interest is the change in width across the time phases which are broadly mirrored across the four wavelengths with the exception of the underpopulated 304 phase.

5.2.2 Positional frequency and Asymmetry

Also recorded is the latitudinal occurrence of widths, from 0 degrees at the solar north pole to 180 degrees at the solar south pole, combining both the east and west limb. This allows for the examination of north-south asymmetry of coronal structures in the three phases of the solar cycle across multiple wavelengths. These locations and widths alongside corresponding sunspot observations from the same time phases can be examined in comparison to well known north-south asymmetry indicators across the solar cycle.

Quantitative measurement of this imbalance has been helped by the creation of general N-S activity (see Equation 3.1). A loop asymmetry index then is the difference in the number of northern and southern loops divided by the total number of loops defined below,

$$A_s = \frac{N_s - S_s}{N_s + S_s} \tag{5.1}$$

Where the coronal structure asymmetry A_s is the quotient of the difference between the number of northern structures N_s and the number of southern structures S_s and the sum of northern structures and southern structures.

Whether coronal loops are seen to have greater or lesser asymmetry in different phases of time or in different wavelengths could provide some insight into the relation between magnetic activity and the relative population of coronal loop populations across various wavelengths. Sunspot data is commonly derived from HMI (Schou et al., 2012) and white light data (Zharkov, Zharkova & Ipson, 2005), and represents the relative abundance and surface area of each sunspot by position. This data can be used to evaluate positional and asymmetry data for each unit of time in the solar cycle. This data is derived with the method and sources detailed in Hathaway (2015), with more recent observations made available through the Sunspot Index and Long-term Solar Observations (SILSO) (SILSO World Data Center, 2010-2020). The asymmetry is examined in more detail in Figure 5.4 examining the total and average frequencies in the north and south hemispheres for observed coronal loops (compare to Figure 3.1, which examines the total sunspot frequency by hemisphere for Solar Cycle 24). It can be seen in both of these figures that the overall activity of the solar cycle is biphasic, with the northern hemisphere (blue) population greater on average throughout the cycle than the southern hemisphere, but it peaks earlier and begins decaying soon after the start of the "peak" phase, whereas the southern hemisphere only peaks in activity towards the start of the decay phase, with both hemispheres decaying to negligible activity by the end of Solar Cycle 24.

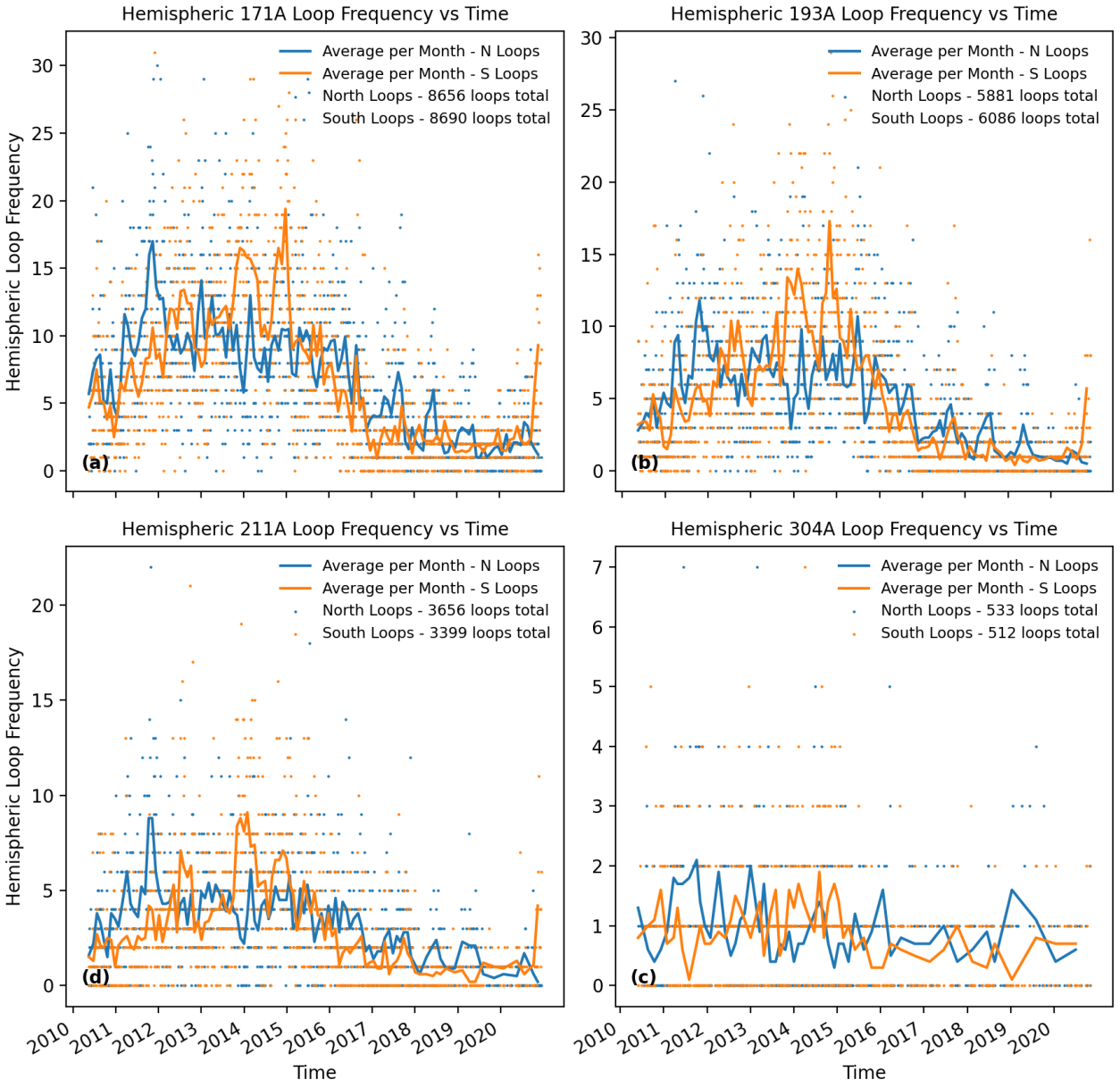

Figure 5.4: Hemispheric loop frequency vs time for all wavelengths. Blue indicates northern activity, orange indicates southern activity. Dots and lines indicates loop counts by day and monthly average respectively. All loops are above 2.7 pixels in width.

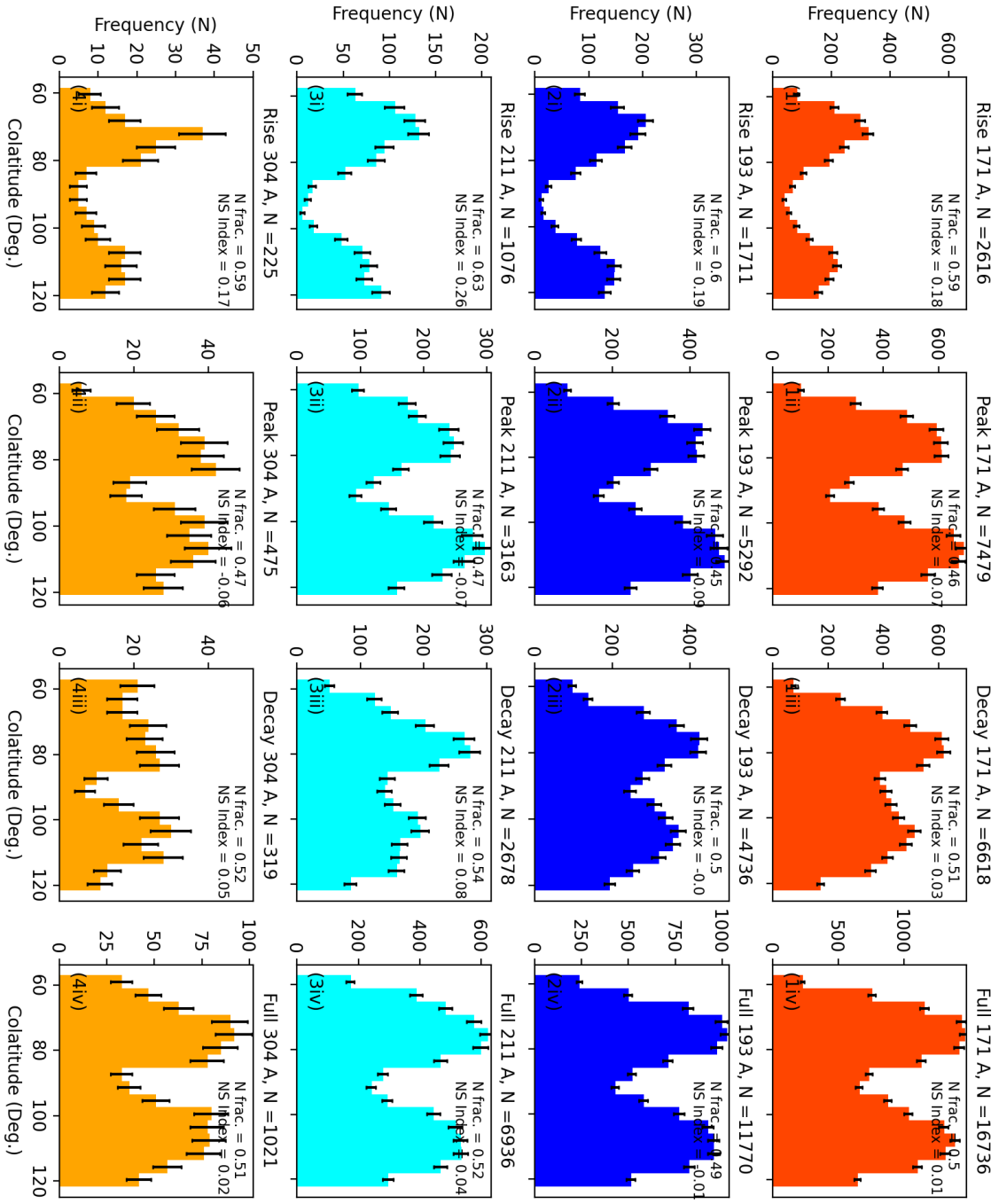

Figure 5.5: Positional frequency diagram stacked with width population for all coronal loops above 2.7 pixel widths by wavelength and phase. $\sqrt{N}$ error indicated by error bars.

Table 5.6: North-South loop asymmetry in three time phases. Left column F represents north hemisphere loops as a fraction of total loops. Right column represents N-S loop asymmetry index for chosen phase and wavelength.

Wavelength	Rise		Peak		Decay	
	F	A	F	A	F	A
Sunspots	0.68	0.36	0.37	-0.27	0.73	0.46
171 Å	0.59	0.18	0.46	-0.07	0.51	0.03
193 Å	0.60	0.19	0.45	-0.09	0.50	0.00
211 Å	0.63	0.26	0.47	-0.07	0.54	0.08
304 Å	0.59	0.17	0.47	-0.06	0.52	0.05

171 Åloops Figure 5.5(1) in the rise phase show a large bias towards northern loops with a fractional northern representation of loops of 0.59; representing 59 percent of identified coronal structures in this time phase. The asymmetry index of this phase is 0.18. This is lower than the rise phase sunspot asymmetry index of 0.36 (see Table 5.6). Loops within the peak phase show a reversal of the previous north dominated phase, with a fractional northern frequency of 0.46, though only 8 percent biased towards the south, this represents a change of 17 percent from the previous phase. This could indicate a resurgence in the activity in the southern magnetic field during this time phase and/or a decrease in northern activity. In the decay phase, northern loops become the larger fraction of loops overall with a fractional northern frequency of 0.51 and an asymmetry index of 0.03. This appears to be caused by a sudden drop in the number of southern loops rather than a collapse in the number of northern loops, which maintain similar numbers in this phase compared to the previous phase.

193 Åloops in the rise phase largely mirror the relation seen in the 171 population; with a higher amount of northern loops, predominantly occurring within the

70-75 degree colatitude range, with a fractional northern frequency of 0.59 and an asymmetry index of 0.18. This is only slightly higher than the value for 171 over the same phase, and indicates that coronal loops in 193 occupy similar latitudinal positions to those visible in 171. The peak phase of 193 possesses a fractional northern frequency of 0.45 and a N-S index of -0.07. This is the greatest deviation from northern dominated loop frequency - even though this value is much less proportionally biased than the most northern lead population. The decay phase of 193 has a fractional northern frequency of 0.5, with a N-S index of 0, indicating no overall change between north south, though this could be due to high southern activity in the beginning of the phase being counteracted by sustained northern activity throughout the rest of the phase. The overall distribution of loops is very similar to that seen in other wavelengths.

211 Å follow the same trend displayed in the other wavelengths, with some small deviations detailed as follows; The rise phase displays the highest fractional imbalance towards northern loops of any of the wavelengths, with a fractional frequency of 0.63 for northern loops - with a corresponding N-S asymmetry index of 0.26. This value is still lower than typical values seen in other asymmetry indices such as sunspots; which is 0.36 for this time phase. Given the exaggerated frequency of northern loops in the rise and decay phase compared to other wavelengths, the peak phase fraction is higher than both 171 Åand 193 Ådistributions with a fractional northern frequency of 0.47 and an asymmetry index of -0.07, The decay phase follows the same distribution as described in previous wavelengths, with a lower frequency of loops overall, but with proportionally less southern loops than in the previous phase. The values of N frequency of 0.54 and a north-south asymmetry index of 0.08 are greater than those seen in 171 and 193, but less than those seen in the rise phase.

304 Å As discussed in previous sections, unreliability of 304 Åpopulations due

to small sample size limits the amount of analysis that can be reasonably applied to the data set. Overall, the rise phase (0.59 northern fraction, 0.17 asymmetry index) peak (0.47 northern fraction, -0.06 asymmetry index) and decay phase (0.52 northern fraction, 0.05 asymmetry index sections exhibit similar broad trends to those seen in other wavelengths, though the exact values of fractional northern frequency and N-S asymmetry are likely not reliable indicators of properties of structures in this wavelength as a whole. Further studies with a more robust methodology of 304 Åstructure detection would add to the value of comparison with other wavelengths.

Overall, loop positional frequency follows a consistent pattern from the rise phase to the decay phase. Northern dominance of loop populations is replaced by slight preference for southern loop populations in the peak phase, caused by a high number of northern loops being outnumbered by a large, temporary increase in southern loop population. This increase is quickly reversed in the decay phase, with overall loop populations decreasing, but southern loops decreasing more rapidly as a proportion of overall loop position.

5.2.2.1 Coronal Structure Versus Sunspot Asymmetry

Another method of analysing coronal structure distribution is by comparison to other indicators of solar magnetic activity, such sunspots. More detailed examination can be made by compilation of sunspot coverage and loop frequency by position and comparing it to analogous measures of positional coverage for coronal structures. This can be investigated firstly in terms of asymmetry indices, which can reveal the overall trends in EUV structure populations broadly. Such an examination of asymmetry index by year can be seen in Figure 5.6 and Table 5.7

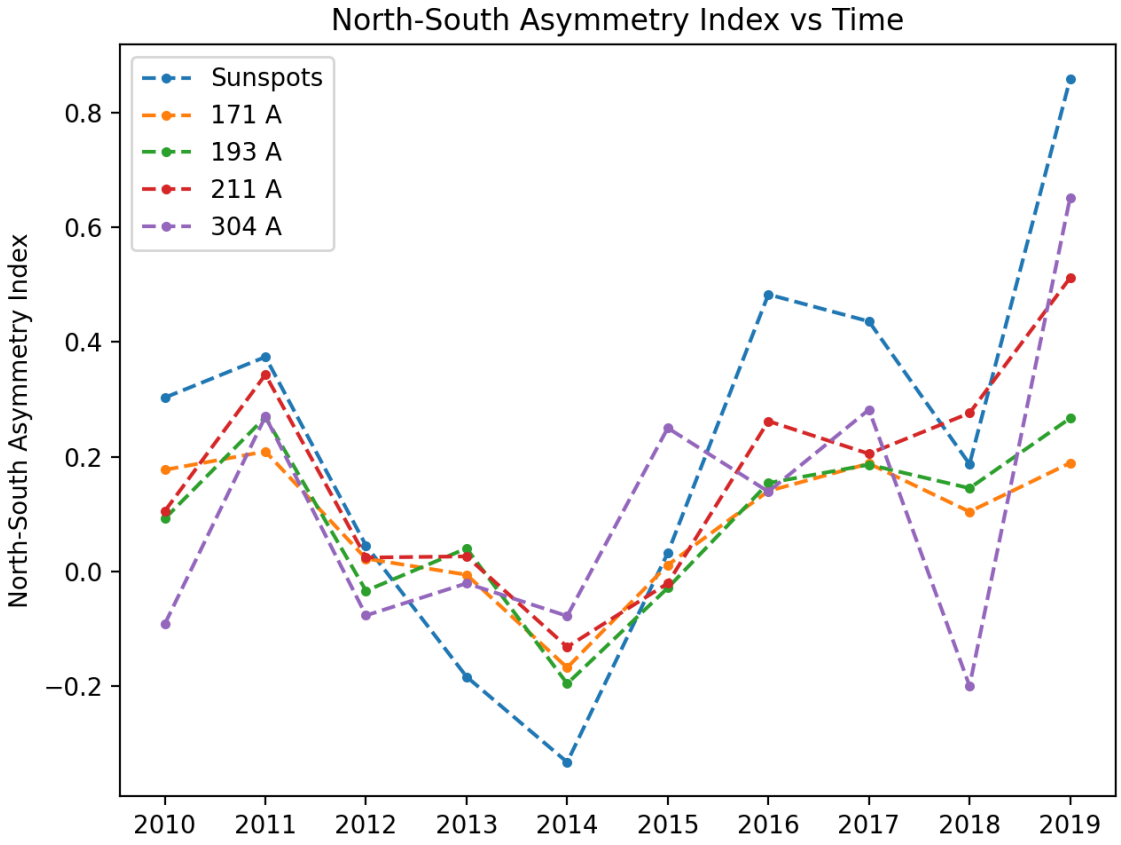

Figure 5.6: North-South Asymmetry Index (y axis) values versus Time (x axis) for all wavelength populations and sunspots (coloured dashed lines).

Table 5.7: North-South asymmetry by year for sunspots and coronal structures in different wavelengths. Left column F represents north loops as a fraction of total loops. Right column A represents N-S loop asymmetry index.

Year	Sunspots		171 Å		193 Å		211 Å		304 Å	
	F	A	F	A	F	A	F	A	F	A
2010	0.651	0.303	0.588	0.177	0.55	0.1	0.554	0.107	0.454	-0.092
2011	0.687	0.374	0.601	0.202	0.626	0.252	0.664	0.328	0.646	0.291
2012	0.523	0.045	0.508	0.016	0.481	-0.038	0.509	0.018	0.461	-0.078
2013	0.408	-0.184	0.5	0.001	0.522	0.043	0.512	0.024	0.493	-0.014
2014	0.333	-0.333	0.417	-0.165	0.404	-0.193	0.436	-0.127	0.465	-0.07
2015	0.516	0.032	0.505	0.01	0.486	-0.027	0.493	-0.014	0.625	0.25
2016	0.741	0.483	0.57	0.139	0.581	0.162	0.628	0.256	0.571	0.143
2017	0.718	0.436	0.594	0.188	0.595	0.19	0.603	0.207	0.641	0.282
2018	0.594	0.187	0.548	0.097	0.571	0.141	0.638	0.275	0.4	-0.2
2019	0.929	0.859	0.591	0.182	0.622	0.244	0.75	0.5	0.826	0.652

Figure 5.6 and Table 5.7 demonstrate the distribution of the asymmetry indices on a more granular scale ie; yearly instead of by phase. Plotted by year, every wavelength is seen to generally follow the trend shown in sunspot figures, to a lesser extent. -0.333 in sunspot figures in 2014 compared to -0.165, -0.193, -0.127 and -0.07 for 171, 193, 211, and 304 Årespectively. Similarly in 2017, sunspot asymmetry index values were 0.436, compared to 0.188, 0.19, 0.207 and 0.282 in 171, 193, 211, and 304 Å. The phase of 2014-2016 represents a large change in asymmetry from broadly southern lead to broadly northern lead, and the values of the populations of coronal and chromospheric structures broadly follows this trend, but to a lesser extent, showing less rapid changes in coronal asymmetry and never to the same magnitude, with the exception of 211 Åin 2018, which was a phase of very low

activity generally and so may be subject to fluctuations caused by small variations in frequency.

These highlight some disparity both between the observed coronal structures and sunspots, and between coronal structures observed in differing wavelengths despite overall agreement. Sunspots possess a more exaggerated asymmetry, with more distinct changes in slope between phases of north and south lead activity - this can be seen in both the sudden rise and decay of southern activity in 2014 which is represented to lesser extents in coronal structures seen in this phase.

The magnitude of coronal loop asymmetry indices shown (positive or negative) exceed sunspot indices only twice across every year and in all wavelengths - 211 Åin 2018 (0.275 vs 0.187) and 304 Åin 2015 (0.25 vs 0.032). In both of these instances, the frequency of one or both of the samples was low (2018 had a very low number of both sunspots and 211 structures, and 304 Åhad low numbers of observed structures throughout the solar cycle). Additionally the 2012-2013 phase saw a sharp decrease in sunspot asymmetry (0.045 to -0.184) which was not represented by any wavelength, instead increasing or remaining relatively constant (171 Åasymmetry index also decreased in this phase, but only from 0.016 to 0.001; remaining positive).

Coronal structure diagrams measuring the position in more detail could also be constructed, and be comparable to the well known Maunder "Butterfly" diagram (Maunder, 1904; Hathaway, 2005), which tracks the relative area covered by sunspots per unit area at every point of solar colatitude over time. Figure 5.8 shows the frequency of loops by cocolatitude over time for each of the four wavelengths represented (171 (a), 193 (b, 304 (d) and 211 (c)). It is a two dimensional histogram of detected loop width cocolatitude (60-120 degrees with 1 degree bin height) versus time (2010-2020 with 1 month bin width). The intensity of the pixel indicates the natural exponent of the frequency of loops within each bin. Overplotted is a line of

best fit for both northern and southern hemispheres, calculated by performing linear regression on the pixels with the highest umbra sunspot coverage (yellow pixels, greater than 0.1 percent) for both hemispheres, equivalent to those calculated for sunspot colatitude coverage data presented in Figure 5.7.

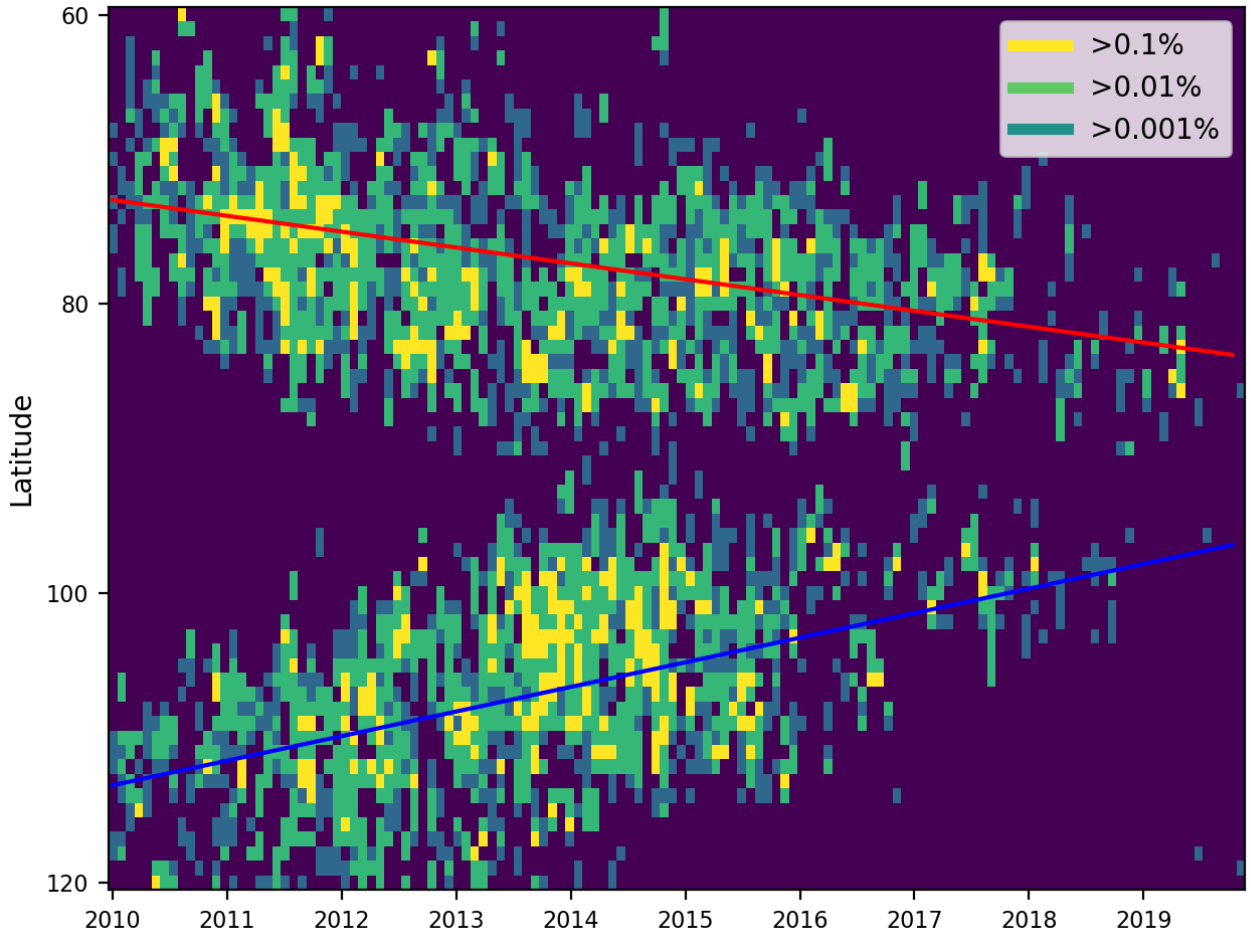

Figure 5.7: Diagram of sunspot umbra area coverage (pixel colour) by colatitude (y axis) and time (x axis) over sunspot coverage data of the same phase. Line of best fit calculated across yellow pixels (greater than 0.1 percent coverage) in each hemisphere.

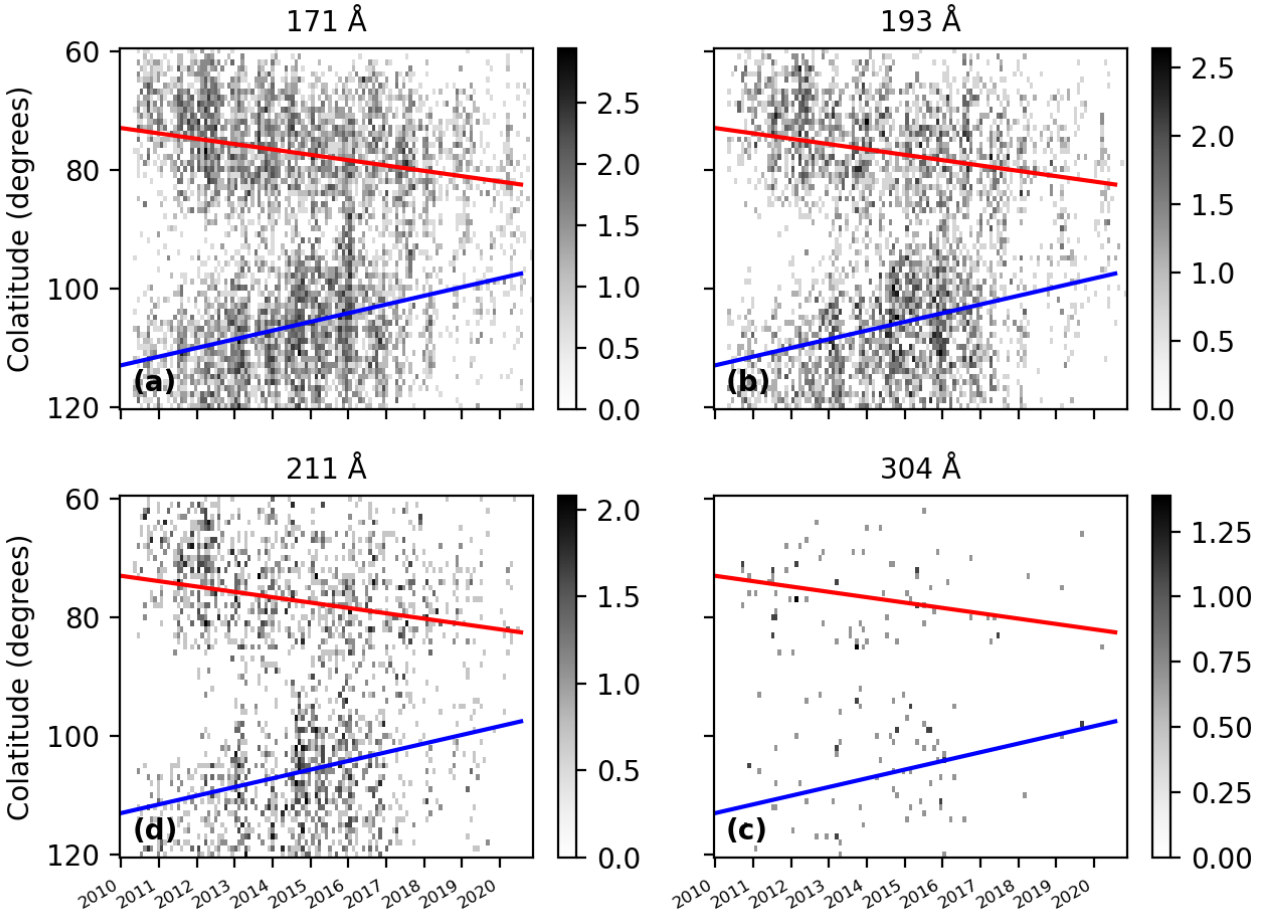

Figure 5.8: Diagram of loop detection frequency by colatitude and time for all four wavelengths, represented in natural log of frequency. The red and blue lines indicates the slope of sunspot data in the north and south hemisphere - identical to that fit in Figure 5.7 over sunspot coverage data of the same phase.

The slope and intercept for the southern hemisphere (blue) is -0.13 and 374.3, and the northern hemisphere (red) is 0.08 and -87 respectively. It is seen that coronal loops bear considerable visual similarity to the sunspot distribution - following a similar if slightly broader distributions (40-30 degrees displacement from the equator at the start of the solar cycle, migrating to 15 degrees displacement at the end of

the cycle), consistent with Spörer's Law (Ivanov & Miletsky, 2014). In particular, coronal loops are seen at low frequencies across the whole range of colatitude s at all phases, though they are concentrated at positions which correspond to sunspots as would be expected.

5.2.3 Coronal Loop Width Versus Colatitude Frequency

The relationship between coronal loop width and colatitude occurrence has not been frequently studied. A result of the construction of our extensive loop dataset is that investigation of long term trends of population properties can be studied, including the width and colatitude . It is understood from previous study of solar sunspots and well known relationships between sunspot frequency and coverage (Maunder Butterfly Diagrams, Spörer's Law, etc..) that these values have direct links to colatitude and solar cycle. The width distribution of a loop population may indicate the degree of activity within emerging active regions or sunspots from which these coronal loops emerge. Investigating whether this distribution changes as a function of the colatitude that loops emerge could highlight any disparity between the conditions at coronal loop footpoints at varying colatitude s.

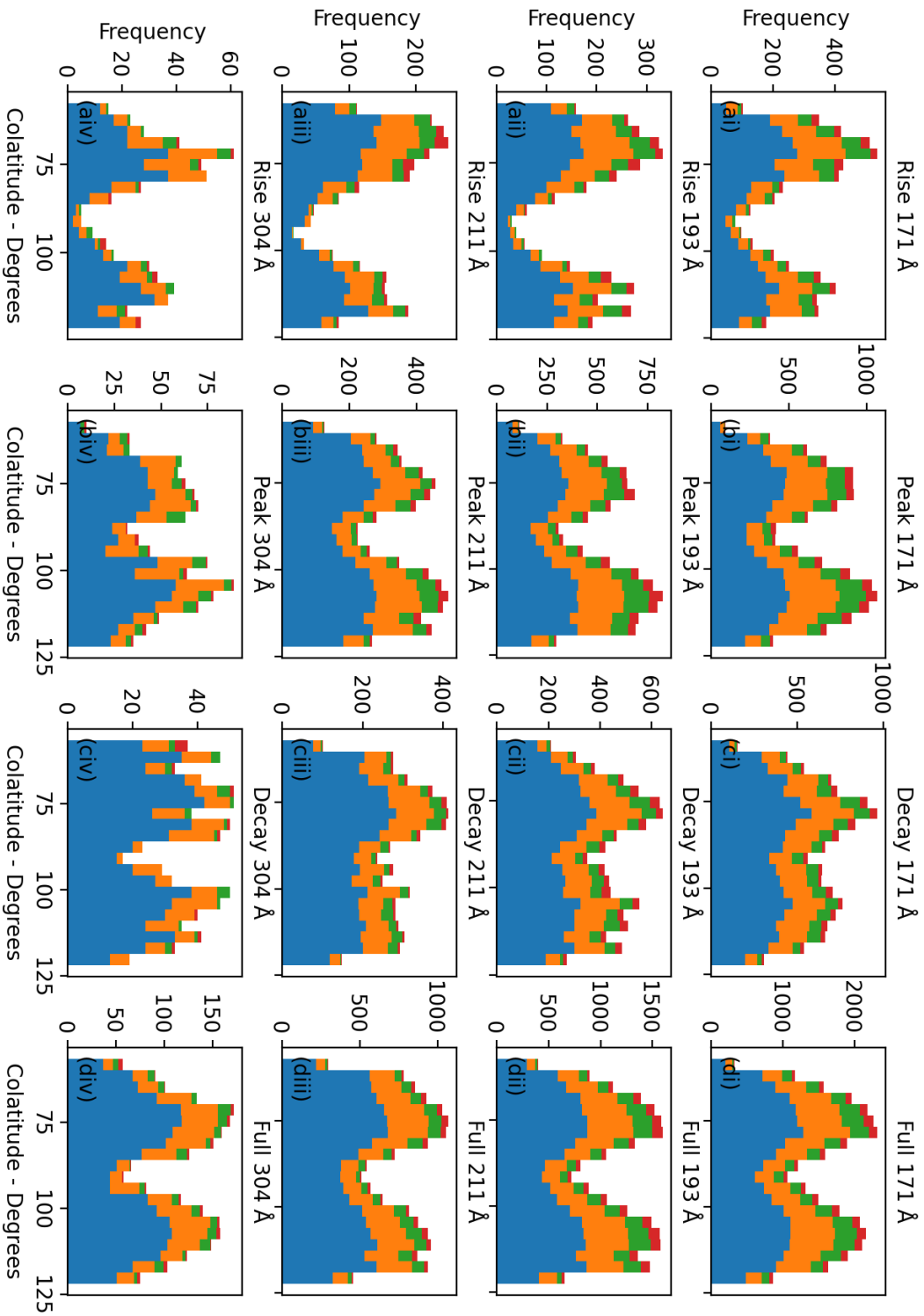

Figure 5.9: Colatitude frequency diagram, frequency (y axis) vs colatitude (x axis) for differing loop populations, with stacked width population (colours) as below. Blue, orange, green, and red represent structures 2-3, 3-4, 4-5, and 5+ pixels wide respectively.

Figure 5.9 visually presents the contribution of various populations of width frequency to the colatitude distributions. In order of smallest to largest; blue represents the 2-3 pixel range, orange represents the 3-4 pixel range, green indicates the 4-5 pixel range, red indicates the 5+ pixel range. Each wavelength and time phase is represented as a distinct population of loop widths(frequency on y axis) and the distribution of their latitudinal positions (degree bins on x axis). The colatitude distributions follow those seen in Figure 5.5, with a greater degree of spatial separation between the loop populations (the distance between the "peaks" of frequency present in the northern and southern half of the diagram) seen in the rise phase, with each subsequent phase displaying less distinction between the two separate hemispheres. Visually, these populations do not appear to drastically change between colatitude s, phases or wavelengths. To further demonstrate this, the fractional proportion of each width subsection by wavelength and time phase has been plotted in Figure 5.10

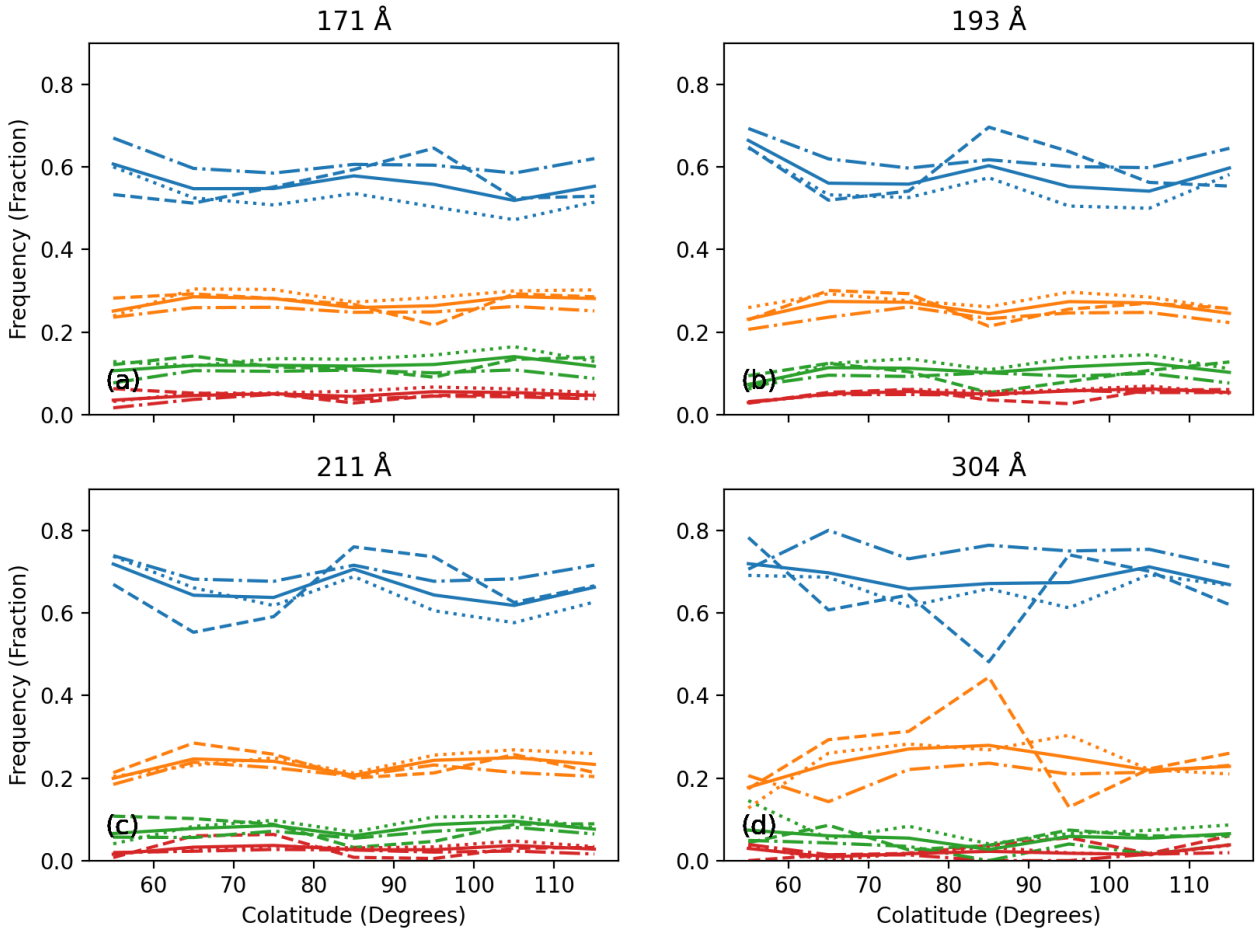

Figure 5.10: Predominance of Widths (Y axis) vs Colatitude (X axis) by various structural widths (colors), with varying phases of solar cycle (dashes). Blue indicates structures between 2-3 pixels, Orange represents structures between 3-4 pixels, green represents structures between 4-5 pixels, and red represents structures above five pixel widths. Dashed lines indicate which time phase the sample is measured across. "–" long dashed lines indicate a rise phase population, ".." dotted lines indicate a peak phase population, "-." dashed dotted lines indicate a decay phase population, and "-" full lines indicate a full cross phase population.

Figure 5.10 displays the frequency of varying width ranges of loop populations

of various time phases vs their latitudinal frequency as a proportion of the total number of loops present in that colatitude . The colatitude corresponds directly to the bins used in Figure 5.9, and each point of the line is based on the frequency of various pixel width subsections recorded within that bin. Each wavelength (171 Å- a, 193 Å- b, 211 Å- c 304 Å- d,) is similarly examined and the results displayed. This can be seen to mirror results of Figure 5.3, as peak and rise phase lines possess slightly lower proportional fractions of the blue and orange lines, indicating that these populations had a greater number of large loops.

These pixel ranges settle into stratified bands of frequency, which are stable throughout the range of colatitude s in wavelengths with sufficiently populated samples. The blue 2-3 pixel range typically occupies a range of 0.55-0.65 in 171 Å, 0.55-0.65 in 193 Å, 0.55-0.7 in 304 Å, and 0.55-0.75 in 211 Å. This range is relatively consistent, and accounts in most cases for 55 to 65 percent of observed loops across all colatitude bins in each wavelength. Of some interest is a slight increase in the frequency of 2 pixel loops between 85 and 90 degrees in colatitude present in most time phases (and a reciprocal decrease in other pixel widths in these same time phases).

The orange 3-4 pixel range is more consistent, occupying a range between 0.25 and 0.3 in 171 Å, 211 Å, and 193 Å, with greater variation in 304 Å; between 0.2 and 0.4. This corresponds to 25-30 percent and 20-40 percent of a population present at each colatitude respectively. The 171 Åorange lines seem to occupy a slightly higher percentage of total loop populations compared to others, despite the overall lower power law slopes of loop populations observed in 193 Åcompared to 171 Å.

The green 4-5 pixel range is similarly consistent to the orange range, with frequencies occurring primarily between 0.07 and 0.13 in most wavelengths, excluding a slightly lower range of lines in 211 Å, indicative of much a higher power law slope and relative lack of wide loop structures. This means that 3-4 pixel wide loops

account for 7 to 13 percent of most loop samples.

The final 5+ red pixel range is constitutes a very small number of any given loop population regardless of colatitude or phase, across any wavelength. Ranges of 4-5 percent are typical of most phases and colatitude s in this width sample, 193 Åslightly higher than 171 Åin this band representative of slightly lower power law slopes in loop width distributions.

5.2.4 Population slopes versus time

The loop width power law slope has been examined as a means of exploring changing coronal activity and the relative abundance of observed loops in the northern and southern hemispheres. By combining analysis of power law slopes in a more granular fashion ie; yearly, as opposed to simply by phase of the solar cycle, a better understanding of how these populations behave can be obtained. Figure 5.11 outlines the results of this study.

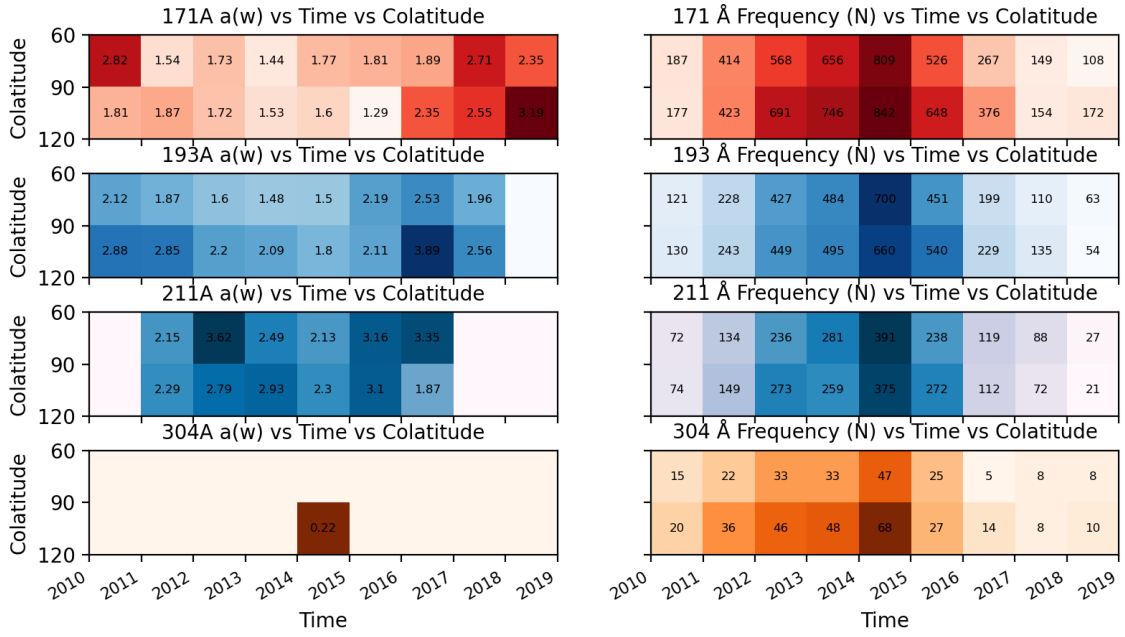

Figure 5.11: Diagram of $\alpha(w)$ for subsections of loop populations between 3 and 5 pixels in the northern and southern hemispheres per year within Solar Cycle 24. Sections with less than 100 total observations (50 for 304 Å) are left blank. Corresponding loop frequency values are shown on the right hand side of the diagram.

Power law slopes are determined for each wavelength for populations in each hemisphere per year within Solar Cycle 24 in the same manner as described in Section 3.1, and displayed in a 2d color histogram plot in north and south hemisphere by year. These values indicate a detectable difference in the underlying distribution of coronal loop widths present at different points in time, though the exact values presented should not be considered as confident as those presented in Figure 5.3. Due to comparatively lower frequencies in each section and colatitude , the exact values are more likely to be prone to issues arising from sub sampling within bins, and is also likely to affect 211 Åand 304 Åmore than 171 Åor 193 Å.

These power law slope values demonstrate a change which is characteristic of the changing solar cycle in both space and magnetic activity. The lowest value

of 1.91 for 171 Åin the northern hemisphere coincides with the phase in which northern activity is at its greatest extent, similarly the lowest value of 2.05 for the southern hemisphere occurs when southern activity peaks, changing in a manner coinciding with the activity displayed in Figure 3.1. This demonstrates that the slopes of each hemisphere closest approach the ideal during phases containing the most observations, and given greater numbers of detections, could detail meaningful alterations to population slopes.

5.3 Discussion

5.3.1 Width Frequency Profiles and slopes

As mentioned in Chapters 2 and 3, the mechanism for DC heating is potentially describable as an SOC process. That is, that the requirements of stochastic addition (energy deposited randomly to subresolved filaments within the footpoints of coronal structures), the existence of a local critical threshold (the amount of energy which is needed to trigger the process of magnetic reconnection), the multi-scale nature of the space (subresolved flux tubes of scale lengths of potentially as few as sub ten km in a space up to 10,000s of km), and the presence of a global critical state by which small scale events can spread and cascade into larger events which spread throughout the space (local magnetic reconnection perturbs adjacent strands and causes further reconnection events to occur throughout the footpoint of a coronal structure) mean that some characteristic statistics of SOC processes might be detectable within large enough samples of these coronal structures. To do this, the impact of observational effects on the resulting statistics should be reduced, to allow for physical effects within the corona to be detected. To minimize the impact of observational effects, and to analyse the effect of changing magnetic activity throughout the solar cycle, slopes can be gathered from populations at various phases of magnetic activity and

compared to each other - as each phase will be analysed with an identical method and instrument. With observational techniques being consistent for all observations made, the primary difference between the power law slopes in different loop populations measured in the phases described above should be descriptive of physical changes within the corona throughout the solar cycle, by means of comparisons of power law slopes.

An example of an observational effect which will ideally be constrained is of smaller, optically thin loops which while distinct physically, will be arranged too closely to be spatially distinguished within the line of sight, and may be misidentified as a larger structure. Though not all of these effects can be removed from a resulting body of statistics, they can be predicted and accounted for when interpreting the final distribution. For example, compounding of small optically thin structures could account for a higher than predicted number of "mid range" loops from 5-7 pixels for example, as the number of identified structures in this range would be inflated by misidentified collections of these smaller structures. Additionally, there are alternative possible physical explanations which could cause deviations from idealized SOC behaviour, such as heating mechanisms, changes to magnetic and plasma pressure across a footpoint region, as well as changes to emerging magnetic flux tubes caused by Alfén waves or other mechanical distortions which may be less conducive to being approximated by SOC statistics. Additionally, phenomena which conform to SOC distributions typically display curtailing effects at higher and low scale lengths. Quenching and finite-scale length effects (see Chapter 2) in particular have the potential to lower the frequency of large scale events by reducing the ability for the system to dissipate energy across the full scale length of the system. In the context of coronal loop populations, effects resembling higher quenching could indicate that regions of emerging flux tubes transfer energy through that space inefficiently, for example.

Interpretations of power law slopes in the following Sections are given with these physical explanations in mind, but it should be noted that these are not direct physical observations of such physical heating mechanisms, and can only be taken as supporting evidence for the predominance of certain mechanisms and interactions during the solar cycle.

As well as coronal widths, the hemispheric asymmetry of structures can indicate the behaviour of the corona and its reaction to the changing activity within the asymmetric solar dynamo. Such examinations would allow for a coronal region to be "mapped" throughout the solar cycle, and examined for trends and distributions which may be characteristic of the solar atmosphere and the magnetic field as it moves into the outer solar atmosphere. Such examination may prove useful for determining the degree of similarity between the placement of coronal structures and their corresponding photospheric footpoints, such as active region sunspots, as well as identifying divergences from these expected positions in different temperature regimes. As the behaviour of magnetic flux tubes and how they change as a consequence of emergence and height above the photosphere is not completely understood (Inoue et al., 2018b), and given the obvious implications these mechanisms have for space weather and the interaction of solar magnetic fields with the outer solar atmosphere, this could represent an alternative way to approach studying the shape and the dynamics of the coronal atmosphere throughout a solar cycle.

Both the lower and higher end discrepancies could be considered as a combination of observational effects described above and physical deviations from the simplified assumptions of an SOC model in conditions within the corona at loop footpoints. As observations are made with the same instrument and experimental techniques, variations observed should be indicative of physical change.

These descriptions of possible physical explanations can explain some specific variations from the ideal distribution at one instant of time or region of the solar

atmosphere, but it cannot be certain that these explanations account for the entirety of any observed change. To avoid this, it is necessary to properly leverage the ability to take measurements at multiple points in time, and correlate quantifiable alterations in the observed slopes. This way, properties of coronal structures as a whole can be measured in a quantifiable way alongside changes in the solar cycle.

The type of study described here is likely to be more difficult in bands with less recorded detections. Structure populations could be more affected by background reduction techniques in some wavelengths than others. 304 Åfor example is a band with broad spectral sensitivity and lower temperature, with less plasma emission intensity at the height of the annulus and may be affected in this way.

The discrepancy of population slopes observed, average power law slopes across the entire Solar Cycle 24 being 1.806 for 171 Å, 2.054 for 193 Å, 2.891 for 211 Å, 3.857 for 304 Å(Section 5.2.1) versus the ideal FD-SOC slope of 1.5 (see Chapter 2) is possibly due to the result of a number of physical and observational effects which curtail the distribution at both high and low widths. If this is the case, it should be seen that these very large slopes are reduced when the slope is fit between a narrower range closer to the center of the right hand side of the distribution. This is demonstrated in Section 5.2. As previously mentioned in Chapter 2, the value of the power law slope α_{w} of the frequency distribution of loop widths $D(w)$ is expected to be analogous to the same power law slope of cascading events α_{s} taking place within the emerging region assuming that principles of SOC apply to the phenomenon of coronal loops. Under ideal FD SOC conditions, the slope of such a distribution would be equal to 1.5. Clearly the results outlined above can differ substantially from this prediction depending on the width ranges viewed, with the lowest observed slope for 171 Å(the most well populated wavelength) equal to 2.81 for 193 ÅRise phase between 3 and 6 pixels, exceeding the predicted value by more than 1.5.

The variation of the slope value between time phases is particularly important

for deeper study of the conditions within loop forming regions. If SOC is taken as a valid descriptor of the consequence of microscopic heating and reconnection events which cause coronal loops to appear, then it is important to understand what the slope measurements are telling us. These variations can be described in roughly two ways; physical variations and observational complications.

Physical variations arise when the physical conditions present in the loop forming regions differ from those assumed by an ideal FD SOC model. Some degree of variation is to be expected as SOC is not a complete analytical model of real world physical behaviour, but the degree to which a distribution varies can be an indicator of how extreme these physical deviations are. Some examples of this type of variation include but are not limited to, (i) limited size scaling effects which curtail the amount of small and large scale phenomenon; (ii) quenching effects limiting the interconnections of the smallest unit scale analogous to the cell size of an SOC automaton model which can limit the number of large events; and (iii) variations of dissipation time scales and the spatial distribution of events which change the critical function or threshold in space. Any of these are potentially significant in describing the exact physical behaviour underpinning the phenomenon being described. In the context of coronal loops, these could indicate a variation in the processes or frequency of heating events, or the level of magnetic activity at their footpoints which could alter the rate of reconnection events.

Observational complications are caused by the inability of observational instruments to properly capture the true distribution of parameters being observed. This arises from a number of issues including but not limited to,(i) the resolution of an instrument and the minimum observable width as described by Equation 1.1 will threshold the power law at small values,(ii) line-of-sight effects are prevalent when viewing structures in the corona, as individual coronal loop structures are difficult

to isolate due to emitting plasma from diffuse background or by other coronal structures in the same line-of-sight. This can negatively affect both scale lengths of the size distribution of loop populations, and result in a larger than expected number of structures between them - but will primarily affect high width populations as these are more vulnerable to small changes in observed frequency.

That the measured power law when fit to a range closer to the center of the distribution is significantly closer to the SOC predicted value of 1.5 ; 1.63 for 171 ÅPeak, 1.80 for 193 ÅPeak, 2.64 for 211 ÅPeak and 3.44 for Å304 Peak indicates that the deviation from SOC is sometimes caused by a small number of loops at the highest widths. Given the size of the distribution, small changes in wide structure numbers can affect power law slope profiles more than thinner structures. It is likely that curtailing or small statistical variation effects are responsible for at least some of the deviation from the predicted value of 1.5. It can be seen from the Hi-C width compilation (Figure13.h from Aschwanden & Peter (2017)) that the differential and cumulative power law of that population are much closer to those seen between 2.7-5 pixels in AIA (around 1.39 for Hi-C versus 1.8 average 171 Åpopulations in this study). This may suggest that once observational thresholding effects introduced by the AIA are reduced, that distributions of loops observed in EUV are much closer to theoretical SOC distributions than suggested by the entire population. This in turn suggests that despite complex physics involved in coronal loop creation, that at least some component of the underlying physical processes adhere to SOC principles.

However, the 2.7 - 5 pixel widths represent a restricted subset of a larger population and care must be taken so as not to make broad assumptions of coronal and photospheric behaviours based solely on these samplings. It cannot be proven at this stage that SOC behaviour is an appropriate approximation for the mechanism describing the formation of observable coronal structures, or if the SOC approximating component is just one of the relevant formation mechanisms. Though this

is evidence in support of the previous assumptions, more work should be done to show that the model is a "close enough" approximation of coronal loop creation, and greater effort is needed to constrain their exact behaviours in relation to SOC models.

When a slope is measured for a coronal loop population in one particular instant and region, the variance of the real slope value $\alpha_{\rm w}$ from the predicted value $\alpha_{\rm s}$ is indicative of a scale of deviations from the ideal model. This by itself can be descriptive of physical processes underlying the observed profile, but cannot be disentangled from observational effects and cannot be used as definitive evidence of a particular kind of physical process being favored in that region.

The advantage of obtaining multiple slope values across various wavelengths from a variety of time phases with identical methodology then is to explore the dataset and ascertain if it is possible to constrain the possible sources of deviation with the distribution that is available. If a deviation is found across a number of time phases, and is found to be consistent throughout multiple wavelengths as is seen in slope distributions described above, and observational effects are therefore controlled for, then it is possible that the degree of variation in these power laws is indicative of a change in physical conditions at the level which is analogous to the unit scale of an SOC model (ie flux tubes).

These variations may help to verify predictions made regarding the role of various heating effects or at the very least that these processes are changing throughout the solar cycle.

5.3.2 Colatitude Profiles and Asymmetries

Results of colatitude distribution of active region coronal structures versus time (Section 5.2.2) indicates an earlier peaking but extended decaying of coronal activity in the north, and a delayed peaking but accelerated decaying of activity in the

south. The highest phase of overall sunspot activity occurs due to southern activity rather than activity in the hemisphere which dominates the cycle as a whole, hence showing that the phenomenon of hemispheric asymmetry is more nuanced than a North vs South predominance per cycle. The solar magnetic field is expected to be north driven in Solar Cycle 24, though some phases of southern leading activity around the peak phase of sunspot counts is observed. 171 Å(Figure 5.4a) bears a close similarity to sunspot figures in this time, but the hemispheric asymmetry is not quite as pronounced. Though the highest monthly average is in the northern hemisphere, the highest individual measurement of loop activity occurs in the southern hemisphere. 193 Å(Figure 5.4b) and 211 Å(Figure5.4c) show a similar, but more muted biphasic solar cycle asymmetry. Southern hemisphere measurements are very important in accounting for coronal activity, and show clearly that NS asymmetry in Solar Cycle 24 is defined by two different overlapping modes of activity in northern and southern hemispheres. A direct comparison of coronal loop frequency in north versus south hemispheres to sunspot figures yields a strong positive correlation between sunspots and coronal structures. This is seen in Figure 5.12, which compares hemispheric sunspot frequencies normalized by the highest absolute value in each series in raw and smoothed (monthly average) distributions with measured coronal structure equivalents. A lag is seen between some individual peaks of coronal loop frequency, but is not consistently before or ahead of corresponding sunspot peaks and might mostly be attributed to the difference in where these statistics are collected (disc versus limb).

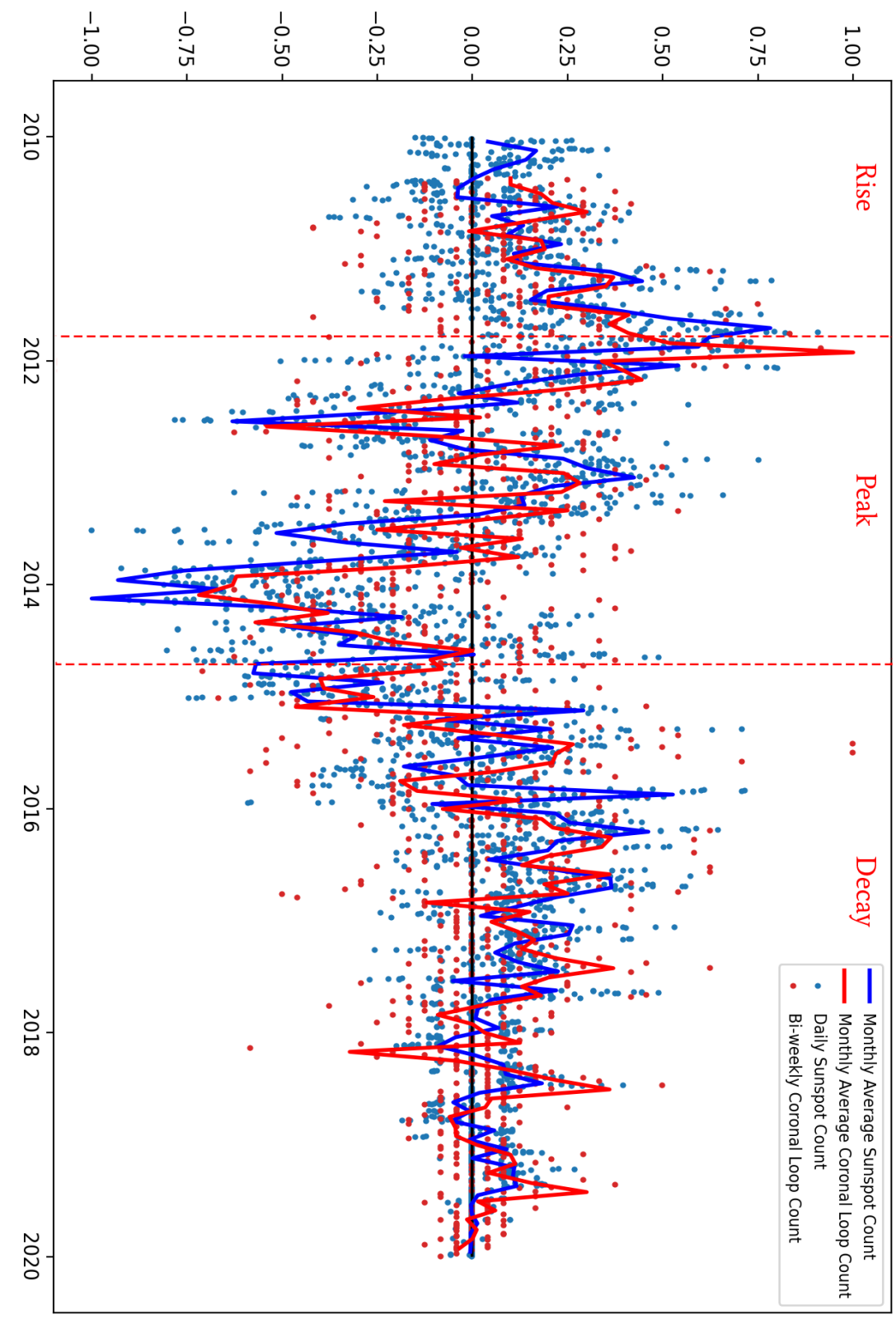

Figure 5.12: A North - South frequency diagram of 171 Åcoronal loops normalized by the largest absolute value in sequence and daily sunspot figures vs time over the 24th solar cycle. Lines indicate the monthly averages for both. Sunspot data from SILSO (SILSO World Data Center, 2010-2020)

A summary of relevant results for N-S loop asymmetry is provided in Table 5.7 and represented in Figure 5.6. It shows that loop asymmetries broadly mirror the same trends seen in sunspot data - though loop asymmetries in general tend to be less pronounced than sunspot data, This is likely due to the fact that coronal loops diverge from sunspots as they spread into the corona, and are also less tightly bound to relations which describe the positions of sunspot occurrence in the solar cycle.

This could suggest that northern loop populations are sustained for longer phases of time, or that southern loop populations peak later in the cycle. This would indicate a difference of some degree in the behaviour of the solar dynamo in the southern hemisphere versus the north for this half of Solar Cycle 24. 171 Åasymmetry data shows more variability than asymmetries in other wavelengths, particularly apparent in the late northern rise phase. This more closely mirrors overall sunspot counts than other wavelength populations, possibly as a consequence of having more coronal loop data than other wavelengths.

Following analyses of both coronal structural frequencies within the active region (see Figure 5.4) and solar sunspot frequency (see Figure 3.1), it can be seen that the overall hemispheric activity for both sunspots and coronal structures is nuanced, with a two distinct phases of activity occurring in each hemisphere. This trend continues within coronal structural populations, and can be seen in all wavelengths. This indicates some underlying commonalities between structure populations within different wavelength and temperature regimes, indicating that despite being composed of different loop populations, the underlying conditions required to produce these loops compared to other wavelength populations are present in the same active regions. Alternatively, some of these structures may be multithermal, composed of plasma of varying temperatures and visible in several EUV channels which may change in composition. It is possible that more multithermal structures may appear in periods of high magnetic activity, causing frequencies to vary dependant on the

phase of the solar cycle, for example.

5.3.3 Other Variables and Analysis

5.3.3.1 Width Power Law by Hemisphere vs Time

The results presented in previous sections highlight the changes to the frequency and observed power law slope of structures present within each hemisphere within a given year from the start to the end of the solar cycle (Figure5.11). This analysis combines aspects of both the coronal structural width data by means of measuring and comparing power laws and of asymmetry analysis by means of comparing the frequency of structures seen at varying points of the solar cycle.

From the change in slopes (shallower overall slope in phases of high activity), it can be seen that the changes in slope follow the change in magnetic activity in Solar Cycle 24, and that these values may be indicative of the nature and magnitude of change present within the regions that produce coronal structure. These slopes show a distinct pattern of rise coinciding with peaks in 2012 (-1.91 in northern hemisphere for 171 Å) and 2014 when activity peaks in the south, (-1.96 and -2.05 for 171 Åin north and south hemispheres respectively) followed by decline which varies by wavelength, but a noticeable rise immediately following a point of decay in the northern colatitude . More coronal loops are required for more definitive assessments of coronal behaviour on a timescale and colatitude scales of individual hemispheres and years, but targeted examination of on disc active regions at various points in the solar cycle might aid in expanding upon this analysis.

5.3.3.2 Average Structure Intensity Frequency

The average intensity of the coronal structures measured was compiled as part of the structural identification measurement process as described in the method Chapter 3. These intensities are recorded as part of a statistical test, as simultaneous detection

of intensity of structures in varying wavelengths was not recorded. The results of this analysis are displayed in Figure 5.13.

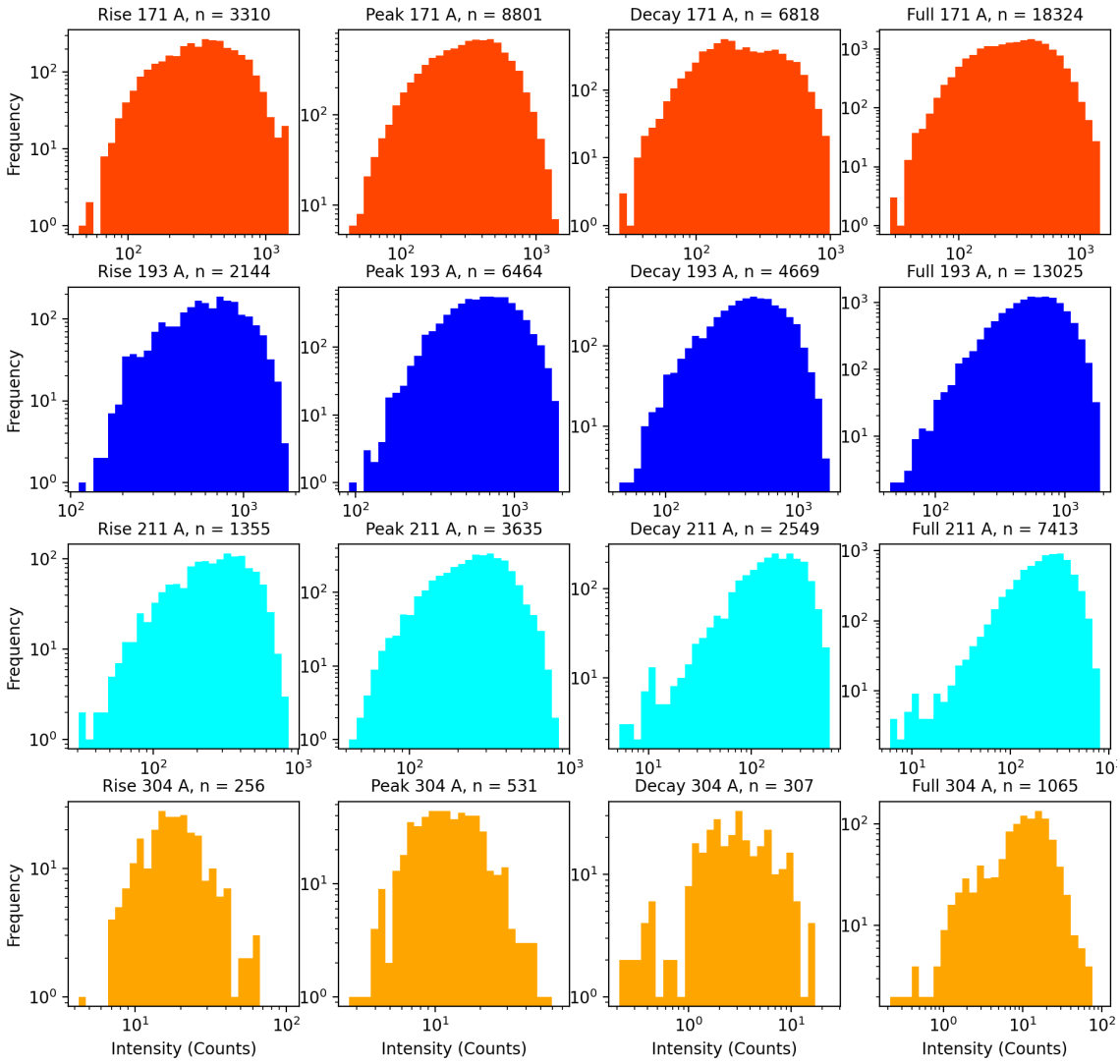

Figure 5.13: A diagram displaying the average structural intensities between 2.7 and 5 pixels wide (x axis) versus the recorded frequency of the measured intensity (y axis) for the three recorded phases of the solar cycle in varying wavelength (in descending order by row, 171 Å, 193 Å, 211 Å, 304 Å). Both axes are log scaled.

These results indicate a profile of intensity which demonstrates a distribution skewed towards the left, with a peak occurring at roughly 400-500 counts for 171 Å, 500-600 counts for 193 Å, around 200 counts for 211 and 304 Å(the latter being underpopulated and therefore a less confident measurement), consistent across time

phases (304 Åbeing less so due to aforementioned population issues). This appears to indicate a characteristic distribution of intensity measurements for recorded structures, which is a skewed normal distribution with a long "tail" of lower intensity. This may be due to observational effects of detections of "near misses" of structures, and may be an artifact introduced by the fitting process rather than a physical description of structural intensities, or it could be that there are proportionally more dimmer structures due to lesser energy requirements.

5.3.4 Statistical Tests and Confirmations

5.3.4.1 Correlation of Width and Colatitude

Overall, despite some small variance in structure width across colatitude and time phase, analysis of colatitude vs width indicates that it is a poor indicator of the width of a loop at any time phase (as seen in Figure 5.10). This indicates a general similarity in the populations of coronal structures imaged in this region regardless of their viewed colatitude , and that footpoints at each colatitude is equally as likely to produce loops of any coronal width as other colatitude s. This could indicate that changes in observed structural width and the required conditions for forming larger loop structures may not vary by colatitude as much as by time phase. A plot of structure width versus colatitude has been made in Figure 5.14.

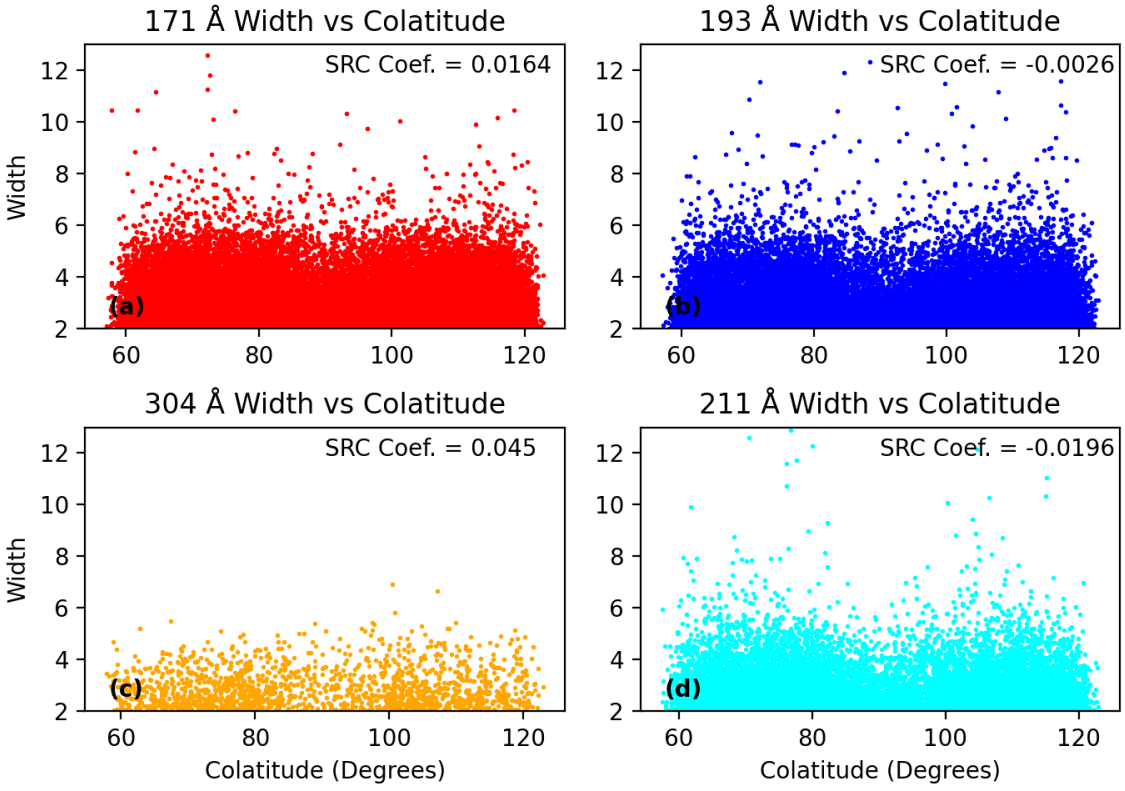

Figure 5.14: Width (y axis) vs Colatitude (x axis) for all loops in population above 2 pixel widths. 171 Å(a), 193 Å(b), 304 Å(c), 211 Å(d)

To quantify this apparent lack of correlation, a Spearman rank correlation coefficient (described in Equation 5.2) determined for the width vs colatitude of each loop in the range of 2-12 pixel widths for each wavelength.

$$R_s = 1 - \frac{6\sum d_i^2}{n(n^2-1)}) \tag{5.2}$$

Here, R_s is the correlation coefficient, n is the number of total observations, $\sum d_i$ is the sum of the difference in ranks of each observed loop in width and colatitude. The values of R_s indicate a very low likelihood of any correlation between loop width and position, approaching a perfect lack of correlation to within 0.05 and a large sample size. At the present time, there is no evidence to suggest any relationship

Table 5.8: Table demonstrating Spearman Rank Correlation Coefficient results for loop width vs colatitude for each wavelength, showing the R_s value, p value, and n number

Wavelength (Å)	R_s	p	n
171	0.0164	0.0063	27847
193	-0.0026	0.7248	19017
211	-0.0196	0.0378	11186
304	0.0450	0.07504	1567

between observed structure width at the limb and colatitude of occurrence.

The value p is the standard p-value test based on the Student t-distribution. Low values of p increases the confidence that the observed lack of correlation is not a coincidence of the data set. The high value of p in the 193 Ådistribution does not necessarily indicate that the correlation is likely to be caused by an improbable distribution, given the large sample size n and the time taken to observe them. It is therefore unlikely that any correlation might be established between width and colatitude based on the information gathered in this dataset in any wavelength. A high p value for a low correlation relation does not mean that a correlation or anti correlation is more likely, simply that it is more likely that this specific distribution could be reproduced by a random uncorrelated set of variables.

5.3.4.2 Cross Correlation of Sunspots vs Coronal Structures

Given the intrinsic link between coronal loops and sunspots, it should be expected that coronal loop frequency is strongly correlated to sunspot frequency, this relationship is examined in Figure 5.12 To examine and confirm this link, the daily hemispheric north - south sunspot count and the average monthly north - south (mean daily) sunspot count obtained from the Royal Belgian Observatory SILSO is

normalized and compared to the bi-weekly (owing to the 3 day time interval) average north - south coronal loop count in 171 and the monthly average north - south coronal loop count in 171 Å. 171 Åis chosen primarily due to the large sample size providing a more representative distribution for comparison, and the similarity to colatitude distributions produced by other wavelengths in this research. To quantify the comparison between the monthly averages of coronal loops and sunspots, a cross correlation was calculated between the overlapping date ranges (1st July 2010 to 30th December 2019), with the standard cross correlation formula;

$$C_{ab}(\tau) = \sum_{i=1}^{n} a(n+\tau) * \overline{b(n)} \tag{5.3}$$

where C_{ab} is the cross correlation of the functions a and b, with time delay τ. $\overline{b(n)}$ is the complex conjugate of the function $b(n)$. The results of this cross correlation are displayed in Figure 5.15. In this case, a is the function of normalized north minus south sunspot frequencies, and b is the function of normalised north minus south loop frequencies for 171 Åpopulations.

This cross correlation is optimal at the 114th displacement value, compared to series length of 116, indicating that the optimal value for correlation is when the two series are almost perfectly aligned. Therefore, the series of monthly average hemispheric sunspot counts and coronal loop counts are best aligned without any delay. This is despite some apparent lags seen between spikes of normalized frequency in either series; the lags are either before or after corresponding spikes in sunspot count. The cause of this delay might be due to the difference in methodology in how these variables are measured, namely that coronal loop widths measured in this study are imaged at the limb, whilst sunspots are measured on the disc.

Average sunspot counts are compiled from daily sunspot figures collected from white light observations of the solar disc, whereas coronal loop measurements are made using EUV observations on the solar limb. As sunspots emerge upon the disc, and any coronal loops corresponding are seen in the coronal limb, these loops can only be observed if they are roughly perpendicular to the line-of-sight. If loops are observed on the eastern limb, then they would appear before any sunspots are observed upon the disc and vice versa if they appear on the western limb. The exact phase of delay is variable, owing to the differential rotational phase of the photosphere, which increases towards the poles but would be expected to occur on either side with approximately the same frequency, despite some variability between observed activity in sunspots and coronal loops, the overall activity should be simultaneous as is demonstrated by the cross correlation plot. Therefore, some loops may be measured slightly behind the limb, and others slightly in front of it. These structures could correspond to sunspots which cannot be counted, as they may either disappear before they move into the disc, or form shortly after they would have appeared. Whether this causes any significant discrepancy between sunspot asymmetry and coronal loop asymmetry is not clear.

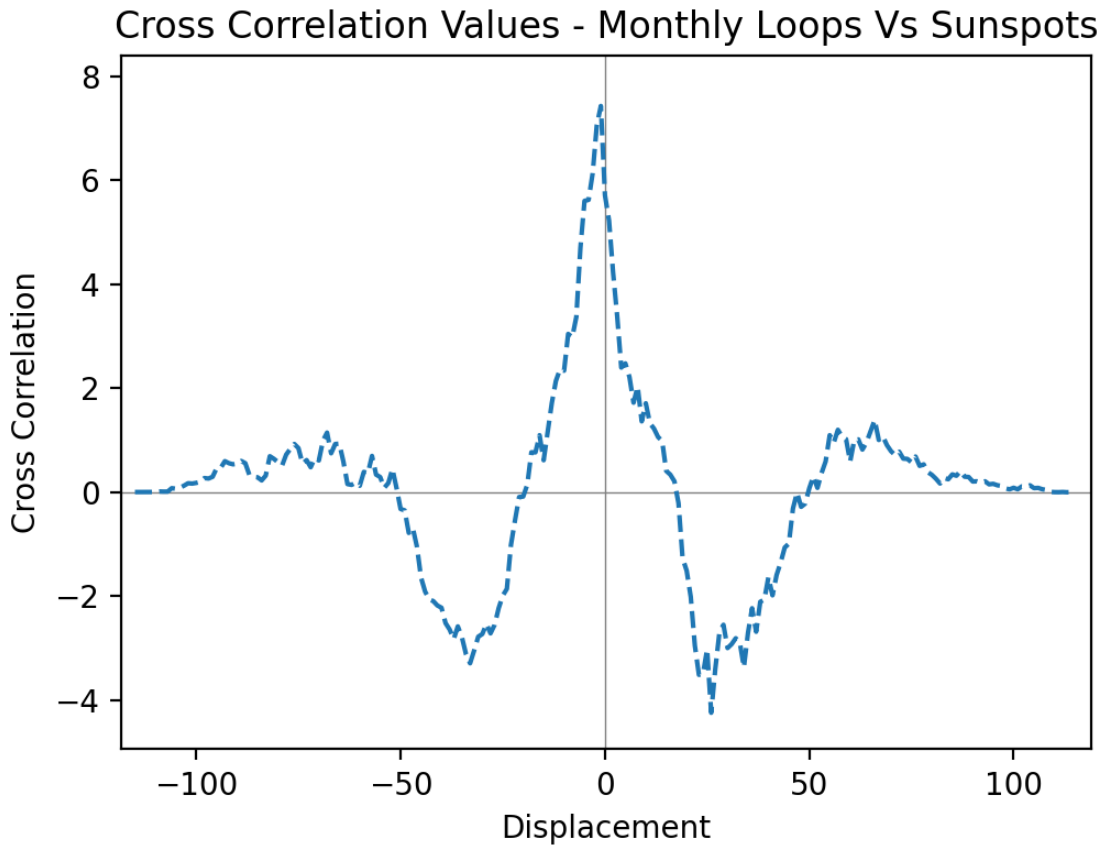

Figure 5.15: The cross correlation of monthly average hemispheric sunspot count difference and coronal loop hemispheric frequency difference. The peak value of the cross correlation occurs at position 114, corresponding to the length of the shortest sequence.

5.3.4.3 Intensity vs Width

The relationship between the intensity and width of coronal structures is not expected to be related Klimchuk & Deforest (2020). To examine whether the width and intensity of structures in this distribution are also unrelated, and width relation of each recorded plume in the extended 2 - 12 pixel range is demonstrated in Figure 5.16. In this figure, structures are shown to show a very slight correlation of width and brightness little in intensity by wavelength, the black dashed line indicating the average intensity of plumes within a 0.25 range of the black dot. These lines remain consistently flat, and a Spearman Rank Correlation performed on these populations indicated R_s values of 0.12, 0.15, 0.22, and 0.13 for 171, 193, 211, and 304 Årespectively. Each population possessed a p value of below 0.001. These results indicate that a correlation in the observational coronal active region structures is small, but not statistically insignificant, but this is likely due to the observational bias against wider, dimmer structures in the brighter equatorial active region limb where these structures are most likely to be affected by local background subtraction. This would negatively affect the number of these structures that exist in the observational population, skewing the distribution towards brighter structures in the wide width ranges.

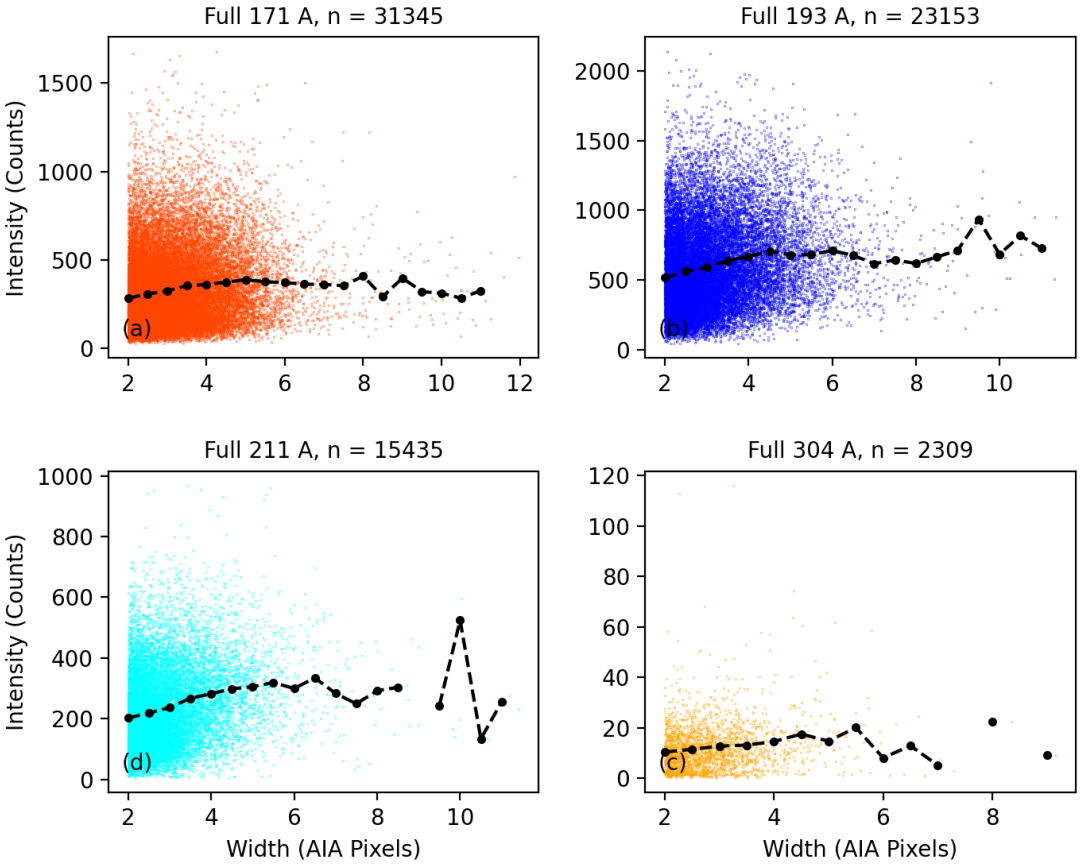

Figure 5.16: The intensity (y axis) vs width (x axis) of equatorial active region structures recorded in the 2-12 pixel width range. Black dashed line is the average intensity of plumes within a 0.25 pixel width range within 171 (a), 193 (b), 211 (c), and 304 (d) Åfor all time phases.

5.4 Summary

The coronal structures described in this work represent different regimes of coronal plasma populations, at differing temperatures and altitudes. It was anticipated that investigating changes in coronal loop widths and colatitude s across Solar Cycle

24 would allow for more detailed insight into SOC slopes and asymmetry of the corona over time, and that trends might be identified which had previously escaped detection due to a lack of extended analysis across the solar cycle. This was achieved by means of a comprehensive analysis of coronal loops in Solar Cycle 24, using the 171, 193, 211, and 304 Åfilters of SDO's AIA instrument.

Loops were isolated by constraining the limb at a fixed height, with loop segments traced automatically across the constrained annulus at a rate of one image per three days and Gaussian profiles fit to cross sectional intensity values. From these profile measurements, over 50,000 loops were measured in all wavelengths above 2.7 pixel widths; the limit of confident width detection imposed by instrumental constraints.

From these loops, analysis of width, colatitude , and flux was performed. Coronal loop widths were analysed by compiling the width of all loops above two pixels separated into wavelengths and subsequent populations in the rise, peak, and decay phase (as well as an aggregated full time phase for comparison). The power law slope of the produced distribution was compared to both theoretical SOC distributions (1.5 for FD SOC) and those measured by other studies of on-limb coronal loops measured in 193 Å(2.7 - 3.1 for Zhiming et al. (2019), Aschwanden & Peter (2017)). These distributions were found to vary across the solar cycle, increasing in magnitude throughout these distinct phases; 1.6 ± 0.091, 1.63 ± 0.065, and 2.063 ± 0.11 for rise, peak, and decay in 171 Åfor example. This trend indicates that observed coronal loop structures appeared to be narrower over time, with less wide structures and more narrow structures present within width distributions. This trend was mirrored across multiple wavelengths, but 171 populations were generally steeper than 193, and 211 were significantly steeper than both 171 and 193 Å. 304 Åpopulations were much less well populated than other wavelengths, and it was difficult to analyse the slope of their power law slopes. This analysis has revealed two things; that coronal loop width power law distributions change throughout the solar cycle, indicating a

change to the rate of non-linear dissipative events thought to produce coronal loops at their footpoints in the photosphere, and that these differences are quantifiable and consistent between wavelengths. More detailed examination of loop populations present in existing and future datasets will be of use in understanding how the corona and its magnetic framework changes and can change over time.

More work regarding the exact change of SOC parameters and how they relate to heating mechanisms within/without active regions and phases of the solar cycle may be useful as a probe of exact heating mechanisms and thresholds. Similarly to coronal widths, coronal loop colatitude s were recorded and compiled. These colatitude s were similarly divided into rise, peak, decay populations and the distributions examined. (See Figure 5.5) These distributions revealed asymmetries in coronal loop populations in north and south hemispheres which varied throughout the solar cycle, but which remained relatively consistent between wavelengths; Northern loop fraction of 0.5 for 171 Å , 0.49 for 193 Å, and 0.54 for 211 Å, 0.521 for 304 Å. While these fractions are similar across each wavelength, there is significant variation within the solar cycle, with phases of southern lead activity reaching as high as 60 percent in 171 Å.

Following this, analysis of the relation between coronal loop width and position was performed within each of the phases of study mentioned previously. The purpose of this analysis was to examine the relation between coronal activity and colatitude . Analysis of the asymmetry indices of coronal structures and sunspots indicated that loops broadly followed trends of sunspot asymmetry, but to a lesser extent. A butterfly diagram of coronal structure frequency similarly shows a broad similarity to a sunspot butterfly diagram. Loop colatitude s and their widths are compiled in Figure 5.9. The relative frequency of each of these bins is plotted for each wavelength and phase in Figure 5.10, indicating generally a lack of connection between colatitude and width. This is confirmed statistically by means of a test of

correlation coefficient of width and colatitude for each loop recorded above 2 pixels. The results (Figure 5.14 and table 5.8) show an R_s value magnitude of less than 0.05 for every wavelength. This indicates that no meaningful relation can be determined between loop colatitude and width independent of time phase, and that the conditions at each colatitude do not vary substantially with regards to coronal loop formation.

Coronal loop asymmetry indexes (Figure5.6, Table 5.7) are constructed to compare coronal loop NS-asymmetry with sunspots figures. This is the first study to highlight and quantify the differences in coronal loop activity in each hemisphere, and across various EUV channels across an entire Solar Cycle, which is made possible due to the large number coronal loop measurements across a decade as part of the SDO's ongoing mission. Loop hemispheric activity is also compared to sunspot hemispheric activity (Figure5.12) in 171 Å, indicating a close link between normalized sunspot and coronal loop activity. The colatitude distribution of coronal loops vs time (Figure5.8) is similar to equivalent measures of sunspot activity, such as the total solar disc coverage by colatitude butterfly diagram (Figure5.7).

Chapter 6

Polar Plumes

In this chapter, the techniques outlined in Chapters 3 and 4 relating to the extraction of positional and width information from coronal structures are applied to structures found within the polar open regions. These correspond to coronal plumes distributed around the open coronal holes, the occurrence of which depends on the phase of the solar cycle, with minimum periods resulting in more plumes, and maximum periods resulting in less plumes. An introduction summarizing the physical phenomena of coronal plumes and the results and analysis of the widths and hemispheric abundance of these plumes are outlined in the following chapter. Code and Results provided. [1]

6.0.1 Plume Classification / Morphology

Coronal plumes are extended ray-like structures, typically present in the north and south coronal polar regions, attached to or located closely to coronal holes (Poletto, 2015). Coronal holes are regions of open magnetic flux from which the fast solar wind originates (Bravo & Stewart, 1997; Cranmer & Winebarger, 2019) and are present throughout all phases of the solar cycle to greater or lesser extents at varying latitudes. Largely devoid of features associated with active regions (coronal moss,

[1] `https://github.com/DanGass/ThesisCode`

coronal loops, flares), their size and intensity are related to the solar cycle depending on the strength of the poloidal component of the magnetic field, as described by the Babcock-Leighton dynamo model developed in the 1960s (Babcock, 1961; Leighton, 1969). The poloidal field describes the component of the magnetic field which is aligned with the polar axis, as opposed to the toroidal field, which is aligned along the equator. The poloidal component interacts with the magnetic fields of the polar dipoles, reducing the extent of the open field region, and consequently, the observed coverage of the coronal holes. The intensity of this poloidal field is at its greatest during periods of solar maximum, therefore polar hole coverage is smallest during this period. Inversely, when at solar minimum, the poloidal field is weakened, reducing the interaction with the dipole field and maximising the area of the coronal hole. From this, it is expected that the highest number of structures will appear at solar minimum, and will be anti correlated with the hemisphere of highest activity. This can be seen in a diagram of normalized N-S plume activity versus sunspot activity seen in Figure 6.1. Sunspot data has been acquired from the SILSO database.

Streamers and other magnetically open and elongated polar structures were one of the early coronal structures identified by ground based observers by using coronagraphs, as the elongated arcs that form them are readily visible in white light observations of the solar atmosphere during solar eclipses, with streamers often extending out to several solar radii above the limb (de Ferrer, 1809). As techniques and instruments for examining the corona have developed, these observations have been bolstered by EUV and X-Ray measurements, first made by space based instruments such as the as the Ulysses mission (Bame et al., 1992) and Skylab (Del Zanna, Bromage & Mason, 2003), but since improving with additions such as SOHO's EIT and SDO's AIA and the upcoming data releases from Solar Orbiter's EUI. These and other instruments have allowed for detailed and multifaceted examinations of plumes and the inter-plume medium in multiple wavelengths, providing estimates

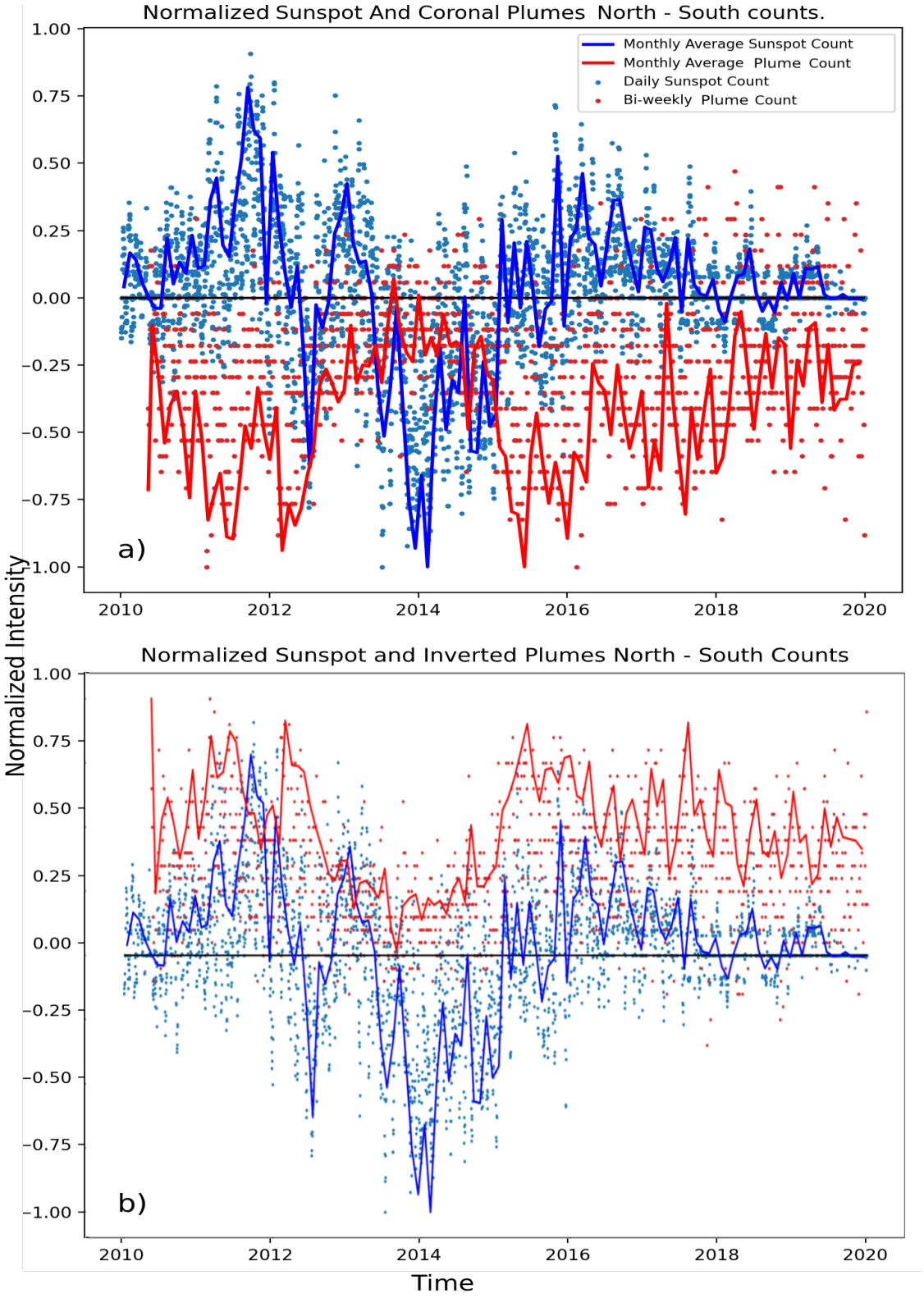

Figure 6.1: Plots of normalized north - south plume frequency (y axis) versus time (x axis) for both sunspots and coronal plumes (a) and inverted image coronal plumes (b) in 171 Å. Sunspot data from SILSO.

of electron temperatures between 0.62 and 2.2 MK, densities between 0.6 and 0.7 $\times 10^8$ cm^{-3} (Mercier & Chambe, 2015, 2016), as well as solar wind speed velocities between 400 - 450 km s^{-1} (McComas et al., 2013). These statistics have been important in determining their relevance to solar wind speeds around the corona and the relative contribution of coronal plumes and coronal holes to the behaviour of space weather (Borovsky & Denton, 2006).

Though similar in that they are prominent "stem" like structures which protrude from the surface of the corona, they differ from coronal loops in several important regards. Firstly, they do not exhibit the same degree of complex "twisting" or braiding effects that appear present in coronal loops (Wang et al., 2022), and they expand far more readily than coronal loops as they rise from the surface of the sun, becoming radial in direction (Boe, Habbal & Druckmuller, 2020).

Secondly, they are connected to the phenomenon of coronal bright points, which are small points on the corona which become bright in EUV and X-Ray wavelengths due to localised reconnection events (Madjarska, 2019). It is thought that bright points are necessary for the formation of plumes, connected to a more intricate network of magnetic structure at and below the photospheric layer (Morgan & Korsós, 2022), though they can persist for some time after their disappearance, which is caused by a drop in density within the plume rather than a drop in temperature. They possess a lifespan on the order of several hours to two days in extreme cases (Pucci et al., 2014), which is similar to closed structures within the active regions.

There has been some debate as to whether plumes or interplume regions are greater contributors to solar wind speeds. Some such as Wilhelm et al. (2011) argue that plumes represent plasma which is relatively static, and exhibits vertical standing oscillations which can be mistaken for outflows while interplume regions (the majority of a coronal hole by area coverage) are by comparison regions of open magnetic flux and outflowing plasma, therefore greater contributors to material

escaping the immediate solar atmosphere and into the interplanetary medium.

Others such as Fu et al. (2014) argue that the plumes contribute to fast solar winds, and do not represent static plasma oscillations, evidenced by differential emission measures of plasma electron temperatures and doppler measurements of plasma in motion. The electron temperature remains constant whilst intensity and densities are reduced throughout the lifespan of coronal plumes, which implies that plume death is caused by material leaving the corona into the interplanetary space, and not by cooling which would result in plasma temperature dropping and material falling back to the surface.

They are also visible to a much further distance than coronal loops, up to several solar radii away from the limb. This is an important difference to coronal loops which do not generally contribute to large scale mass transfers of plasma to the solar atmosphere. Because plumes do not reconnect locally, the material which escapes the plume is carried upwards into the outer solar atmosphere.

As coronal loops can be studied for widths and distributions to analyse their relationship with solar magnetic activity, so can plumes.

6.0.1.1 Questions to Answer

Do plumes display the same kind of power law width distribution as coronal loops?

Plumes are expected to be formed by reconnection events (Wang, Warren & Muglach, 2016), possibly similarly to how coronal loops are formed, and so there may be an expectation of SOC like profiles for their widths. However, differences exist in the conditions around their footpoints and expectations in how these structures are created. In turbulent regions, photospheric motions can drive reconnection, in comparison to closed loops, which experience rapid magnetic reconnection as part of DC heating. This may be caused by the comparatively stable surroundings for

plumes as compared to loops causing different magnetic driving mechanisms leading to the process of magnetic reconnection. Additionally, loops are seem in magnetically closed regions whilst plumes are seen in magnetically open regions as a consequence of the local magnetic field. Any difference in the power law of observable widths for plume populations could indicate a difference in the total amount of reconnection and heating which dominates in the polar regions and the spatial scales over which they operate.

Do plume populations show the same degree of asymmetry between north and south hemispheres as the solar cycle progresses?

Asymmetry has been taken as a measure of relative activity in each hemisphere. Previously in Chapter 5 of this thesis has looked at both the sum difference of northern and southern activity in terms of sunspots and coronal loops, as well as the totals for each hemisphere individually. This hemispheric "imbalance" has highlighted that the solar cycle is not simply a period of one hemisphere growing more dominant, but of distinct and sustained differences in solar activity throughout the solar cycle in each hemisphere. By examining plume asymmetries, the polar corona can also be examined for these differences, providing a potential survey of activity across all latitudes.

Do plumes show the same degree of similarity between wavelengths as seen in coronal loops.

Coronal loops have shown similar trends in spatial distribution and for the relation between width slopes in each phase, indicating that different temperature regimes occupy the same latitudes within active regions. Examining distributions by wavelength in the polar region would allow for closer examination of whether this region is also multithermal by latitude, or whether a latitudinal stratification of temperatures exists in the polar region.

By addressing each of these questions, it may be possible to more closely scrutinise the relationship between coronal plumes and the progression of solar activity throughout the solar cycle. The overall aim is to better the body of observational statistics available for analysis, in turn improving understanding of how the solar magnetic field evolves throughout the solar atmosphere.

6.1 Methodology

To identify and characterise coronal plumes, a similar method to that discussed in Chapter 4 was employed, with some differences to the stem fitting procedure (see figs 4.1 and 1). Instead of implementing curvilinear tracks of circular segments, plumes are approximate enough to straight lines within the range of the annulus that simpler linear segments are employed instead. This was done to improve code performance, given that plumes do not generally display highly curved geometries at low altitudes, hence the resulting and plume cross section measurements should not be affected.

Previously a three day cadence was initially determined by loop lifetimes and visual geometries relating to the limb region and the differential rotation, however the difference in geometry in the polar limb requires consideration. Instead of relying upon differential rotation to clear the line-of-sight, the lifetime of plumes becomes important for avoidance of double counting of structures. As the average lifetime of a plume is estimated to be of the order of hours (Pucci et al., 2014; DeForest, Lamy & Llebaria, 2001), 72 hours will be more than sufficient to ensure the uniqueness of each recorded plume in the resulting dataset.

6.1.1 Fitting Plumes

To identify a plume, an annulus is first fit to the limb between 1.05 and 1.10 solar radii, similar to that described in Chapters 3 and 4 (Method and Algorithm Details). Identification of a plume starts with selecting bright points within close proximity to the innermost annulus (typically 3 pixels). These bright points form the basis for further tracing attempts, performed recursively until the brightest point remaining in the annulus is equal to a value equal to 0.4 the maximum value as outlined in Chapter 4 (see Figure 4.2). This value is chosen as it represents the peak of the Poissonian-like distribution of pixel intensity of the inner annulus.

Once the pixel has been identified, tracing for optimal geometric fitting starts with a line segment rotated through a fixed range as described in Chapter 4, but with modifications as mentioned in the following.

The fitting process has been simplified for use in the polar regions, which typically contain less complex geometries for coronal structures. The curvilinear section fitting process was reworked to fit linear sections directly from one side of the annulus to the other. The optimal angle of the line segment is still determined by iteration (all angles between $\pm$ 20 degrees at base of starting section), and the section is still traced per pixel to determine that the structure is close to continuous.

Like in the previously mentioned study of coronal loops, the eight cross sections are placed equidistantly along the traced bath of the plume. The sum of these cross sections is mean averaged, and local minima background subtraction undertaken to identify the likely profile of the recorded structure. A Gaussian profile is then fit to the composite plume cross section and its width recorded. Examples of plumes fitted within an annulus is provided in Figure 6.2.

In each wavelength, the position of the detected plume is recorded to examine the possibility that plasma regimes are not equally distributed in the polar regions. In this work, previous examinations of frequency versus colatitude (Chapter 5, Figure

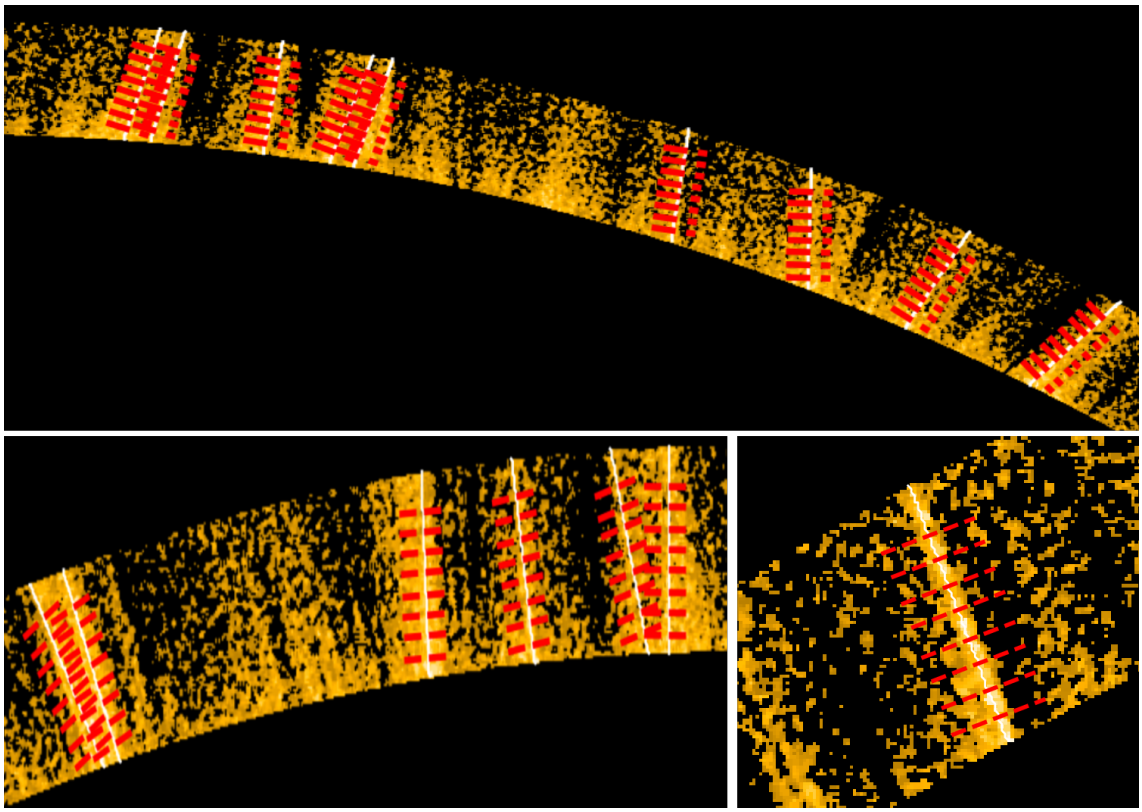

Figure 6.2: Example of plume geometries fitted across the annulus within the polar regions.

.

5.10) for active regions demonstrated a generally mixed spatial distribution, in that loop colatitude distributions did not vary between wavelengths. If this were not the case for plumes, it could demonstrate differences in the fundamental structure of the magnetically open polar regions and magnetically closed and more complex active region loops.

6.1.2 Asymmetry

Of additional interest is any observed north-south hemispheric asymmetry of coronal structures within the polar regions. Frequency and colatitude of plumes is measured, and a map of activity by region can be made. By taking many of these maps across the solar cycle, an understanding of how the polar corona changes across the ten year period of Cycle 24 can be made and compared to sunspot figures and active region structure populations.

This can be examined by recording the colatitude for each structure once it is successfully traced and compiling these into a histogram for each hemisphere. The profile of these histograms indicates the relative frequency and spatial distribution of plume structures within a given span of time. By examining and comparing these profiles to those seen in active regions, the corona in the closed polar region can be examined for structure and any variation of these structures by wavelength and colatitude can also be identified. Colatitude comparisons between hemispheres could potentially indicate the role that varying coronal hole topology and evolution could have on the corona within the open polar region. The extent of asymmetry compared to structures within the equatorial active regions may also highlight the degree to which the polar corona is impacted by the solar activity cycle. The method for examining these asymmetries will be consistent with those outlined in Chapter 5 and will involve constructing histograms for both corrected and uncorrected colatitude displacement from the north pole.

In the next section, the results of analysis of data extracted in these polar regions will be organized into widths and latitudes, and comparisons to results of the previous section regarding "closed" active regions made.

6.2 Results

As can be seen in Table 6.1, the total number of plumes in the 2 - 10 pixel range (the full physical range) observed across the entire solar cycle was 6662 in 171 Å, 3594 in 193 Å, 1147 in 211 Å, and 188 in 304 Å. The number of plumes observed in this period between 2.7 and 5 (confident non-thresholded range) pixels is equal to 3414 in 171 Å, 1703 in 193 Å, 499 in 211 Å, and 130 in 304 Å. This represents a total number of plumes detected as equal to 5746. This is less than the total number of coronal loops seen across the solar cycle in this same pixel range, 23876 (see Table 5.3), by roughly a factor of five in terms of total number.

Table 6.1: Plume structure frequency by wavelength and period. Plume widths between 2 and 10 pixels.

Wavelength (Å)	Rise	Peak	Decay	Total
171	1083	1177	4400	6662
193	638	1480	1474	3594
211	225	427	495	1147
304	48	104	36	188

Table 6.2: Plume structure frequency by wavelength and period. Plume widths between 2.7 and 5 pixels.

Wavelength (Å)	Rise	Peak	Decay	Total
171	518	572	2091	3182
193	276	647	667	1591
211	92	179	201	472
304	30	61	20	111

Table 6.3: Plume frequency by wavelength and hemisphere. Plume widths from 2.7 to 5 pixels.

Wavelength (Å)	North	South	Total
171	1360	2380	3740
193	492	1216	1708
211	181	380	561
304	66	47	113

As can be seen in Figure 6.3, the wider plume widths are closer to the ideal slope than loop widths in the closed active region (see Figure 5.3), meaning that thresholding effects which cause deviation from the ideal SOC distribution are less pronounced at higher widths in plume populations than those seen in active region loops. The range from six to ten pixel widths represents the largest structures that can be regularly detected given distributions numbering in thousands of detections, but their presence in higher abundance in the polar plume populations (see Figure 6.3) could point towards two possibilities. Firstly, the limb background at the polar regions is maybe quieter or less intense than the active region limb background which may reduce the curtailing of wider structures due to background subtraction. Secondly, wider structures may be more prevalent in the open polar regions than

the closed active regions due to physical differences in structure formation.

Although both plumes and loops exhibit power law behaviours in their observable widths, the profiles seen in plume populations appear to differ substantially in terms of slope (3.125 ± 0.093 average slope for plume populations vs 1.806 ± 0.064 in loop populations for 171 Å).

In the following sections, these results are further broken down into more detailed analyses of structure widths and asymmetries.

6.2.1 Width Profiles

Plume slopes in the full 2-10 pixel width range are shown in Figure 6.3, results summarized in Table 6.1. In the range of 2.7-5 pixels, slopes are more constrained, and the results from this subsection are shown in Figure 6.4 and summarized in Table 6.5. The distribution of these profiles show less of the thresholding effects at higher widths than loop profiles, but higher width structures are still rare in 304 Åand entirely absent from 211 Ådistributions. The widths seen in plume populations vary by period, wavelength, and the width range analysed. Quantitative comparisons and analysis is restricted to the 2.7-5 pixel range, where bins are less affected by small number fluctuations of bins at low frequency values drastically affecting fit slopes.

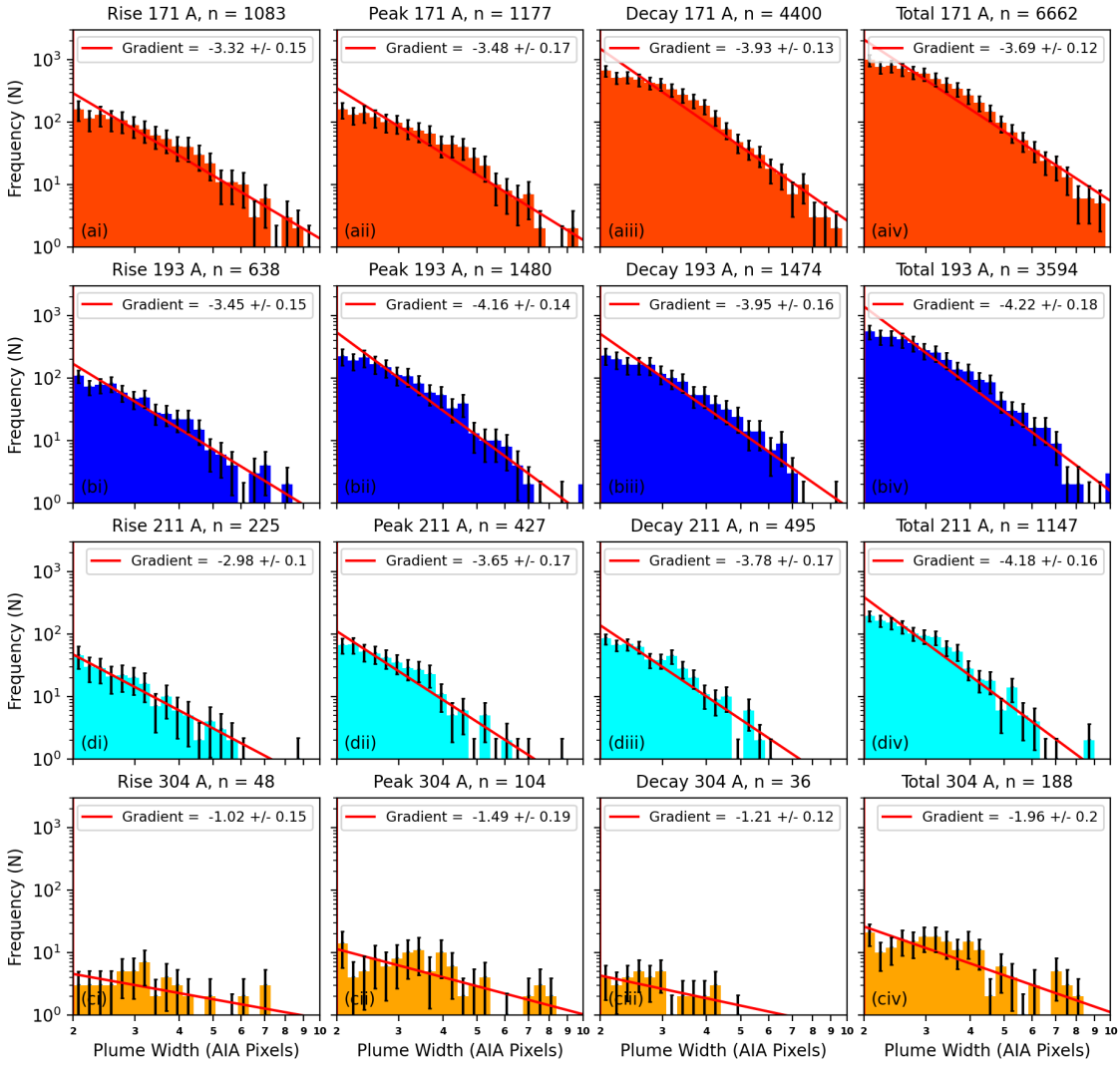

Figure 6.3: Figure of polar structure width (x axis) vs frequency (y axis) between 2 and 10 pixels. Rise (i), peak (ii), decay (iii) and total (iv) phase distributions separated, displaying varying power law profiles.

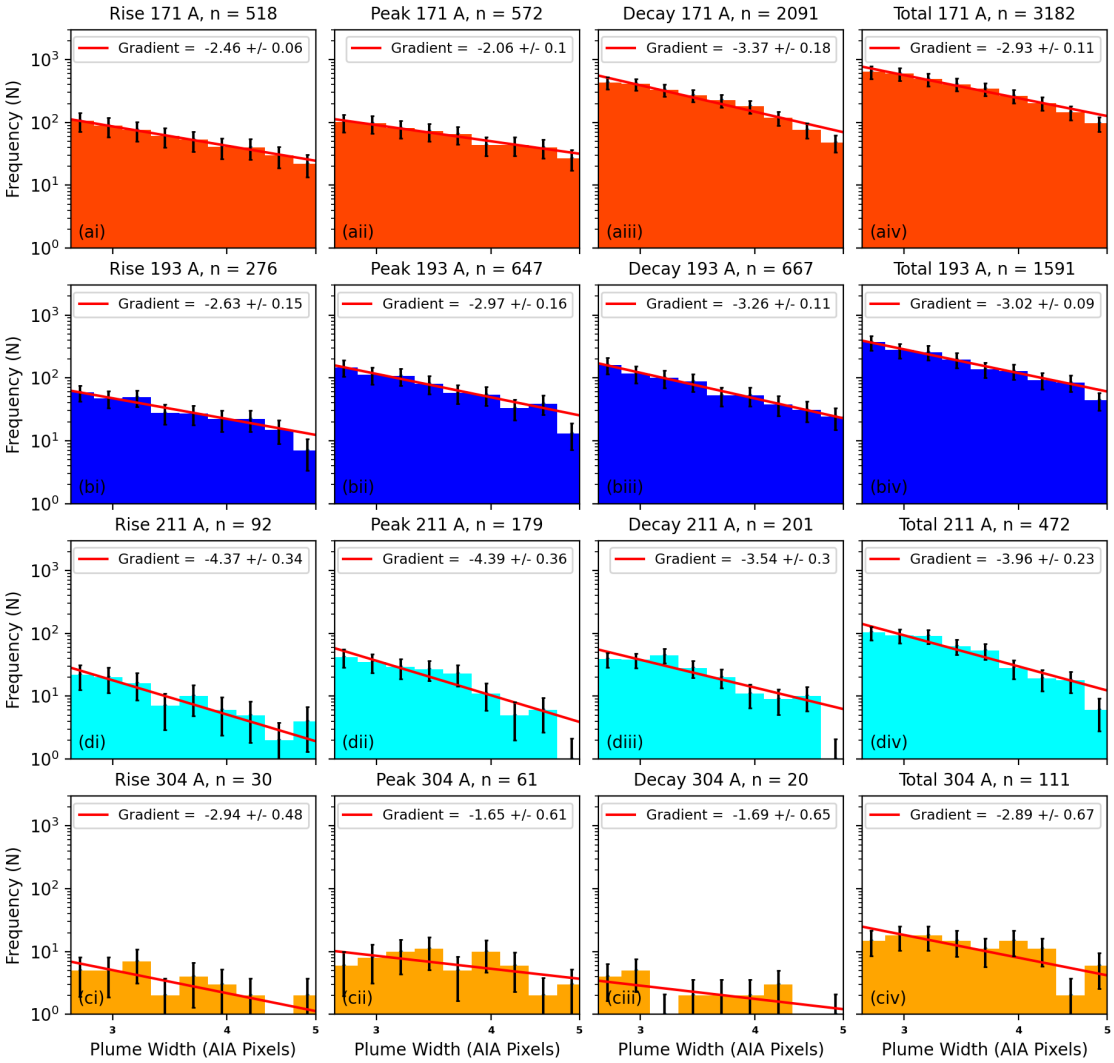

Figure 6.4: Figure of polar structure width (x axis) vs frequency (y axis) between 2.7 and 5 pixels, equivalent to the range shown in reduced active region structure diagrams. Fig 5.3. Rise (i), peak (ii), decay (iii) and total (iv) phase distributions separated, displaying varying power law profiles.

Table 6.4: Width frequency power law slope by time period and wavelength - 2-10 pixel widths

Wavelength	Rise	Peak	Decay	Total
171	3.32 ± 0.15	3.48 ± 0.17	3.93 ± 0.13	3.69 ± 0.12
193	3.45 ± 0.15	4.16 ± 0.14	3.95 ± 0.16	4.22 ± 0.18
211	2.98 ± 0.1	3.65 ± 0.17	3.78 ± 0.17	4.18 ± 0.16
304	1.02 ± 0.15	1.49 ± 0.19	1.21 ± 0.12	1.96 ± 0.2

Table 6.5: Plume width frequency power law slope by time period and wavelength - 2.7-5 pixel widths

Wavelength	Rise	Peak	Decay	Total
171	2.46 ± 0.06	2.06 ± 0.1	3.37 ± 0.18	2.93 ± 0.11
193	2.63 ± 0.15	2.97 ± 0.16	3.26 ± 0.11	3.02 ± 0.09
211	4.37 ± 0.34	4.39 ± 0.36	3.54 ± 0.3	3.96 ± 0.23
304	2.94 ± 0.48	1.65 ± 0.61	1.69 ± 0.65	2.89 ± 0.67

General trends for both the full 2 - 10 and restricted 2.7 - 5 pixel width range vary by wavelength. Quoted slopes are for the restricted range, as this the range with the best fit.

171 Å remains the most populated plume population and also the one with the lowest slopes in both the full and restricted pixel ranges. Gradients in this wavelength follow the same trend as those seen in the closed active region populations, namely that the rise phase slope (2.46 ± 0.06) is steeper than the peak phase (2.06 ± 0.1), and the steeper decay phase slope (3.37 ± 0.18) steeper than both. The overall slope for all plumes in this range is 2.93 ± 0.11.

193 Å differs from the 171 Åpopulation in its trends throughout the cycle. It possesses a shallow rise phase slope (2.63 ± 0.15) with progressively steeper slopes

throughout the cycle; a steeper peak phase slope(2.97 ± 0.16), and a slightly steeper decay phase slope (3.26 ±] 0.11) and an overall slope of 3.02 ± 0.09. Though this overall slope is very similar to the slope of 171 Å, the specifics of each phase and the change between them indicates a different relationship between this wavelength and the activity cycle in the open polar region.

211 Å represents a less well populated distribution than 171 or 193 Åand this is reflected in higher uncertainty values for slopes. Possessing less than 500 detected structures overall, it is difficult to make well evidenced statements about the behaviour of the corona in the polar regions in this wavelength, but the general trend displayed seems to differ from both 171 and 193 Å. In this wavelength, the rise phase slope (4.37 ± 0.15) is less steep than the peak phase slope (4.39 ± 0.36), which is shallower than the decay phase slope (3.54 ± 0.3). The overall slope is 3.96 ± 0.23. Despite the overall values of the slopes being much steeper than other populations, the change between phases indicates the possibility of a different relationship between the 211 Åwavelength corona and the solar activity cycle than other wavelengths for plume populations.

304 Å plumes are under populated, and it is unlikely that much analysis can be confidently made with the plume populations in each phase in this wavelength. With just over 100 plumes total, the 304 Åpopulation possesses an overall slope of 2.89 ± 0.67. Further analysis would require a higher population sample size to properly develop the differential slope.

The width profiles seen by plumes observed in these time periods vary substantially from loop population profiles, steeper by a least one in all measured slopes - these populations are heavily affected by the relatively low number of plumes.

Taking into consideration lower population numbers, and that the north and south polar regions constitute two spatially distinct regions of the corona, analysis of slopes by hemisphere throughout all periods of the solar cycle between 2.7 and

5 pixel widths were undertaken to examine any possible variance of coronal power law slopes between the two hemispheres. The results are displayed in Figure 6.5 and Tables 6.3, and 6.6.

Table 6.6: Plume width frequency power law slope by time period and wavelength - 2.7-5 pixel widths

Wavelength (Å)	North	South
171	3.17 ± 0.13	3.13 ± 0.09
193	2.89 ± 0.11	3.30 ± 0.10
211	3.68 ± 0.30	5.05 ± 0.35
304	2.18 ± 0.50	1.48 ± 0.43

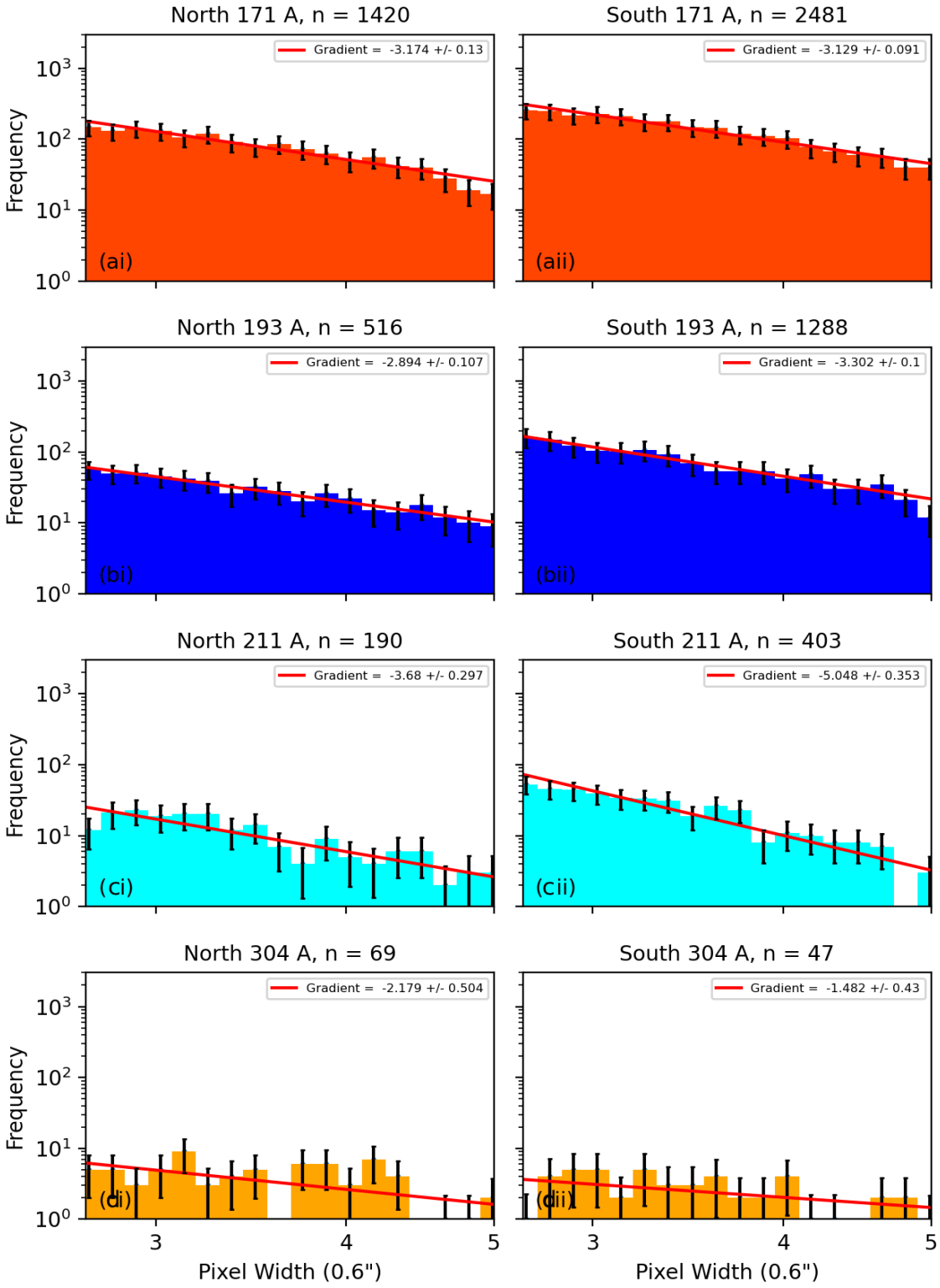

Figure 6.5: Plumes frequency (y axis) versus width (x axis) between 2.7 and 5 (full physical range) pixels in width in all wavelengths. Note a marked discrepancy between n in N population and S population.

Generally speaking, these slopes appear to agree with overall slopes seen in the populations by time period. More specifically;

171 Å possesses almost identical slopes in the north and south hemisphere (3.17 ± 0.13 in the northern hemisphere, 3.13 ± 0.09 in the southern hemisphere), with close agreement to the overall slope in both hemispheres of 2.93 ± 0.11. This could indicate a low degree of variability between hemispheres for the 171 Åcorona.

193 Å displays a moderate degree of of variation between hemispheres, with both distributions appearing well fit; 2.89 ± 0.11 in the northern hemisphere, 3.30 ± 0.10 in the southern hemisphere, a variation of close to 0.5. These values are close to the overall slope of 3.02 ± 0.09, though this could indicate a larger degree of difference between the 193 Åcorona in the north and south poles throughout Cycle 24 than compared to 171 Åstructures.

211 Å shows a large degree of variation between hemispheres, though the northern population is less well populated than the southern population. The southern population also seems to suffer from a lack of widths in certain bins which may skew the slope. The northern slope in this time wavelength is 3.68 ± 0.30 and the southern slope is 5.05 ± 0.35, which is the steepest slope yet recorded for a coronal structure population. This degree of variation is close to 1.5, and could indicate a major difference in conditions for coronal populations in 211 Åin each hemisphere, though low population numbers make this difficult to analyse.

304 Å continues to lack sufficient numbers to draw meaningful analysis from, though it is notable in that it is the only wavelength to display more detected structures in the northern hemisphere than in the south. The recorded slopes are 2.18 ± 0.50 in the north, and 1.48 ± 0.43 in the south respectively.

Apart from the trends in slopes indicating a potential variation in conditions between wavelength populations which have not been detected in active region populations, it is notable that the asymmetry between the hemispheric populations is

pronounced; 2481 southern structures for 171 Åcompared to 1420 northern structures, 1288 southern 193 Åstructures compared to 516 northern structures etc. This represents a much higher asymmetry in coronal activity than was detected for closed active region loops, and this asymmetry may be important in describing the changing distribution of structure in the corona across Cycle 24. The following section outlines results relating to colatitude frequency and plume asymmetry in more detail.

6.2.2 Latitudinal distribution of plumes

The colatitude distribution of plumes in the range of 2.7 - 5 pixel widths is displayed in Figure 6.6 for corrected colatitude plumes and in Figure 6.7 for uncorrected colatitude plumes. Table 6.7 describes the N-S asymmetry of these plume populations by wavelength and time period. As these regions contain coronal holes whose exact dimensions and topologies are complex and change throughout a solar cycle (Hewins et al., 2020; de Toma, 2011), these colatitude descriptions are to be considered averages of the polar region distributions.

Table 6.7: North-South plume asymmetry in three time periods. Left column F represents north hemisphere plumes as a fraction of total plumes. Right column A represents N-S loop asymmetry index for chosen period and wavelength.

Wavelength	Rise		Peak		Decay		Total	
	F	A	F	A	F	A	F	A
Sunspots	0.68	0.36	0.37	-0.27	0.73	0.46	0.54	0.22
171 Å	0.31	-0.38	0.29	-0.41	0.38	-0.23	0.34	-0.31
193 Å	0.53	0.05	0.17	-0.66	0.3	-0.4	0.28	-0.44
211 Å	0.68	0.36	0.11	-0.78	0.23	-0.53	0.28	-0.44
304 Å	0.54	0.08	0.65	0.3	0.71	0.42	0.65	0.3

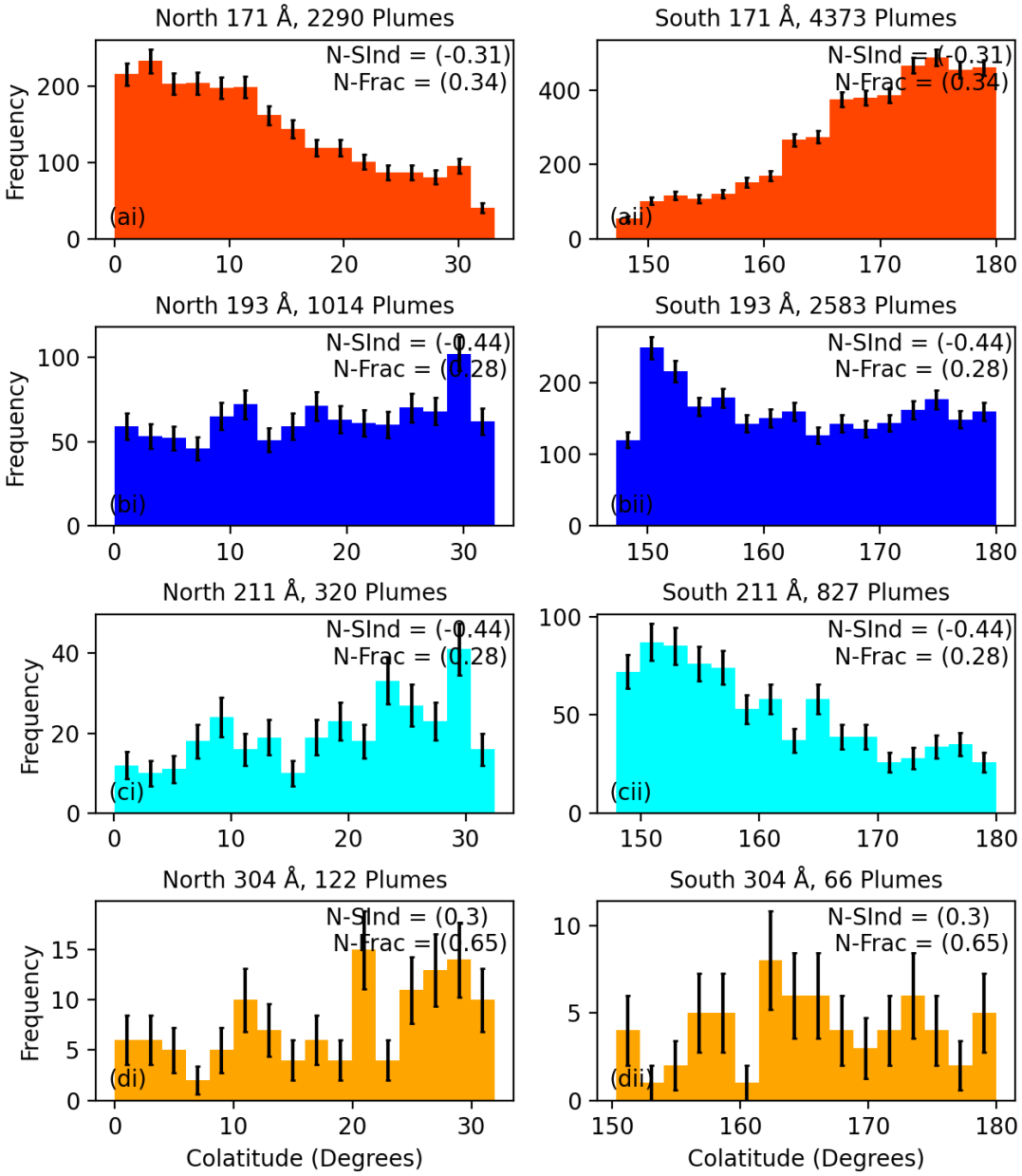

Figure 6.6: Plumes frequency (y axis) versus corrected colatitude (x axis) between 2.7 and 5 (conservative range) pixels in width in all wavelengths. $\sqrt{N}$ error for each bin indicated by error bar.

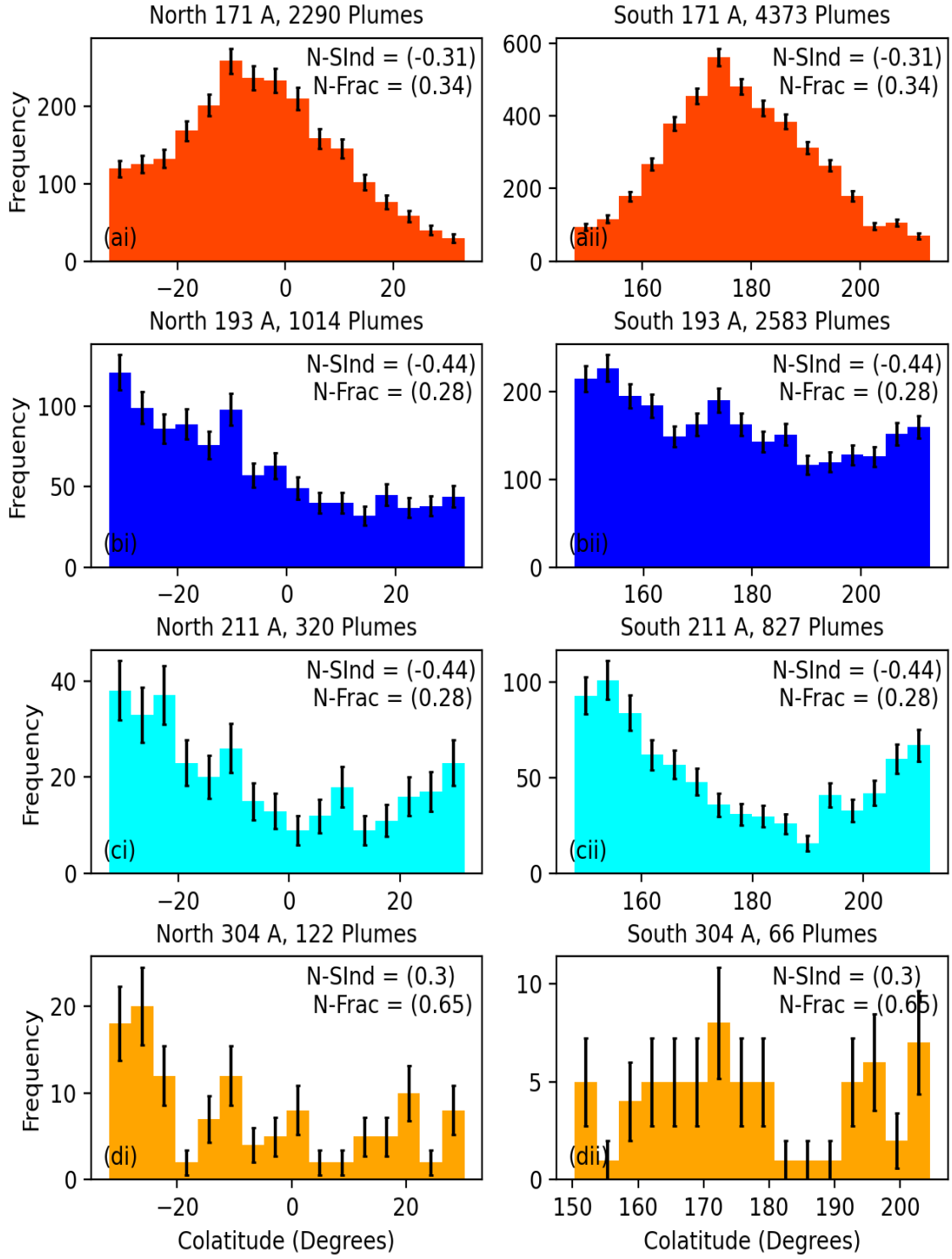

Figure 6.7: Plumes captured between 2.7 and 5 (conservative range) pixels in width in all wavelengths, with relative instead of absolute distance from the north pole. $\sqrt{N}$ error for each bin indicated by error bar.

6.2.2.1 Corrected Latitudes - Figure 6.6

From these, there are differing distributions of structures in differing wavelengths.

171 Å distributions appear to conform to a distribution which correlates to the depth of the line-of-sight over the polar region, with the detected number of structures decreasing sharply with distance from the center of the polar regions.

193 Å appears to demonstrate a shallow distribution, with only a small variation between the highest and lowest populated areas. The highest concentration of 193 structures appears to be at both the center and the edge of the polar regions, which places it as an intermediary between 171 Åand 211 Å

211 Å displays a different profile to the 171 Åand 193 Åprofiles, with an inverted relationship to distance from the northern and southern pole, with a much higher number of structures appearing at the edge of the polar region. This profile is more well defined in the southern hemisphere owing to the greater number of structures.

304 Å populations are likely too sparse to draw meaningful analysis, but the north population seems to roughly resemble the distribution of 211 Å, with greater numbers of detected objects away from the north and south poles within the polar region whilst the southern population is predominantly flat.

6.2.2.2 Uncorrected Latitudes - Figure 6.7

The uncorrected distribution represents plumes between 2.7 and 5 pixels with their position relative to the north pole, with negative values indicating counterclockwise angular distance. ie; -30 degrees = 30 degrees towards the eastern equator.

171 Å shows peaks in both the northern and southern hemispheres which occur between -12 and -9 degrees and 172 and 176 degrees respectively. This peak appears better defined in the southern hemisphere, but this may be due to the relative abundance of structures in the southern hemisphere. This would indicate a distribution that favored direct line-of-sight depth across the polar region, as the number

of structures detected appears to be proportional to center of the imaged region.

193 Å displays a profile which appears to be a combination of both the peaked distribution of hemispheres, with a distribution skewed towards anticlockwise that also contains a spike in ranges corresponding to the center of the polar region. Though this is more difficult to determine in the north due to a less well populated distribution.

211 Å profiles are similar for both hemispheres, displaying a sharp decrease in visible structure detection from the outermost to innermost region, with a strong preference for the counterclockwise region similar to the 193 Åpopulation.

304 Å is the most difficult wavelength to describe adequately, owing to the very low populations of structure present to fill out a spatial distribution. In the north, these structures appear to take on an S-shape favoring the anti clockwise direction towards -30, though the south seems more similar to 171 Åin containing some kind of peak towards the center of the polar region. Both regions however contain bins with very low or no recorded structures.

6.2.2.3 Asymmetries

The degree of asymmetry shown in the polar corona (table 6.7) across Solar Cycle 24 is to a much greater extent an inverse of that seen in sunspot data. The asymmetries by period shows a large degree of variability between wavelengths and time period.

Rise phase shows a mixed distribution for wavelengths, e.g; for 171 Åvs sunspots, with 0.31 northern plume fraction and -0.38 plume asymmetry index versus 0.68 northern sunspot fraction and 0.36 sunspot asymmetry index with other wavelengths remaining north dominant. This may be due to a relatively low number of structures in this period and time.

Peak phases are nearly universally southern dominant; 171 Ådisplaying 0.37 northern fraction and -0.27 asymmetry index of sunspots versus 0.29 and -0.41 .

Overall asymmetry seems to remain in the southern hemisphere despite the overall southern dominance in sunspot periods at this time. These are much more asymmetric than closed equatorial region structures in the same time period (table 5.6), with 89 percent of 211 Åstructures appearing in the southern hemisphere.

Decay phase represents a less extreme southern dominant period, with 0.38 northern fraction and -0.23 asymmetry index in 171 Åcompared to 0.73 and 0.46 for sunspots. 304 Åseems in agreement with sunspot figures and has remained northern dominant for the entire cycle.

In **Total**, the expectation of a polar corona asymmetry which is anti correlated with equatorial active region activity by hemisphere is mostly observed, but interestingly this correlation does not significantly seem to shift the total fractions. It is possible that, even though N-S numbers became less southern dominated, this was due to smaller numbers of plumes in total.

6.2.3 Confirmation of Asymmetry Results

To confirm the high asymmetry values described in the prior results section, a test was performed to investigate the algorithm used for hemispheric bias. To demonstrate this, a plot demonstrating the cross correlation value of plumes in both the normal configuration and image data which had been inverted vertically is shown in Figure 6.8 is produced to demonstrate the optimal positioning of the data series of sunspots and plume numbers extracted by both inverted and normally aligned datasets by hemisphere.

These results, shown in figs 6.8 and 6.1 and especially the asymmetry evaluations were tested in the same manner as the Loops results (Chapter 5). Firstly by plotting the normalized frequencies of sunspots and plumes to examine trends in asymmetry. Secondly, this was repeated on a vertical inversion of the image dataset, allowing the resulting correlations to be compared to test for hemispheric biases in

plume detection and measurement. This test is important for plume results, as the asymmetries detected in these datasets were significantly larger than those in the active region datasets (60-70 percent asymmetry towards southern hemisphere plumes as opposed to 45 percent asymmetry towards northern hemisphere active region structures.) This demonstrates that there is no undue hemispheric bias and these asymmetries are genuine observations in plume populations. These plots are very close to but not inverted copies of one another, and this could be due to the change in orientation of the input image causing minor changes to the output image during the signal processing phase, as pixel intensity values are transformed when the images are flipped or rotated.

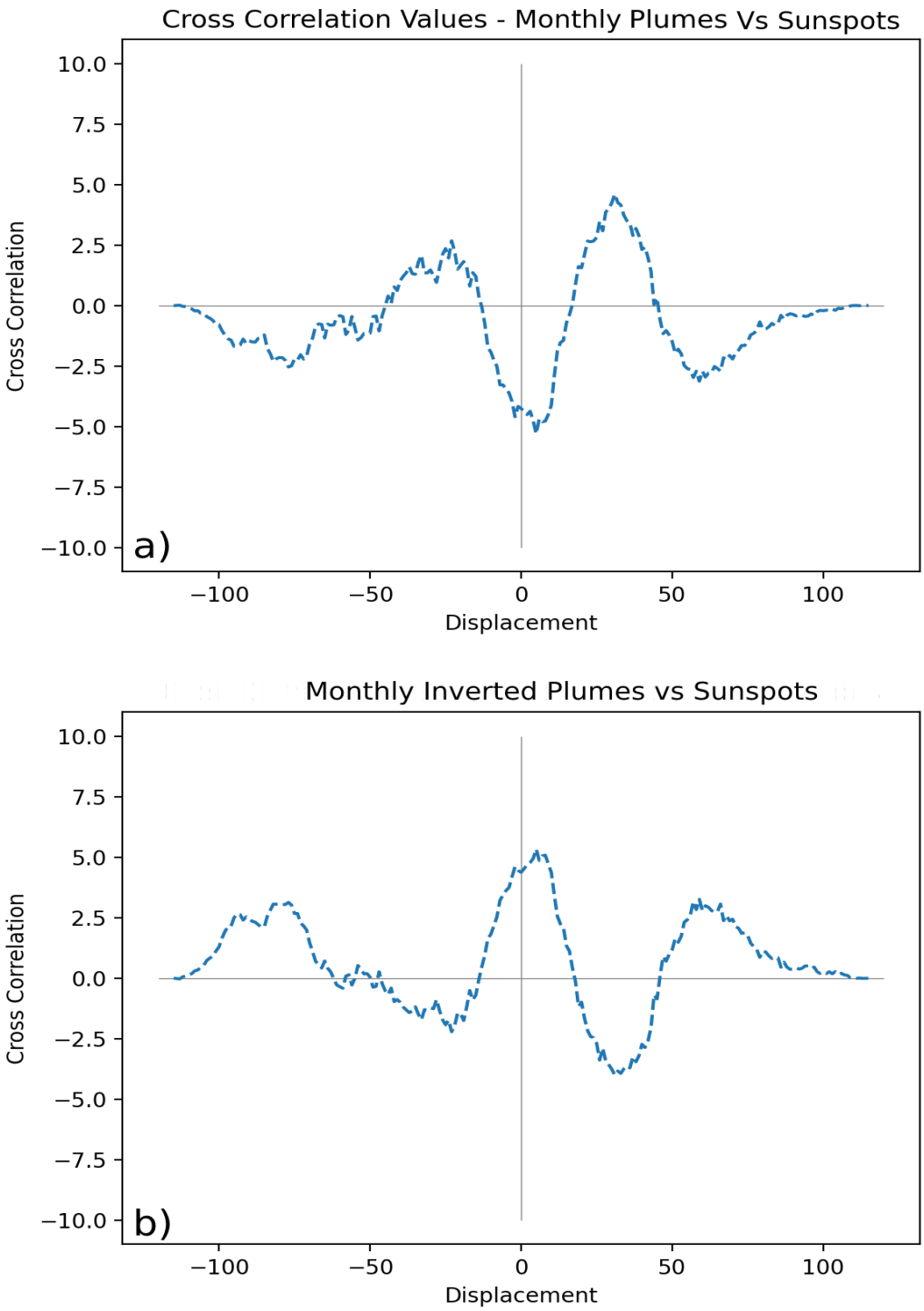

Figure 6.8: The cross correlation of the North - South plume frequency and sunspot frequency (y axis) versus time (x axis) for both (a) standard plumes and (b) plumes detected in the vertically inverted image data set.

6.2.4 Intensity vs Width

Similarly to earlier analysis in Chapter 5, the intensity and width relation of each recorded plume in the extended 2 - 12 pixel range is demonstrated in Figure 6.9. In this figure, plumes are shown to vary little in intensity by wavelength, the black dashed line indicating the average intensity of plumes within a 0.25 range of the black dot. These lines remain consistently flat, and a Spearman Rank Correlation performed on these populations indicated R values of 0.08, 0.01, -0.01, and 0.23 for 171, 193, 211, and 304 Årespectively. Given the very low population size for 304 Å, these results do not indicate that there is any evidence of a relationship between width and intensity for plume populations observed in Solar Cycle 24.

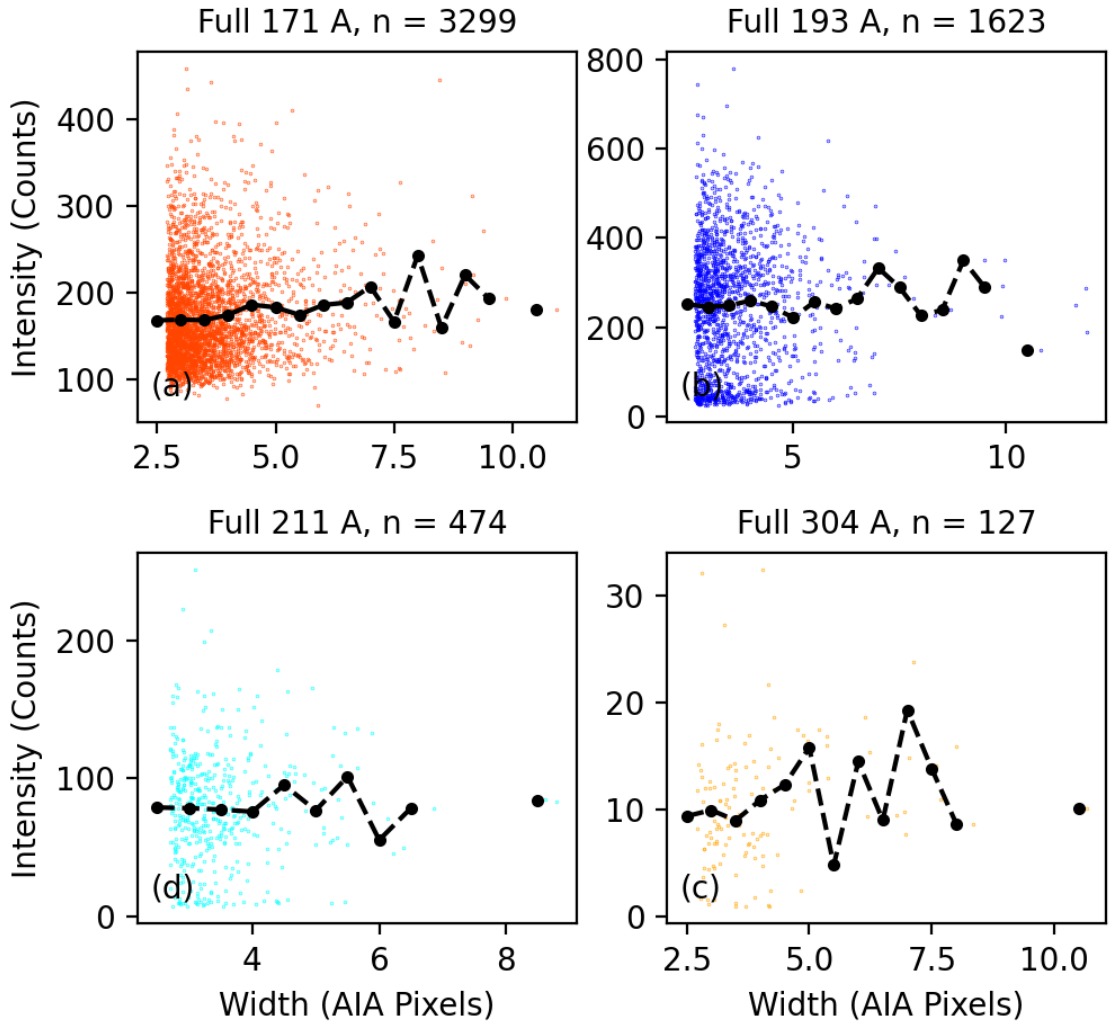

Figure 6.9: The intensity (y axis) vs width (x axis) of plumes recorded in the 2-12 pixel width range. Black dashed line is the average intensity of plumes within a 0.25 pixel width range within 171 (a), 193 (b), 211 (c), and 304 (d) Åfor all time phases.

6.3 Discussion

6.3.1 Width Populations

Observed plume power law profiles vary from those seen in closed active region populations, with slopes in the range of 2.7 to 5 pixels ranging from -2.06 ± 0.10 for 171 Åto -4.39 ± 0.36 for 211 Åin the Peak period. This varies significantly from active region power law slopes, with plume power law slopes universally steeper, varying between 0.6 to 2.2 steeper than equivalent active region populations at the same time period. This appears to indicate that plumes tend to be narrower on average than active region loop structures, but it must also be noted that the frequency of structures is more than an order of magnitude lower in the open plume population versus the closed loop population for some wavelengths (3182 vs 17430 for 171, 472 vs 7285 for 211 etc..).

This draws into question whether some of the observed plume slopes represent populations of structures which genuinely display an altered probability distribution of widths, or whether statistical effects of small number variations (in 211 and 304 Åparticularly) become a more significant source of observational disruption to the underlying distribution. For example, the relatively stable conditions of the polar corona and the lack of complex, tangled structures in the line-of-sight may create conditions which favor detection of narrower structures. In comparison, the active region detections of narrower structures may be associated with more complex geometries, either locally bound as part of collection of structures in an active region, or anywhere along the line-of-sight. This obfuscation of smaller loop structures is an example of an observational effect thresholding the power law distribution of a loop population. If these different regions experience variation in the intensity of their thresholding effects, this may also influence the observed power laws of structural widths within that region without necessarily changing the true physical properties

of structures in either region.

If the difference is primarily within the formation region ie, the footpoint of the structures, then it would be expected that these profiles would possess a different power law. Differences in the formation region would result in a difference of the parameters of the SOC model, assuming reconnection in these regions can be described in an SOC like manner. This might result in a change in the effective fractal space dimension of the reconnection space (e.g; is the reconnection space truly three dimensional or is there preference to one plane over another?) or in the diffusivity (how easily does reconnection cascade across all available scales in the reconnection space?).

For periods containing less than five hundred total detected structures, meaningful analysis is limited by variability of histogram bins, leading to greater uncertainties. As a result, in the following only the 171 193 Åwidth results by region will be discussed in detail.

For **171 Å**, the overall trend of steep rise period slope (-2.46 $\pm$ 0.06), gentler peak period slope (-2.06 $\pm$ 0.1), and steeper decay period slope (-3.37 $\pm$ 0.18) appears to be in agreement with the pattern observed in loops, and this may indicate that at least some of the same process by which the solar cycle is influencing the width distribution profile of coronal structures is also operating in the polar regions. However, the slope for the distribution across the entire solar cycle is markedly steeper than that seen in the active loop data, -2.93 $\pm$ 0.11 for plumes versus -1.81 $\pm$ 0.06 for the active region. This could be as a result of the smaller population in the polar region, but the relatively small uncertainty of slope of the line of slope indicates that the distribution was well populated in the range of 2.7 to 5 pixels. This variation, if genuinely physical and not a result of observational or statistical deviation represents a definitive departure from the expected 1.5 value predicted by SOC that would need to be explained by conditions at the formation regions of

these structures.

For **193 Å**, the overall trends are more difficult to discern. Though the decay period still has a steeper slope (-3.26 ± 0.11) than the peak period (-2.97 ± 0.16), the rise period has a gentler slope than both of these (-2.63 ± 0.15); All of these are within error of one another, and so may represent a different relationship than that seen in 171 Å. While this does contradict the trend identified in the loops and the polar 171 Åpopulations, it also only contains 276 structures in total, the large uncertainty indicates that this range was not well populated. If a larger population size were to confirm this result, it would indicate that the 193 Åplumes were being influenced to a differing degree by changes in the solar cycle. The total population slope for 193 Åplumes displays a slope which is almost identical to the total 171 Åpopulation, with a 0.003 difference well within the margin of error for both measurements. This varies slightly from the observed difference of 0.248 between total populations for 171 Åand 193 Åloops (1.80 and 2.05 respectively, see Figure 5.3), which is greater than the sum total of their uncertainties (0.11 and 0.09, respectively), indicating a subtle distinction between the two populations. It will likely require more robust statistical populations and observation in the polar regions to determine whether this represents a difference in the behaviour of 193 Åand 171 Åstructures in the open polar region compared to the closed loops region.

Unlike the loops, where sunspots cause the appearance of loops in the active region belts, polar plumes appear two distinct spatial regions of the solar atmosphere - the north and south poles, and thus represent two different populations which can be compared for the purposes of studying N-S asymmetries in number and power law distribution.

The result of compiling separate distributions for each hemisphere over the entire solar cycle is shown in Figure 6.5. Though this does not capture the evolution of all polar regions throughout the solar cycle, and each hemisphere will experience its

own phase of declining and increasing activity, any difference in these populations may be seen in the power law slopes. From these results, 171 Åpopulations appear to be similar between hemispheres, with a northern hemisphere slope of -3.17 ± 0.13 and a southern hemisphere slope of -3.13 ± 0.09. This is despite a large discrepancy between the frequency of plume structures in these two hemispheres; southern hemisphere structures almost twice as abundant (2481) than northern structures (1420). This would seem to indicate that either the activity of the entire solar cycle produces a fairly consistent distribution of plumes in either hemisphere, as each hemisphere experiences an (asymmetric) rise and fall in magnetic activity.

6.3.2 Colatitude Distributions and Coronal Polar Topology

The results shown in Figure 6.6 vary from those seen in active region distributions, (see Figure 5.5) in that it describes the frequencies of structures occurring along a two dimensional line-of-sight displaced from the pole. As these structures are in reality occurring across a hemispherical, three dimensional space, these measurements of colatitude instead describe the spatial distribution of those structures throughout that three dimensional space. This introduces an additional complication when interpreting the colatitude distribution. Without true stereoscopic imaging of the coronal region, information about the exact location of an imaged structure is unobtainable. Structures seen close to the poles in either hemisphere are likely displaced away from the pole ie; towards the boundaries of the polar region.

As described in section 2.6, the distribution of plume latitudes is displayed by histogram. Each bin of this histogram, by necessity of geometry represents the summed total of structures seen within the width of the bin along the line-of-sight. This value is itself an integral of the observed distribution of structures at a particular range of latitudes at the height of the observational annulus. Each bin represents a horizontal range on either side of the pole, and the observed value is equal to the

density of the structures within that range multiplied by the area of the rectangle constructed by the binning process.

Firstly, these colatitude distributions appear very similar across each hemisphere for all lines, despite the comparative lack of structures in the north (only 36 percent of structures in the north compared to the south for 171 Å). This may indicate a topology which is consistent despite the varying intensity of the local polar magnetic field across the solar cycle, which influences the number of structural detections but not their spatial displacement from the pole.

Secondly, the histograms present in Figure 6.5 indicate the presence of a polar corona which is stratified by temperature depending upon the depth of the line-of-sight. The distributions of plumes in each wavelength are as follows;

171 Å profiles (Figure 6.6ai and 6.6aii) show an S shaped profile consistent an interpretation of even structure coverage throughout the entire surface area of the coronal hole below the imaged region. Given that distance along the x axis is consistent with the optical line-of-sight across the polar region, this is the simplest assumption that can be made with the data available.

193 Å distributions (6.6bi and 6.6bii) exhibit a mostly flat distribution, with plumes no more or less likely to be seen away from the central pole. This could indicate that 193 structures are less likely than 171 Åstructures to form in the central regions closest to zero latitude, and that some structures seen at this colatitude may actually be displaced away from the poles on both the close and far side of the pole.

211 Å distributions (6.6ci and 6.6cii) display a correlation between frequency and latitudinal displacement from the pole. This is in contrast to the relationship exhibited by 171 Åstructures, and indicates that it is more unlikely that 211 Åstructures form frequently in the central latitudes of the polar regions.

304 Å plumes (6.6di and 6.6dii) may show a similar displacement to 211 Åplumes,

but it is difficult to discern given the low number of structures seen in this wavelength. Of some note, this is the only wavelength where the northern hemisphere displays more structures than the southern hemisphere (126 in the north versus 73 in the south) Though these are small numbers compared to other wavelengths.

These distributions place 171 Åstructures as being more "central" in the polar regions, in contrast with 211 Ådisplaying the opposite (ie; with most detected structures occurring towards the edge of the polar regions). 193 Åis something of an "intermediary" between these two, appearing at all visual latitudesalmost equally. Given that these wavelengths describe an ascending order of temperature, (171, 193, 211 Årepresenting 600,000 K, 1,000,000 K and 2,000,000 K respectively), this indicates a temperature stratification within the polar corona which is detectable and consistent in both hemispheres. This is in contrast to closed region populations (see Figure 5.9), where loops of differing wavelength populations did not appear to display varying latitudinal dependencies. This is consistent with previous descriptions of the polar regions as displaying hotter structures at the boundaries of the open flux region of the coronal hole, caused by reconnection with closed region active regions (Higginson et al., 2017).

Within the profiles of uncorrected colatitude distributions (Figure 6.7), a consistent anticlockwise tilt between 5 and 8 degrees is observed in both hemispheres, and this is clearest in the 171 Åplume population.

This tilt towards one side of the polar distribution is unexpected, given that the rotational period within the polar region is roughly thirty days, and there would be an expectation for the distribution to appear even once compiled, that is to say that an uneven distribution of polar plumes would appear on either side of the limb from the perspective of the observing instrument once time was averaged over a long enough period. It is difficult to explain why this might be the case.

One possible explanation involves uneven evolution of coronal hole coverage. The

exact position of a coronal hole can exhibit asymmetric coverage within the polar region and can vary with time, migrating and merging with other areas of open flux throughout the solar cycle, as demonstrated in Figure 6.10. If this evolution happened to coincide with the position of the observing instrument over a long enough period of time, this could influence the resulting colatitude distribution to possess a slight tilt, but this would need to be the case for both hemispheres at some point in the solar cycle, realistically in the decay phase as this is when most plumes are detected.

A second possible explanation is that the methodology is biased in some way that preferentially selects angles within the quadrants anticlockwise of 0 and 180 degrees, and that this has manifested in plume populations in a manner which has not yet been detected in other populations.

For other wavelengths, this tilt might be represented in greater numbers of plume structures appearing towards certain edges of the coronal boundary, as appears to be the case in 193 and 211 Ådistributions rather clearly. The edge of the polar region in the anticlockwise direction in the southern hemisphere has a peak detected structure count of between 50 and 60, whilst the clockwise edge (above 180 degrees) possesses a peak frequency below 30. Structure appearance may vary by wavelength, as the polar coronal holes appear differently in different wavelengths (see 6.11).

By analyzing the profile of these histograms and taking the presence of these structures to be a descriptor of the conditions of the corona beneath them, a rough approximation of coronal hole area by colatitude can be constructed, which could then be examined by time, but this method comes with a number of caveats, such as rapidly changing coronal hole conditions not being reflected, and the assumption that the

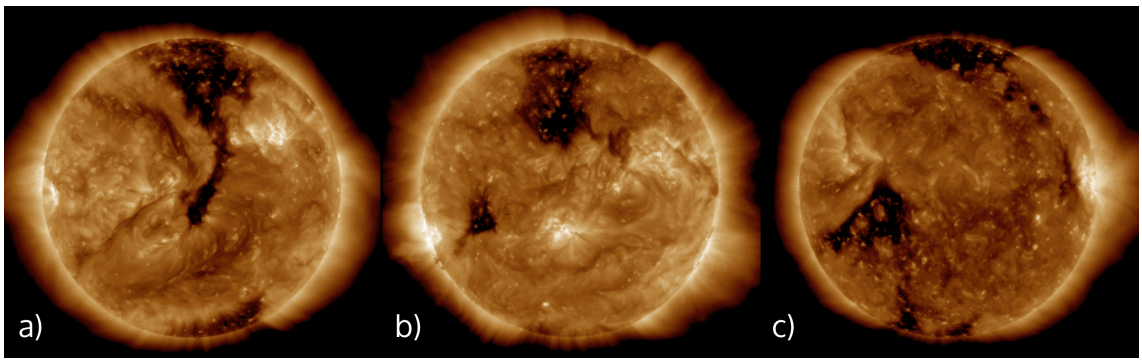

Figure 6.10: Example of polar coronal holes displaying irregular coverage in 193 Å.

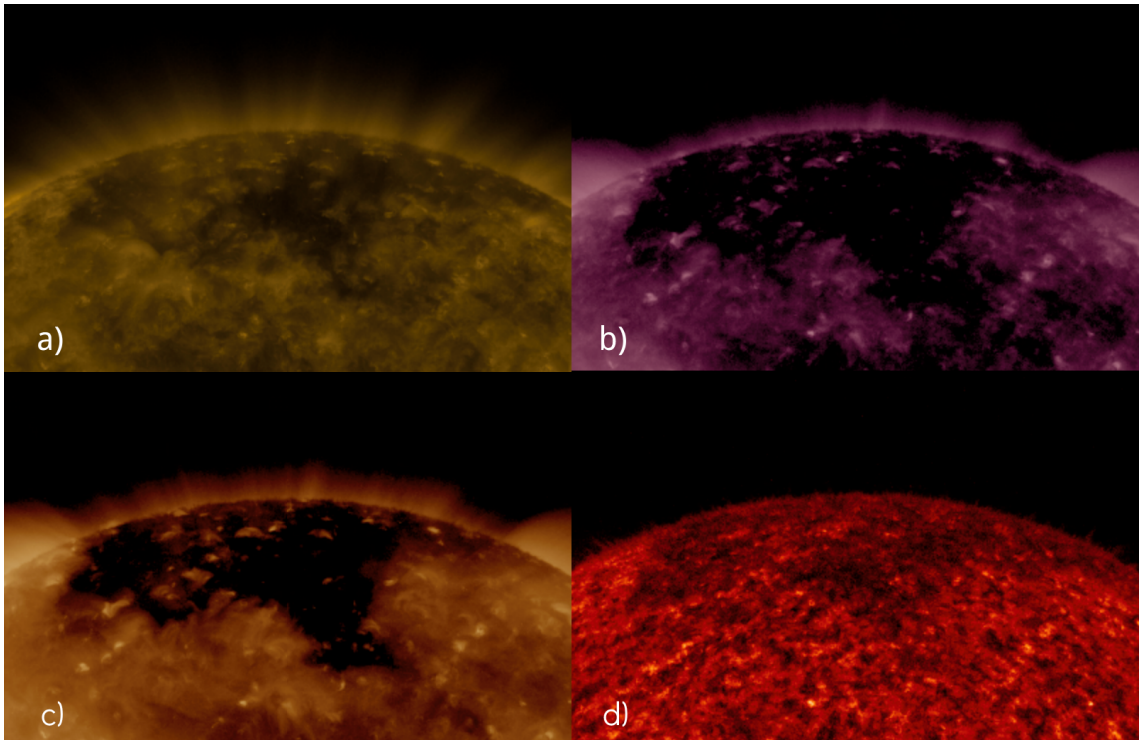

Figure 6.11: Example of polar coronal holes visible in 171 (a), 193 (b), 211 (c), and 304 (d) A respectively, demonstrating the wide range of visible structures and topologies which can be inferred by different temperature regimes.

6.4 Conclusion

Plumes from North and South polar regions were examined throughout Solar Cycle 24 by means of an automated, algorithm, surveying plume structure width employing a similar method used to examine active region loops (see Chapter 5). Results revealing the power law slopes of plume structural widths within open regions across three time periods in all wavelengths were analysed. These slopes were found to be steeper than comparative active region loops at the same part of the cycle, indicating that populations of polar plume structures were narrower on average than their equivalent active region populations. This may be due to physical effects which prevent or curtail the formation and longevity of wider structures, or it could be due to observational effects which cause narrower structures to be more easier to detect in quieter polar regions. These results can form a basis for an approximate description of physical differences between the corona in open and closed regions. The relationship between slopes in differing time periods is similar to those seen in active regions, but constraints on population sizes of plumes limit the usefulness of direct comparisons. If these values are taken to be indicative of values for open structures, which form the entirety of structure seen in the polar region, whereas the active region population which contains both open and closed structures, then the closed population would then necessarily require a lower slope than higher population structures.

Additionally, latitudinal abundances for open polar structures were recorded and analysed for their spatial distributions. These distributions demonstrated a stratified structure in the polar regions, where cooler structures primarily occupied regions away from the boundary of open flux regions, whilst hotter structures existed primarily at the interface between the open and closed magnetic flux regions. 171 Åstructures displayed a decreasing relationship with distance from the pole,

whilst 211 Åstructures displayed a profile which indicated that they occupied regions furthest from the pole. 193 Åstructures appeared to be a combination of the two profiles, with a mostly flat profile distribution. This technique demonstrated the strengths of utilizing the viewing angle to sample structures which originate on the far side of the polar regions.

Chapter 7

SOHO EIT and Solar Cycle 23

Solar Cycle 23 is the solar cycle directly preceding Solar Cycle 24, occurring from roughly 1999 to 2010, a period which coincided with greater solar activity than within Solar Cycle 24. As this period was covered by predecessor instruments to the SDO such as SOHO, an opportunity presents itself to extend the studies outlined in previous chapters. The differing technical capabilities of these instruments requires some adaptation of these techniques however, and these results may be more limited. The following chapter introduces the differing techniques developed to analyse local coronal brightenings used as a proxy of coronal activity. Code and Results provided. [1]

7.1 Introduction

Studying trends within the eleven year activity cycle can be enhanced by extending analysis to trends within a larger twenty-two year solar cycle, following the full sinusoidal pattern of hemispheric magnetic polarity. Although instrumental technology has developed significantly since the end of Solar Cycle 23, older instruments and

[1] `https://github.com/DanGass/ThesisCode`

their data catalogues such as SOHO's EIT can still represent a large wealth of unexamined data for use by solar physicists. As will be described below, this can be useful for descriptions of the spatial distribution of coronal structures and magnetic topologies, though infomation regarding fine scale detail and structural widths will be unavailable. Despite this, indices of magnetic activity and north south asymmetries such as sunspot frequency and hemispheric area coverage are well documented in this period, and will be of use in examining the dynamics of the larger twenty two year solar cycle.

7.1.1 Solar Cycle 23

Solar Cycle 23 occurred between 1999 and 2010, and in this period, magnetic activity was predominantly southern lead as opposed to the northern lead Solar Cycle 24 (Watson, Fletcher & Marshall, 2011). The breakdown of solar activity by hemisphere is seen below in Figure 7.1. As in cycle 24, the phases of rise (January 1997 to February 2001), peak (February 2001 to April 2002), and decay (April 2002 to December 2009) are defined by the relative intensities of sunspot counts.

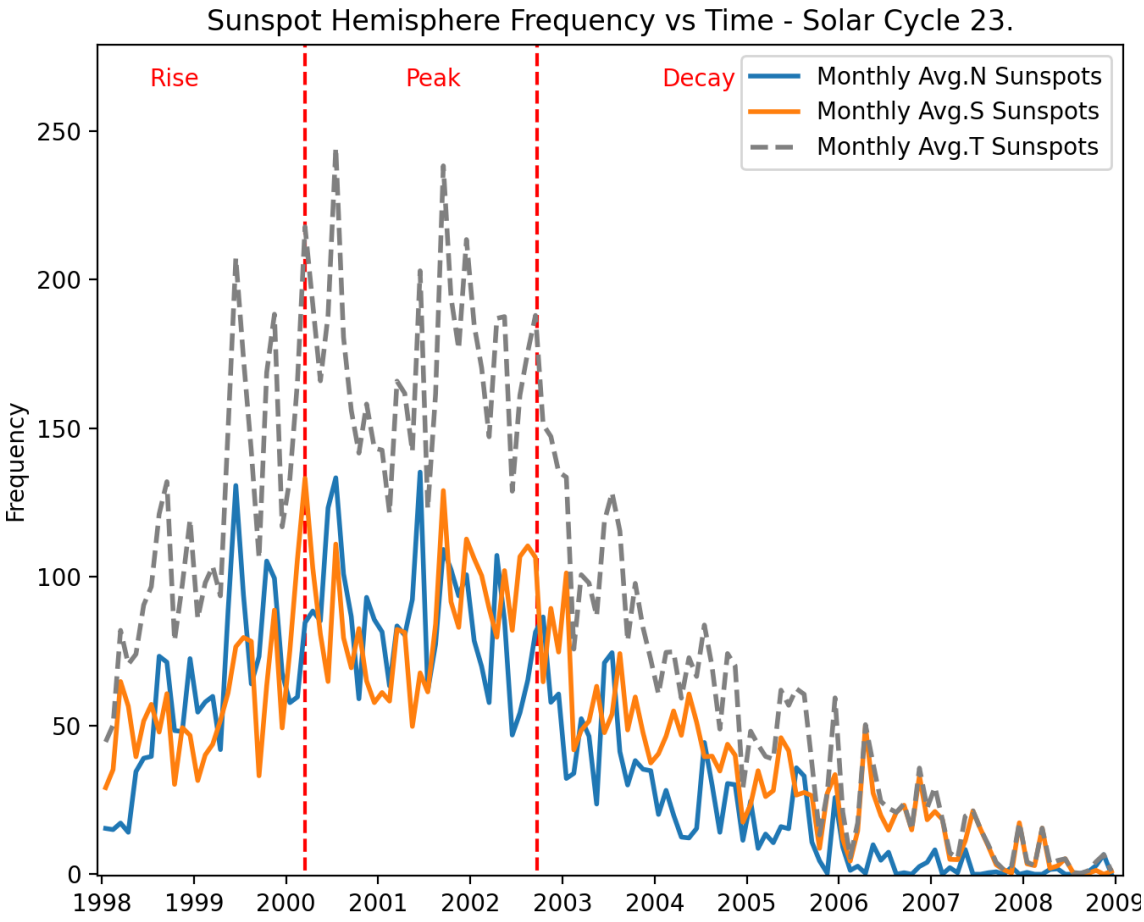

Figure 7.1: Plot demonstrating the North - South sunspot frequency (y axis) against time (x axis), between 1997 and 2009, coinciding with Solar Cycle 23.

7.1.2 EIT

The Extreme ultraviolet Imaging Telescope (EIT) (Delaboudinière et al., 1995) (see Figure 7.3 of the ESA's Solar and Heliospheric Observatory (SOHO) (Domingo, Fleck & Poland, 1995) was launched in December of 1995 and began science operations in May of 1996. The mission was placed within a halo orbit around the L1 Lagrange point of the Sun-Earth system, placing it 1.5 million kilometers sunwards from Earth.

EIT utilizes normal incidence multilayer mirrors (Stern et al., 1984), to capture four passbands in EUV. These passbands are sensitive to radiation at 304, 171, 195 and 284 , mostly from He II, Fe IX-X, Fe XII and Fe XV ion emission, with dominant temperatures of 8.0 x 10^4, 1.3 x 10^6, 1.6 x 10^4, and 2.0 x 10^4 K respectively.

EIT possesses a pixel resolution of 2.6 arcseconds with a spatial resolution of 5.2 arcseconds, with an image size of approximately 1024 x 1024 pixels, or 45 x 45 arcminutes. This represents one sixteenth of the total number of pixels compared to an equivalent AIA image, at 4096 x 4096 pixels. The detector on the EIT is shutterless, which means that light arrives uninterrupted into the detector, and regular readouts are made to produce images. This results in a low instrumental time cadence of 70 seconds and high reliability by reducing power consumption and the number of single-failure-point moving parts. However, this has resulted in a high degree of CCD degradation throughout the lifespan of the instrument. This degradation has affected some passbands to a greater extent than others. For instance, the 284 and 195 passbands appear more highly degraded than the 171 and 304 passbands. This can be seen in the "striped" banding of images is a result of uneven damaging of pixels within the CCD, and cannot be simply deconvolved (see Figure 7.2.

This relative lack of pixel resolution and variable image quality can limit long term studies of historical coronal image data, as will be explained in the following subsection.

7.1.3 Advantages and Limitations of EIT

EIT was the first instrument to provide long term, high cadence coverage of the EUV solar atmosphere. In regard to the research within the thesis, the use of this historical data to determine the topological descriptions such as widths and intensities of imaged coronal structures is more challenging. This is primarily due

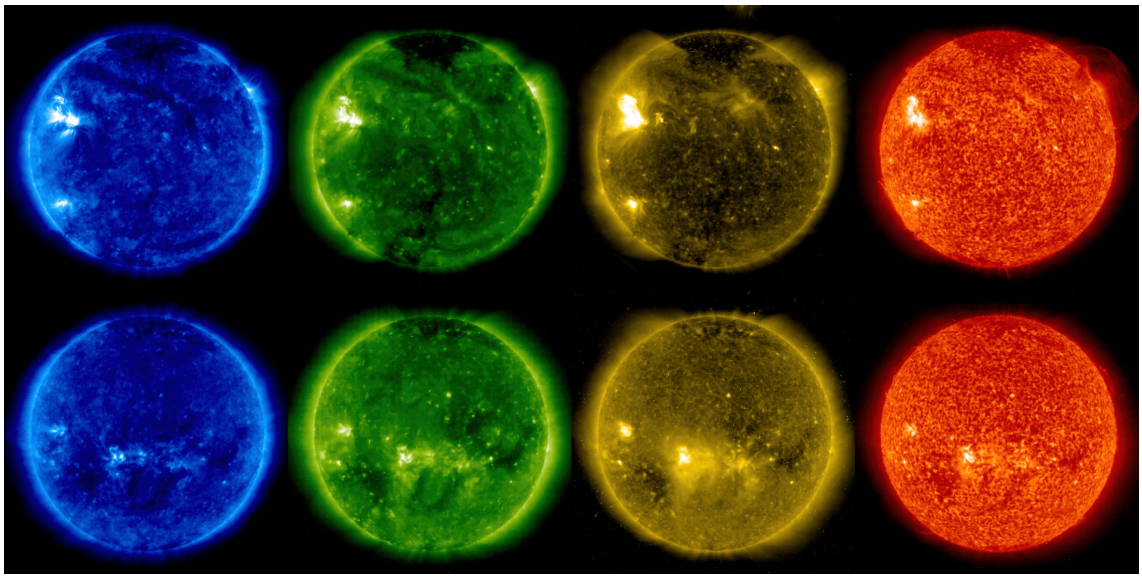

Figure 7.2: Figure demonstrating typical calibrated image frames for all passbands of EIT in ascending order of wavelength (171, 195, 284, 304 Å). Top images captured in August 1997, bottom images captured in August 2007. Degradation of image quality and "striping" effect visible.

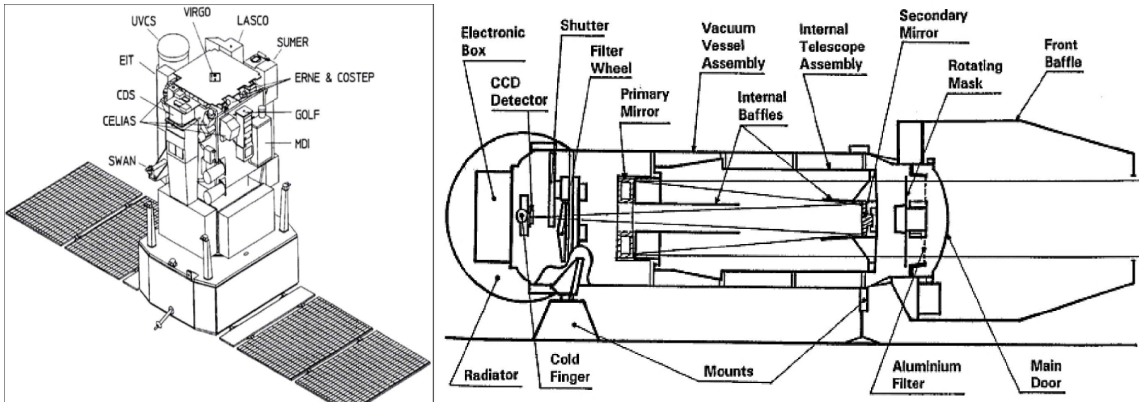

Figure 7.3: Diagram of SOHO satellite (left) and schematic of the EIT (right) (Figure 4 from the SOHO Satellite Mission Overview (Kramer, 2012b), and Figure 2 from Delaboudinière et al. (1995) respectively).

to two factors, outlined briefly above.

First, there is the limited pixel resolution of the EIT instrument. As mentioned previously, the pixel sampling of an EIT pixel is 2.6 arcseconds, meaning a spatial resolution of 5.2 arcseconds or roughly 2000 and 4000 km at the L1 orbital. This compares to 0.6 and 1.2 arcseconds for the AIA, or approximately 440 and 880 km at Geosynchronous orbit. Considering that this minimum ideal resolution is well outside of the range of the widest observed structures in the conservative (2.7 - 5 pixel width) AIA loop dataset outlined in Chapter 5, it is unlikely that a well evidenced power law can be extracted. Consequently, the derived statistics, for which widths are analysed to examine long term trends within the corona throughout Solar Cycle 23 are also likely to be limited.

Secondly, the irregular degradation of the CCD results in a complex and pronounced pattern of charge spreading and pixel damage over time. This damage is not possible to completely deconvolve from the resulting level 1 images, and so assumed values of w_{psf} and w_{noise} are likely to be significantly higher than the AIA and becomes noticeably more intense within the solar cycle. This results in observational constraints which change substantially between the start and end of the solar cycle, and becomes especially difficult to compensate for when MGN edge enhancement is applied. (see Figure 7.4). As a result, the determination of the distribution of EIT widths is likely to be severely limited across the solar cycle.

The combination of these two effects means that width measurements are very limited and lack confidence when compared to AIA width measurements. On the other hand, colatitude determinations will still be possible and defendable throughout cycle 23.

In the following Section, the methodology which will be used to analyse coronal structures throughout cycle 23 will be described, along with alterations and modifications made to the data pipeline to accommodate EIT images.

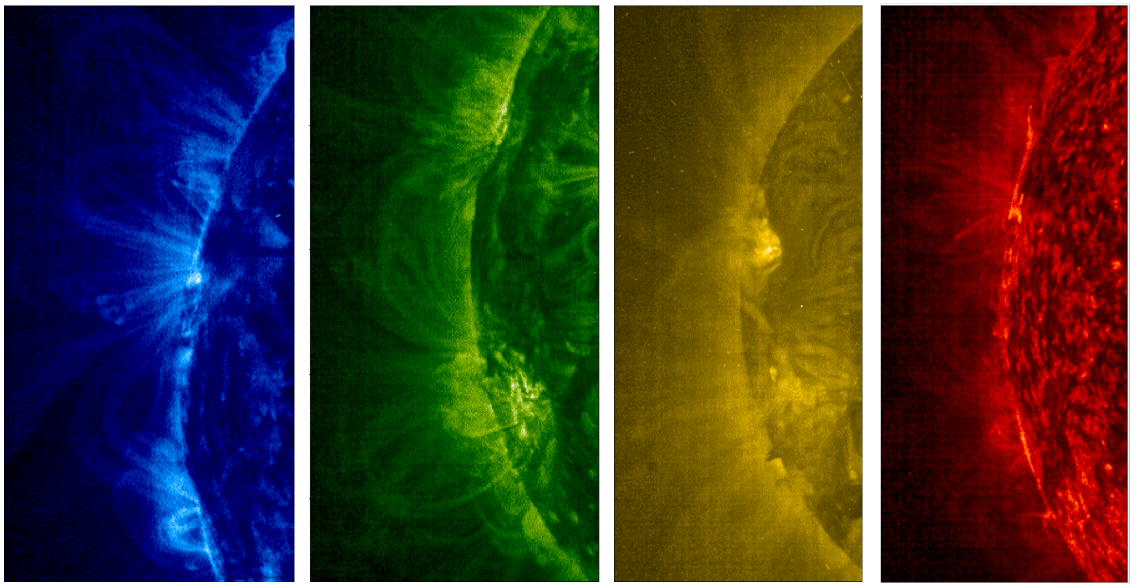

Figure 7.4: Image degradation becomes especially pronounced in image enhancement (Such as MGN as shown). Structures become difficult to dissociate with instrumental defects.

7.2 Method

Due to the limitations as described above, the method for detecting and extracting details from the low altitude (less than 1.1 solar radii) off-limb corona developed for AIA data and applied to Solar Cycle 24 will be simplified to maximise the quantity of reliable science data from EIT and across Solar Cycle 23. Measurements of physical widths are not feasible given technical limitations and are not attempted. Instead, information regarding the spatial distribution of bright coronal structures across the entirety of the solar limb is recorded, including both polar and active regions. Data is gathered from all colatitudes of the Sun simultaneously, and will produce a more detailed distribution of coronal structure location and how this may change throughout the solar cycle, providing a possible indicator of the evolving morphology of the coronal magnetic field in the period of 2000-2010. This method, which involves identifying the colatitude of local prominences in the inner annulus (described in Chapters 3, 5 and 6) in each image and compiling a distribution of their occurrence frequencies is a simplification of earlier methods, stopping before geometries are attempted to be fit across the annulus. This will allow for a statistically significant number of points to be collected across the range, but no detail on their width and geometry.

Initially, it is not possible to confirm whether all local prominences detected within this annulus are independent and resolvable structures, or whether they are simply artifacts in the image, but steps such as image enhancement and median filtering reduce the likelihood of such an event. An example of this local prominence fitting is demonstrated in Figure 7.5, where several fit points are seen in context.

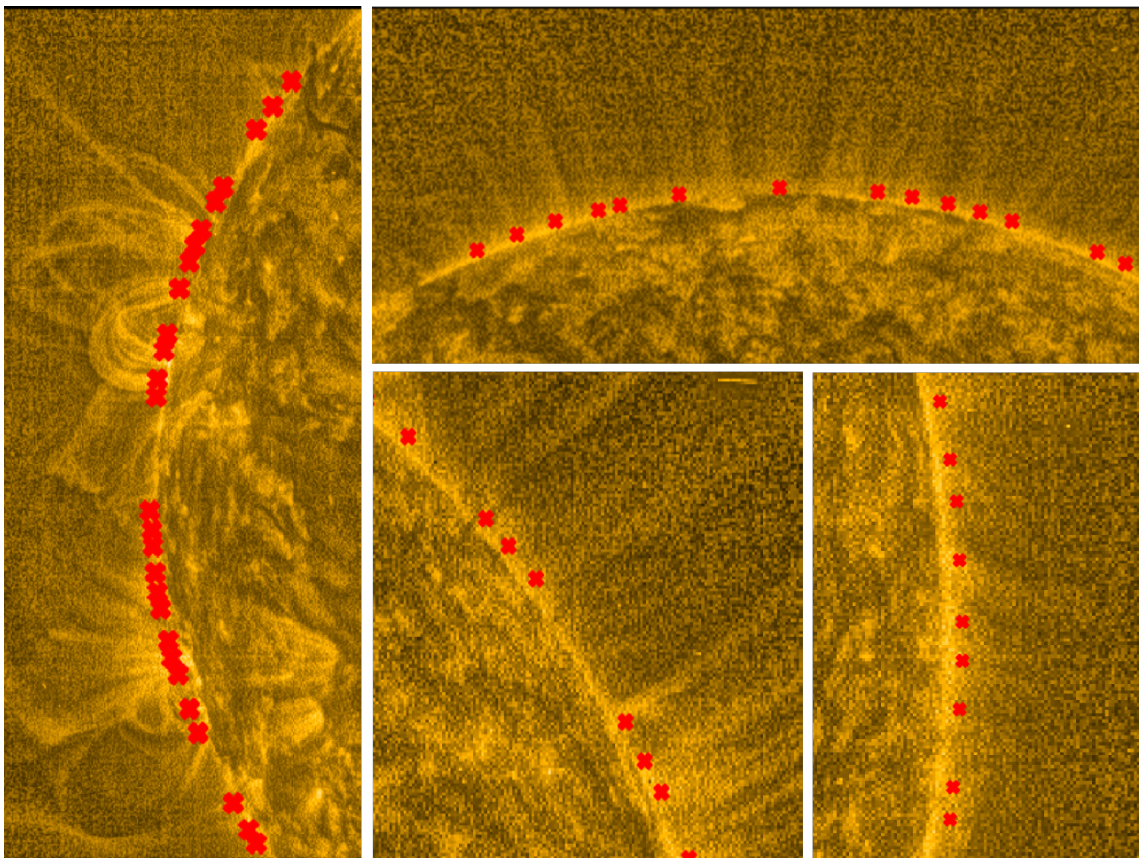

Figure 7.5: Whole region and close up of 171 Åimages showing local prominences (red crosses) displayed on top of their corresponding physical structures. Not all crosses correspond to structures visible, and not all structures have a corresponding cross.

Though this method is has limitations, it should be capable of creating a crude proxy for examining the colatitude distribution of structures overall. Consequently, most of the an annulus is disregarded, and the innermost strip (three pixels, roughly 0.003 solar radii) is normalized with respect to pixel intensity, and points greater than 0.5 are chosen as points to be tracked (as values less than this result in spurious detections in brighter regions, and values greater than this omit legimiate structures

in dimmer regions). Additionally, a minimum spacing between points (10 pixels) prevents oversaturated regions from being over represented in the resulting distribution without sacrificing too many potential structures in brighter regions. However, this may have the effect of excluding legitimate and distinct structures that are tightly packed together. These choices represent a compromise between ensuring that different regions of the limb have detected structures, and minimising the number of spurious detections, which is necessary for the results to be statistically valid.

These points are compiled into a histogram of occurrence frequency versus co-latitude, similarly to those seen in Chapters 5 and 6. phases of Rise, Peak, and Decay are defined in Cycle 23 by the same criteria they are defined in Cycle 24; namely rise being the phase between the start of sunspot activity at the beginning of the cycle (or the earliest available data) and the first maximum in total sunspot activity; Peak being the phase between the first observed maximum and the last local maximum before sustained activity decline is recorded; and Decay being the phase between the last local maximum of the peak phase and the end of the cycle where activity drops to near zero. Of these three phases, decay marks the longest time phase.

These collected local prominences will be analysed in three different ways. Firstly, their entire distribution, from the north to the south poles, which was not previously attempted in previous AIA studies.

Secondly, they will be analysed within the polar regions and examined for evidence of a persistent boundary somewhere between the open polar regions examined in Chapter 6 and the closed active regions studied in Chapter 5. Evidence of this would provide information as to how the polar region topology and it's interface with the active region varies and evolves across a longer twenty two year solar cycle.

Thirdly, they will be analysed between the same range as initial analyses of active regions in cycle 24 using AIA data. This will demonstrate whether the same

prevailing distribution of structures in different EUV regimes is seen in cycle 23 as in cycle 24, or whether the shift between which prevailing hemisphere of magnetic polarity dominates overall will also change the location and evolution of these interacting active regions.

Given the decrease in spatial resolution from AIA to EIT, as well as the constant and irregular degradation of the CCD throughout cycle 23, the exact position of local prominences should be considered approximate for the general location of brightly emitting structures at a specific height of the corona. As these points are based on a normalized intensity index, each frame will produce potential points, therefore, it is the relative distribution of these points and not simply the number which is important to analyses of the changing coronal structure.

7.3 Results

In total, 128,377 local prominences were recorded for 171 Å, 114,776 for 195 Å, 76,275 for 284 Åand 33,444 for 304 Å. These numbers far exceed those of confirmed structures seen in AIA studies. These local prominences were captured between 0 and 180 degrees of colatitude displacement from the North Pole in each frame, approximately three days apart from each other except in cases when frames were unavailable for extended phases of time owing to database continuity issues or instrument dropout due to calibration or dark frame records. The relationship between the colatitude and occurence frequency is shown in Figure 7.6. These numbers are also summarized in Table 7.1

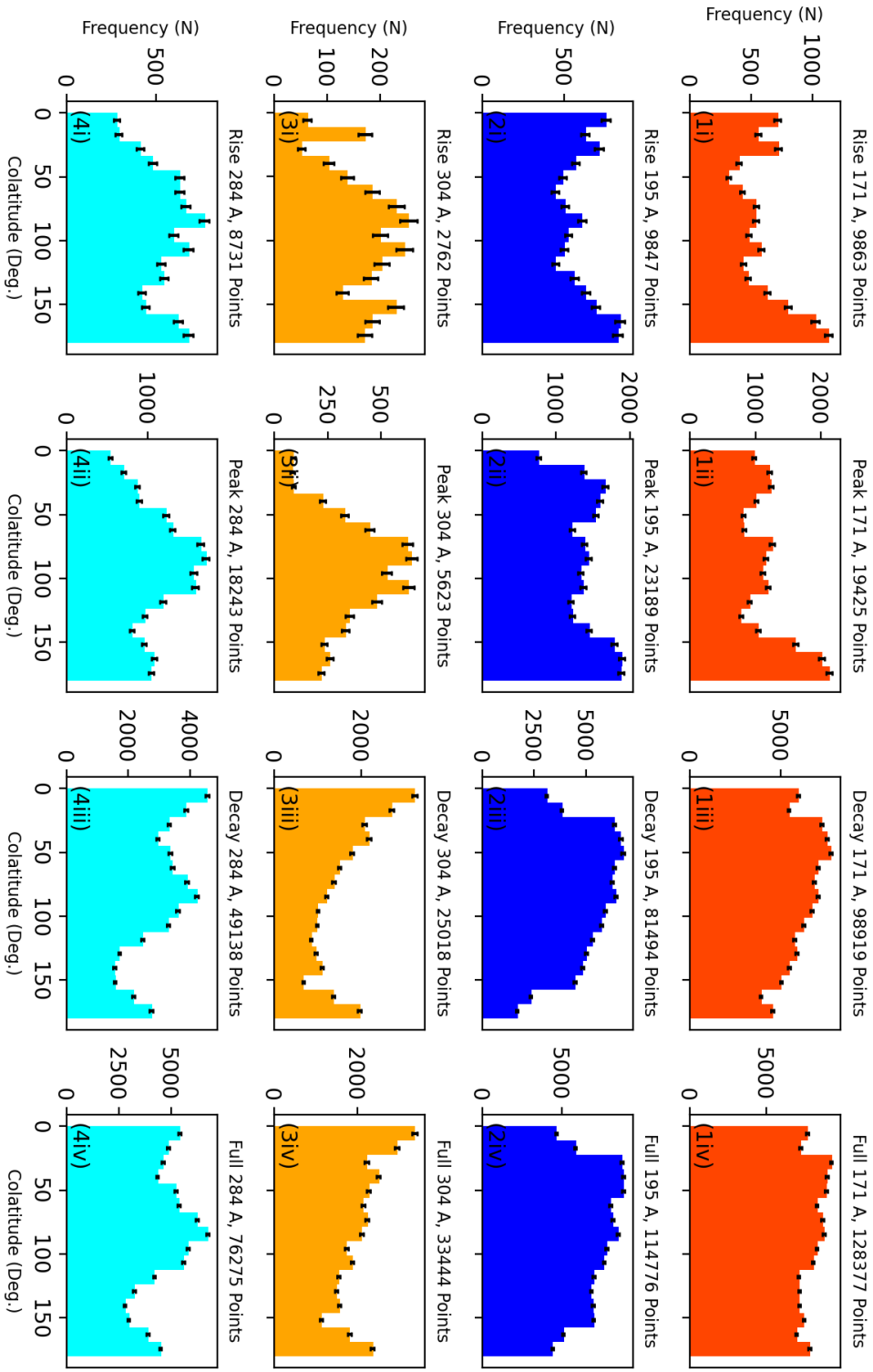

Figure 7.6: Diagram of colatitude frequency (y axis) versus colatitude (x axis) for local prominences in across all colatitude ranges by time phase (Rise, Peak, Decay, Total) and wavelength (171, 195, 304, 284 Å) respectively. $\sqrt{N}$ error indicated by error bars.

Table 7.1: Full Range EIT local prominence structure frequency by wavelength and phase.

Wavelength (A)	Rise	Peak	Decay	Total
171	18960	25099	84186	128377
195	19906	27185	67488	114776
284	16209	21162	38748	76275
304	5471	8091	19824	33444

The relationship shown in each wavelength differs during the rise phase (18960 points) 171 Åshowing a distribution which favors the polar colatitude (in particular the southern pole), becoming more evenly distributed in the peak phase (25099 points), and demonstrating a distribution which favors the more equatorial active region in the decay phase (84186 points).This relationship is largely mirrored in 195 Å, with a slightly less pronounced but similarly shaped distribution in the rise phase (19906 points), but with similar distributions in the peak (27185 points) and decay (67488 points) phase, as seen in the 171 Åcase. For 304 Å, the least populated group, the distribution in the rise phase (5471 points), peak phase (8091 points) and decay phase (19824 points) diverges from the 171 Åand 195 Ådistribution. These local prominences fall predominantly in regions excluded by these two populations, displaying a preference for the equatorial region during the rise phase, and distributed predominantly away from the active region in the decay phase. Similar to 304 Å, 284 Åshows a distribution of southern leading equatorial preference in the rise phase (16209 points), a northern leading equatorial preference in the peak phase (21162 points), but diverges from 304 in the Decay phase (38745 points) by generally retaining it's distribution from the peak phase, showing only a slight increase in amplitude in the polar regions.

Differences in local conditions that the features are within and the difference between open and closed structures and open structures necessitate a more limited

evaluation in specific ranges, such as how the predominantly closed active region (Chapter 5) and open polar regions (Chapter 6) were analysed individually. The results of these analyses can be seen in Figures 7.7 and 7.8, demonstrating the results of active region and polar analyses respectively.

7.3.1 Closed Region

In the closed region analysis, the distributions appear to be more flat than those seen in the AIA regions, with less pronounced distribution profiles compared to earlier study (see Figure 5.9) The results of this analysis for closed regions is demonstrated in Figure 7.7 and Table 7.2.

Table 7.2: Active Region EIT local prominence structure frequency by wavelength and phase.

Wavelength (A)	Rise	Peak	Decay	Total
171	2760	5963	35343	44122
195	2735	7146	32233	42193
284	3505	8256	19198	31034
304	1202	3069	6171	10466

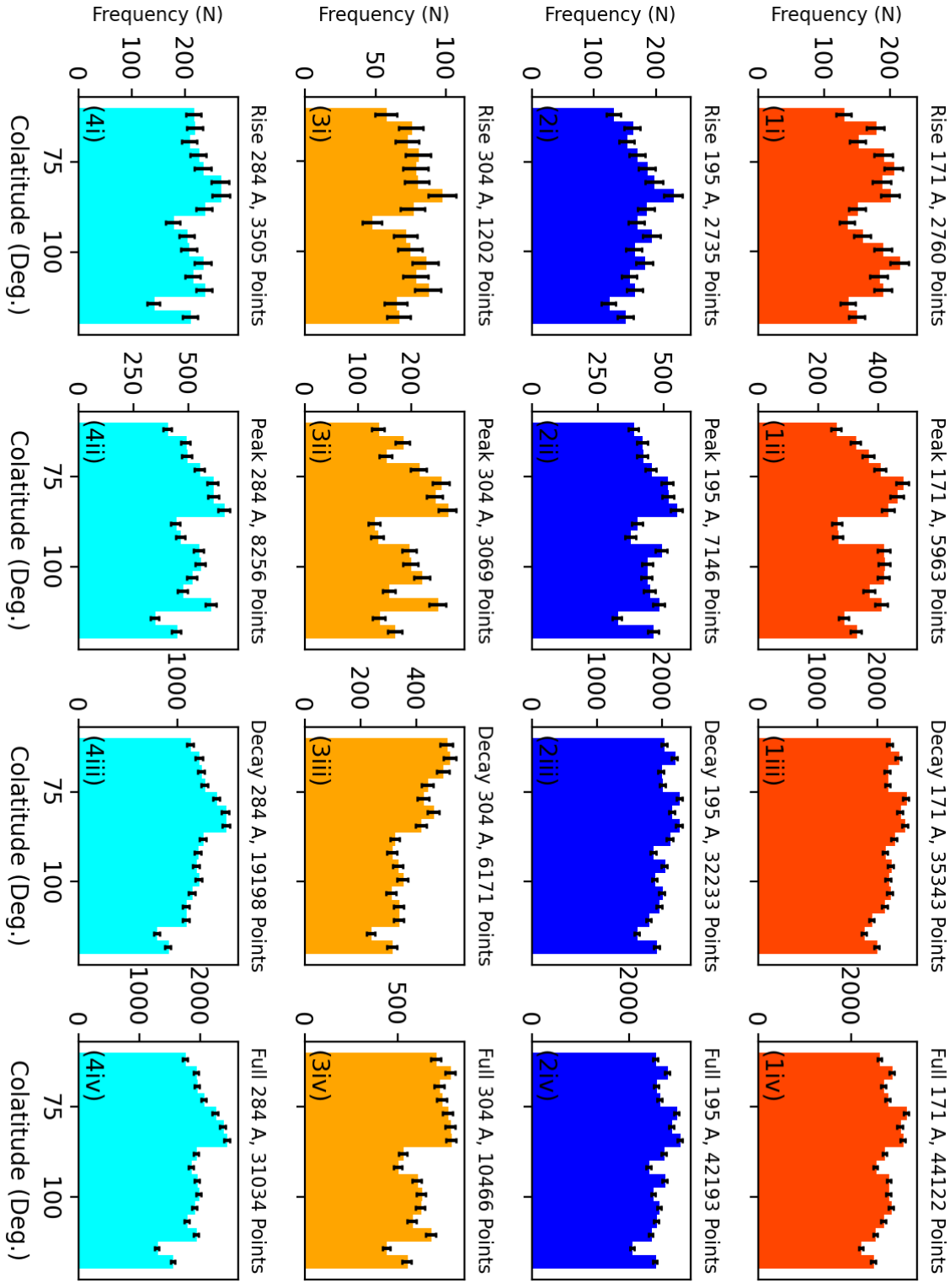

Figure 7.7: Diagram of colatitude frequency (y axis) versus colatitude (x axis) for local prominences in the equatorial active regions by time phase (Rise, Peak, Decay, Total) and wavelength (171, 195, 304, 284) respectively. $\sqrt{N}$ error indicated by error bars.

The 171 Åwavelength points demonstrated the exclusion of detections near the equator best in rise (2760 points) and peak (5963 points), but decay (35343 points) was predominantly flat with a very minor degree of hemispheric preference, and little visible preference or exclusion by colatitude. This lack of consistent profile is also seen in 195 Å, which maintains relatively flat distributions in rise (2735 points), peak (7146 points), and decay (32233 points). 304 Åhas profiles which appear similar to the slightly bifurcated distributions of 171 Åin rise (1202 points) and peak (3069 points) phases, but a distribution which heavily favors the northern hemisphere in the decay (6171 points). 284 Ådisplays profiles similar to 195 and 304 Åin the rise (3505 points) and peak (8256 points) phase, but with a profile which appears distinct from any other wavelength in the decay phase (31034 points), a distribution favoring the northern hemisphere active region.

7.3.2 Open/Polar Region

In polar region analysis, distributions show varying degrees of similarity to equivalent wavelengths in the AIA distribution, shown in Table 7.3 and Figure 7.8.

Table 7.3: Polar local prominence frequency by wavelength and hemisphere.

Wavelength (Å)	North	South	Total
171	21043	19710	40753
195	16218	13924	30142
284	13521	10350	23871
304	7877	4957	12834

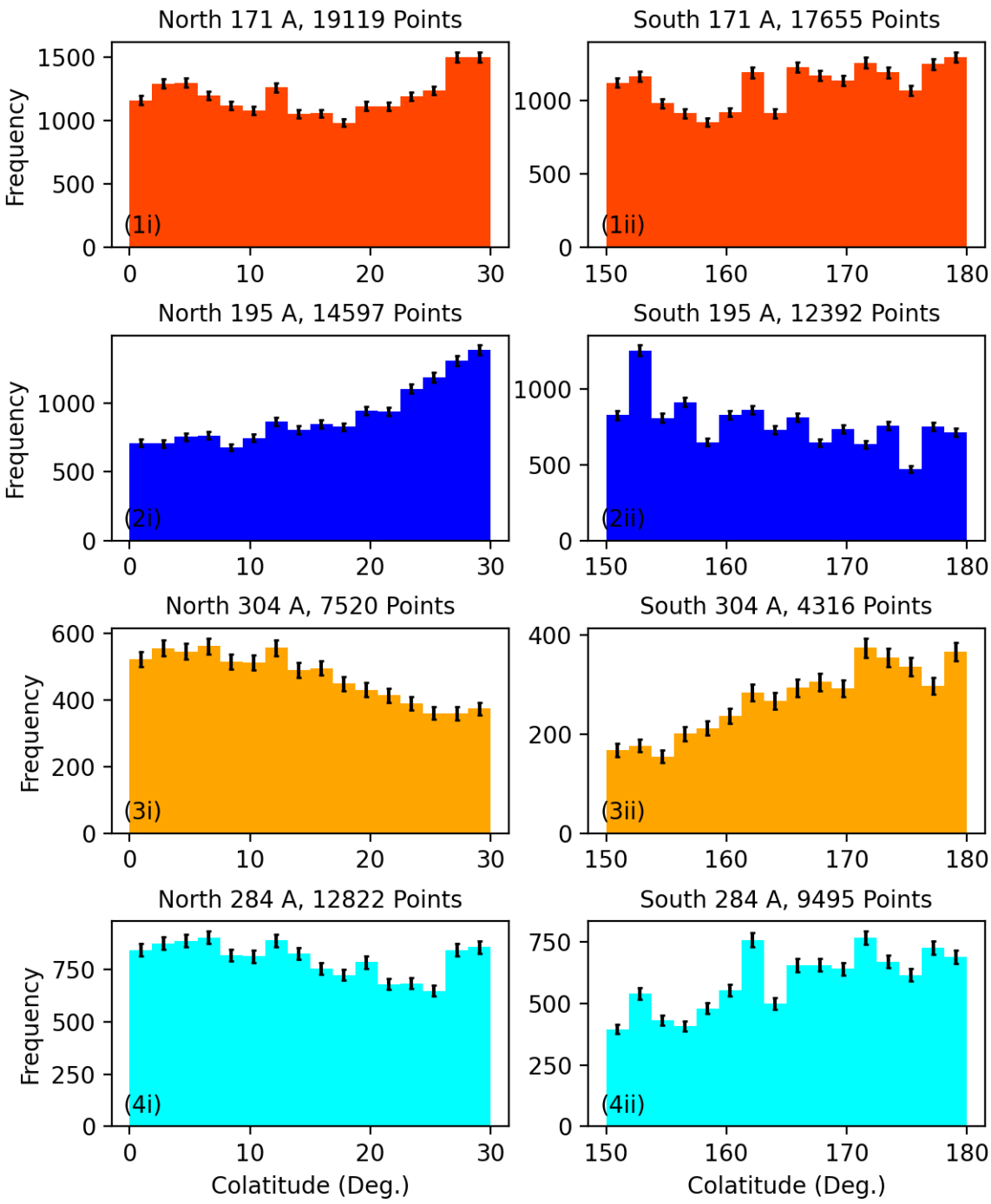

Figure 7.8: Diagram of colatitude frequency distribution for local prominences in Solar Cycle 23. Frequency (y axis) of structures by colatitude (x axis) arranged in descending order (171, 195, 304, and 284 Å). $\sqrt{N}$ error indicated by error bars.

171 Å local prominences shows a slight preference towards the edge of the polar regions, with more points appearing towards maximal displacement from the middle of the polar regions (30 degrees away from poles). The North (21043 points) is more pronounced in this, and shows clearer exclusion from the center of the region than the South (19710 points).

The **195 Å** distribution shows a profile with preference towards the edge of the distribution. This profile is more distinct in the North (16218 points), and indicates an less potential structure in the region directly above the north pole. This trend is more exaggerated, but less well populated in the South (13924 points). This distribution is different from that seen in the 193 Åband in the AIA plume structures (see Figure 6.6), which displayed a flatter profile which showed a greater proportion of structure away from the equator.

The **284 Å** distributions appear similar to those in the 304 Åpopulation, though these distributions are less well defined despite being more well populated in the North (13521 points) and the South (10350 points).

The **304 Å** population displays a profile which favors the poles, again dissimilar from that seen in plumes in AIA. This profile is more pronounced in the South (4957 points) than the North (7877 points).

7.4 Discussion

The analysis of distribution of local prominences using EIT data must be considered with the following details. Firstly, local prominences are a cruder metric of coronal magnetic activity than structures which have satisfied the criteria for measurement of closed/open structures and which fall within the range of 2.7 - 5 AIA pixel widths.

This means that the number of points, while statistically more significant than the number of structures, are potentially a less reliable indicator of overall structure within the corona than confirmed structure segments traced within an annulus.

A consequence of this process is that the normalization within each image causes a greater number of points than structures to be detected, but that these points are based on normalization within each image only. A consequence of this is that detected activity is more weighted towards the number of frames within each phase instead of exclusively the amount of structures present than would be the case for AIA structure based detections. This can be seen in the number of local prominences within the decay phase compared to the rise and peak phases where most activity is expected to be present, such as for 171 Å(84186 points in the decay out of a total 128377). As previously mentioned, the shape of the distributions should still be informative of overall coronal trends, and not merely the number of detections within these phases.

Also, the relative number of structures in each hemisphere will be affected. Solar Cycle 23, as seen in the number of sunspots by hemisphere (see Figure 7.1) is lead by the Southern hemisphere, though the numbers of points in the northern hemisphere is greater than the south (21043 N vs 19710 S in 171, 16218 N vs 13924 S in 193 Å). One possibility for this is the greater numbers of polar local prominences as a proportion of the population compared to the total population (active region points included) 44122 active region points versus 40753 polar points for 171 Å. This compares to 3501 171 Åplumes (see Figure 6.6) versus 17430 171 Åactive region loops in Solar Cycle 24, showing that the relative numbers of structure in these regions are not preserved by local prominence analysis. By weighting towards the polar regions, the activity of the solar cycle could appear inverted, as the number of plumes appearing in the northern hemisphere could be relatively higher than those appearing in the southern hemisphere.

Despite these considerations, some overall trends can still be analysed in these time phases for Solar Cycle 23. Though width profiles could not be constructed for structures using EIT data, analyses of local prominences in both the closed

equatorial active regions and the open polar regions can be compared to profiles gathered from structures in cycle 24 to create characteristic descriptions of colatitude occurrence profiles for the corona throughout the solar cycle. For example, three distinct profiles emerge from the equatorial active region analyses.

The first is the bifurcated distribution, where local prominences are less pronounced in the regions surrounding the equator. This is most clearly seen in the rise and peak of 171 Å(Figure 7.71i and 7.71ii), phases of high activity where the normalization based approach of the local prominence detection method works most effectively. This distribution is closest to those seen in the equatorial active regions, which mirror observations of sunspots following the butterfly distribution of Spörer's Law.

In decay, and other wavelengths such as 193, a flat distribution is seen. This flat distribution may represent a constant level of "noise" introduced by the local prominence method which does not correspond exclusively to the presence of structure. Other distributions (such as Figure 7.7 4ii) could be combinations of the bifurcated distribution (split into two hemispheres) and some constant noise. The distribution of 304 Åin decay (Figure7.7 3ii) displays a predisposition towards the northern edge of the active region (60 degrees from the northern pole). As 304 Åis the least populated distribution, and the relative scarcity of 304 emission at this height above the limb, the distribution may have been dominated by a relatively small number of events in the decay phase.

In the polar regions (Figure 7.8, distributions present more contrast to polar region profiles as described earlier (see chapter 6). The three distributions seen in this region are predominantly flat distributions as seen in 171 Å, with a slight predisposition towards the pole and the edge of the polar region. This is inconsistent with observations of the AIA 171 Åpolar plumes, which show a clear preference towards the lines-of-sight intersecting the greatest surface area of the coronal hole. 195

Ålocal prominences show a clear preference for the edges of the coronal hole in both hemispheres, a distribution which is not present in AIA 193 Åplume populations, which display a profile similar to the EIT 171 Ålocal prominences. Both 304 Åand 285 Ådisplay a profile which appears to be combination of the asymptotic distributions seen in AIA plume populations such as 171 and 193 Åand some background noise. These distributions are noteworthy, in that they demonstrate a dissimilarity between the position of local prominences and magnetic structures seen in AIA.

7.5 Conclusion

In conclusion, the distributions of coronal local prominences can provide some estimate of coronal activity throughout Solar Cycle 23, but do not represent parameters as significant or as clearly defined as those used in Cycle 24. Further work may be required to draw details of spatial and structural evolution of coronal magnetic structures throughout this phase, but distributions such as those seen in the more active phases (Rise and Peak) of the most spectrally well defined wavelength (171 Å) agree with some distributions seen in cycle 24, indicating that a characteristic description of coronal structure might exist. Other distributions involve either an asymptotic distribution of polar regions, or some combination of the two depending on the specific geometries of the polar coronal hole. The inverse relationship between observed plume structures and the overall polarity of the solar magnetic field is similarly observed to continue in cycle 23, though little can be said about the likely structural details in this phase, which would be of greater importance in describing conditions within the regions which formed structures relevant to studies of coronal field morphology. More work is required to properly analyse cycle 23 for whatever detail can be extracted and used for coronal analysis.

Chapter 8

Summary, Discussion, and Future Work

8.1 Summary

The research outlined in this thesis currently represents the largest analysis on structures within the corona, with results gathered from across twenty two years and two solar cycles, from data gathered from two generations of space based solar observatories collecting six EUV wavelengths of light in temperatures ranging from 50,000 to 2,000,000 K. The data has been used to isolate and analyse trends in structural topologies from across the Active and Polar regions, and studied within the context of theoretical models of width distributions and understandings of hemispheric asymmetry. These results will be discussed in greater detail in the following subsections.

8.2 SOC and the Corona

The theory of SOC applying to the magnetic structures which comprise the solar corona is detailed in Chapter 3 and is summarised as follows; Stochastic processes

add energy to the footpoints of coronal structures by helical magnetic tension or footpoint motion (or a combination of both), and the effect of that addition on generating criticality within strands is a non-linear, dynamically driven cascade of magnetic reconnection events across all available scale lengths within the formation region. In the corona, this process is analogous to direct current or DC heating. To better analyse whether the phenomena of coronal structures were predominantly governed by this process, a study of coronal widths was made in both active region and plume structures, as these represent different conditions of the solar atmosphere. From these studies of loop widths across solar cycle 24, a clear tendency for loop widths to display a power law profile is observed, the slope of the power law which converges to but does not meet the expected value of -1.5. The values of α_w populations of different active regions range from -1.6 to -2.0 in 171 Å, -1.8 to -2.2 in 193 Å, -2.6 to -3.3 in 211 Å, and -3.2 to -5.5 in 304 Å(though this was an underpopulated range). If these slope values are taken to be a measure of similarity (or dissimilarity) to the model prediction, then the variance of the power law slope of width populations in differing wavelengths must be explained.

If active region structures are predominantly isothermal, then the differing power law slopes could indicate that parameters of the formation regions analogous to a theoretical SOC space are being changed. If parameters such as the level of "quenching" ie; the difficulty for cascades to pass throughout the available space or the local critical threshold is of higher or lower importance to the formation of structures observable in hotter lines (like 211 Å), then this would be reflected in steeper slopes in the width populations, as smaller scale events become more frequent and larger scale events are less likely to occur. Additionally, as these conditions change throughout the solar cycle, the slopes are likely to be affected as the magnitude of magnetic flux within these regions also changes.

There are also variations between polar structures which are topologically open

and active region structures which are primarily topologically closed. 171 Åpolar structures are recorded with slopes between -2.2 to -3.4, 193 Åslopes between -3.1 and -3.3. Average slopes in 211 Åand 304 Åare -4.7 and -2.4 respectively, but the distributions of these wavelengths are underpopulated and the range of these values is unlikely to indicate a statistically significant variation. There exists a noticeable difference between open plume widths in the polar region and closed coronal loops in the active region colatitudes, namely that polar plume widths almost universally possess a steeper power law slopes than populations in the active region colatitudes. This indicates that wider polar structures are proportionally less frequent than wide active region structures. This could be due to observational effects, such as differing backgrounds within these regions, but could also indicate a difference in the physical properties of the footpoint regions which manifests as lower amounts of cascading of events or a higher local critical threshold in the SOC space.

Though these results indicate that coronal structures do indeed appear to follow the principles of SOC, at least in the active region colatitudes, and that measurable differences between these power laws can be seen across temperature regimes and throughout different time periods, there are a number of questions which remain to be answered before it can be said with confidence that SOC can describe the occurrence of coronal structures accurately. Firstly, are deviations of observed power law slopes from the ideal -1.5 prediction caused primarily by observational limitations that threshold smaller scale widths, or by real physical variation from the SOC principle? Because the SOC based assumptions are not informed by specific physical processes, it should not be expected that the observed power law slopes are exactly -1.5, so a value such as -1.6 may be considered to be "close enough" that only a small degree of variation can account for this discrepancy. Other populations possess much steeper slopes, however, and the question of whether a slope of -3.1 can be considered an indicator of SOC is unclear. Ultimately, this work represents

a first step in being able to utilize the large scale statistical trends of select coronal statistics (such as coronal structure widths) to highlight and bring attention to trends and relationships which may be impossible to determine with small datasets based on a limited selection in both time and space. The ability of SOC based analysis to track physical variation across particular regions of the solar photosphere and corona over time represents an opportunity for large statistically based surveys of coronal geometries to contribute to understanding of the creation and behaviour of these structures, and developments of this technique may lead to discoveries of physical processes within the corona and improvements to parameters which inform modelling efforts.

8.3 Hemispheric Asymmetry

Analysis of solar hemispheric asymmetry as defined in Chapter 5 has been important for studies of outwards moving/transferring phenomena such as the solar wind and coronal mass ejections, as well as studies of internal mechanisms of the solar dynamo and the consequences of an imbalanced solar magnetic field. Asymmetry has been most commonly studied in sunspot frequency and umbral area coverage, but other indicators such as solar wind speed and coronal hole morphology are also frequently studied and related to this variability in the dynamo and how it threads through different regions and altitudes of the solar atmosphere. This work represents the first survey of coronal structures above the limb for asymmetry, and includes positional data of the occurrence of coronal structures in both the active and polar regions in Solar Cycle 24, as well as a combined study of local annular brightenings at a set altitude (see Chapter 7) throughout Solar Cycle 23. Results indicate the consistent presence of a distinct hemispheric asymmetry, comprising of coronal activity within a hemisphere which slowly approaches its maximum value and declines more rapidly, and a hemipshere in which activity quickly arrives to peak intensity and declines

more gradually. The hemisphere in which the more gradual change occurs seems to align with the overall polarity of the hemisphere throughout the solar cycle, and was southern in Solar Cycle 23, and northern in Solar Cycle 24.

Results have indicated the presence of a nuanced and multiprofiled solar cycle, with two distinct modes of activity occurring in each hemisphere. Latitude frequencies indicate that structures within the rise and decay phases predominantly occur within one hemisphere, seen in the first peak of solar cycle activity, whilst the second peak of solar activity occurs due to activity occurring in the other hemisphere. The decay phase activity appears to be lead by the dominant hemisphere, as this hemisphere decays more slowly, despite peaking potentially years before the second hemisphere (see Figures 3.1 and 7.1 for cycle 24 and 23 respectively). This asymmetry in activity is pronounced in closed equatorial regions (between 45-55 % predominance in leading hemisphere activity in all periods) compared to open polar regions (average of 65 % predominance in leading hemisphere throughout Solar Cycle 24).

Additionally, colatitude distributions highlight the variation in structures between open polar regions and closed equatorial regions. Distributions of structures and annular bright points within active region colatitudes show a general lack of stratification between wavelengths and time periods, except for those that would be expected due to underlying shifts in the position of sunspots (eg, Spörer's Law migration towards the equator). Structures in the open polar regions conversely show clear evidence of a stratification, with 171 Å, 193, and 211 Åstructures frequencies all varying by colatitude (see Figures 6.3 and 6.4). This stratification appears to correspond with the optical line-of-sight and may also indicate a preference towards the boundaries of the coronal hole and the region between open and closed magnetic flux for hotter lines (193, 211 Å). More work is required to explore whether these distributions could be used to probe the qualities of coronal holes, as well as extract

information from structures with footpoints on the far side of the solar polar regions.

8.4 Future Work

8.4.1 Optimisation and Development of Technique

Future development of these techniques can be broken down broadly into three overall categories. Firstly, efforts to reduce the ambiguity and arbitrary choices involved in the process could be introduced. When determining an algorithmic approach and assembling a data pipeline to allow for the collection of statistics and subsequent analysis of data from a raw image, a number of decisions must be made, which must ultimately involve an element of arbitrary choice. Examples of where bias might be introduced through these choices are the application of image filters, how optimal geometries are selected and traced, and the threshold of these variables that determine successful and unsuccessful detections.

Parameters may in future be determined by testing of the data being used instead, such as by determining local brightness intensities within the annulus for a given wavelength population and tailoring appropriate cutoff points, kernel sizes or layer weighting during image processing and subsequent enhancements for differing wavelengths.

Secondly, it may be possible to improve the performance of techniques and the efficiency of the algorithm. For example, mechanisms for determining ideal geometries might be revised, and a range of different types of geometric fitting such as cubic, spline fitting, or combinations of linear segments may be used instead of curvilinear segments. Additionally, the annulus height may be changed for differing wavelengths, depending on which wavelength and temperature regime is best represented at which altitude. The 304 Åresults will be of particular interest to improve, as the upcoming EUI instrument of the Solar Orbiter (see Section 8.4) will only have

two high resolution EUV instruments, in 174 A and 304 Å. As these will be the only wavelengths with an exact match to existing instruments, this could potentially be a promising avenue for comparison of events captured simultaneously with both the AIA and Solar Orbiter.

Thirdly, to gather more parameters of interest that could enhance the research of coronal structures, such as tracing structures out to higher altitudes using multiple nesting annuli to determine the height of structures, and to then compare average widths within these annuli to one another to examine for expansion with height, or to compare the relative intensity of the averages of the cross sections in different wavelengths as a probe of multi versus isothermal emission of structures in the corona. Additionally, expansion could be examined by recording cross sections separately, and determining if these profiles become wider and by how much.

Additionally, the Heliophysics Event Knowledgebase (HEK) (Hurlburt et al., 2012) could be used to correlate structures detected with other recorded phenomena such as sunspots, coronal hole positions, active regions, locations of emerging flux, filament activation, and other indicators of solar activity. This would allow a more precise analysis of coronal structure location in comparison to other parameters in time as well as location.

The AIA, whilst still operation and providing high quality science data, has experienced inevitable degradation of imaging CCDs as a result of long term exposure to conditions in orbit and direct sunlight, a phenomenon known to affect all EUV instruments (BenMoussa et al., 2013). In the AIA, this manifests as reduced spectral efficiency and increased point spread function, resulting in dimmer and less focused images (Dos Santos et al., 2021). This effect has not been controlled for in this work, but future studies using AIA data could be improved by implementing a level 1.6 correction, which deconvovles the psf from each pixel of the image. This has not been attempted in this work as it was considered too computationally expensive,

but improving computational resources and GPU based image processing may allow work to be performed using cleaner and higher quality image data.

8.4.2 Machine Learning

Machine Learning is a burgeoning field in scientific and specifically astronomical and solar physics based research. Its uses have been speculated upon for some time (Shih et al., 2008), and there are many ways in which an automated survey of data might be enhanced by the addition of machine learning elements. As the functionality and applicability of machine learning is diverse, there are a wide range of possibilities for incorporation into the project.

Though there are many different ways in which machine learning might be utilized in continuations of this work, there are several ways in which it is likely to be more practical. In terms of identification and tracking, deep learning machine learning models have been used in pattern recognition for a number of structures, either in multiple capacities ie, identifying more than one structure or indicator (Armstrong & Fletcher, 2019), or in more specialized roles such as identifying Solar Energetic Particle events (SEP's) (Lavasa et al., 2021). They can also be used in predictions of other paramaters, which can be time consuming or unreliable by other methods such as polarimetric inversions of spectral data (Asensio Ramos & Díaz Baso, 2019).

One use of machine learning which has been investigated for implementation in this project is in de-noising of image data either at the level 1 or post MGN stage, as demonstrated by the Noise2Noise method (Lehtinen et al., 2018). In this method a deconvolution of a "ground" truth from many noisy images can be created, assuming that the pattern of noise itself is some kind of randomly added noise such as would be the case in noise patterns generated by MGN. An advantage of this method which makes it suitable for use in astrophysical settings is that no "clean" ground image

is needed to compare for training purposes, and training images do not need to be of the same type as images that are to be cleaned, just that they contain the same type of noise. As AIA has a short time cadence, millions of unique training images can be created by applying the MGN (or other similar data processing techniques), which is likely to increase the reliability and quality of resulting cleaned images. In this work, this machine learning method would likely replace the cruder time averaging MGN method as a means of reducing the impact of noise on resulting images. This could lead to cleaner images, in turn leading to more reliable geometry fitting/tracing and higher quality results.

8.4.3 Solar Cycle 25

The exact nature of Solar Cycle 25 is yet to be determined, but indications are that the early rise phase of Cycle 25 is greater than that of Solar Cycle 24. Given the current, active instrumentation represents the most advanced imaging procedures ever utilized for solar physics research, there are a wealth of opportunities for examination of structures and dynamism as the cycle progresses. Future work will require proper utilization of all available datasets and instruments, including continued coverage of Cycle 25 with SDO, as well as new data made available through the Solar Orbiter mission (Müller et al., 2020a).

Launched in February 2020, Solar Orbiter is a joint ESA and NASA multi-instrument satellite with a total of ten remote and in situ instruments capable of measuring a diverse array of data and capturing the solar atmosphere from a wide variety of vantage points and one evolving orbit, with the aim of providing better insight into the mechanisms of propagation of the Heliosphere (García Marirrodriga et al., 2021; Müller et al., 2013). Of particular interest to future studies of the corona is the Extreme Ultraviolet Imager (EUI) instrument (Rochus et al., 2020) that utilizes a combination of EUV and Lyman-Alpha channels and contains three

imagers. These three imagers cover the 174 Åand 304 Åwavelength bands, with two close field High Resolution Imagers (HRI) in 174 Åand 304 Å, and one synoptic imager in 174 A. These HRI have a pixel coveage of 2048 x 2048, with the Full Sun Imager(FSI) possessing a pixel resolution of 3072 x 3072. Due to the varying orbital radius of the Solar Orbiter, and the irregular orientation and mission requirements as well as limited telemetry, this data will not be as regular or as long running as from SDO. However, this represents an opportunity to view certain fields-of-view in much greater detail, obtaining results comparable to the Hi-C missions. Additionally, these results can occasionally be compared to AIA images captured at the same time, producing a stereoscopic picture of events, albeit in different resolutions.

Other instruments which could be helpful for analysis of the corona within Solar Cycle 25 is the Geostationary Operational Environmental Satellites (GOES) 16 (formerly R) satellite, which contains both Earth and Sun facing satellites, observing both terrestrial and space weather. This satellite contains a suite of remote sensing and in-situ instruments to document space weather. Among these is the Solar Ultra-Violet Imager (SUVI) (Darnel et al., 2022), capable of performing synoptic imaging of the Sun in 171, 195, 284, and 304 Åwith a spatial resolution of 2.5 arcsecs per pixel in a field of 1240 x 1240 pixels, representing an improvement over the 5 arcsecs per pixel resolution of the previous GOES 15 X-ray detector. This synoptic coverage over Solar Cycle 25 and similarity to EIT would allow for similar methodology to be employed on an ongoing basis.

8.4.4 Improving Legacy Data Analysis

Chapter 7 detailed attempts to extract positional data of coronal structures in Solar Cycle 23 using EIT data in the 171, 195, 284, and 304 Åfilters. Though this effort was successful in determining some trends of coronal atmospheric distributions across

Solar Cycle 23, it was limited in some regards. The quality of the data seemed to be affected by a constant level of "noise" which overlaid any observable pattern in the distribution of coronal bright points. This is reflected in the very high number of detections, with 352,872 annular bright points in total, with 128,377 in 171 Åalone. Though it is possible to show hints at more detailed distributions like those seen in Chapter 5 and 6, this level of "background" makes clear trends difficult to discern and confidently analyse. Were the techniques used within Chapter 7 developed further, such as by a more detailed bright point analysis in nested layers or by machine learning reproductions of coronal structures using SDO and SOHO data, and these points refined to better reflect distributions of coronal structure within Solar Cycle 23 and the EIT dataset, more confident analyses of longer term trends could be made.

Additionally, a study of the periods during which coverage of the Sun is captured by both the SDO and the SOHO instruments would allow a detailed comparison of structures imaged in both. The bright point technique developed to analyse the EIT could be compared to the structural identification and tracing technique. This would allow for an estimation of how closely those local prominences match to traceable coronal structures.

Synthetic data, including those made by machine aearning algorithms can allow for improvement and development of automated detection algorithms, as the input parameters of loop position and width can be compared to the output of the algorithm to determine

Appendices

CHAPTER

.1 Code and Results

These are shortened links to a github repo where code and results utilized for analysis in various chapters are held.

.1.1 AIA Active Region Cycle 24

Code

Chapter 5 Code - https://tinyurl.com/COSDALoops

Results

Chapter 5 Results - https://tinyurl.com/LoopsResults

.1.2 AIA Polar Region Cycle 24 Code

Code:

Chapter 6 Code - https://tinyurl.com/COSDAPlumes

Results:

Chapter 6 Results - https://tinyurl.com/PlumesResults

.1.3 EIT Full Limb Cycle 23 Code

Code:

Chapter 7 Code - https://tinyurl.com/COSDAEIT

Results:

Chapter 7 Results - https://tinyurl.com/EITResults

CHAPTER

.1.4 Geometry Tracing Diagram

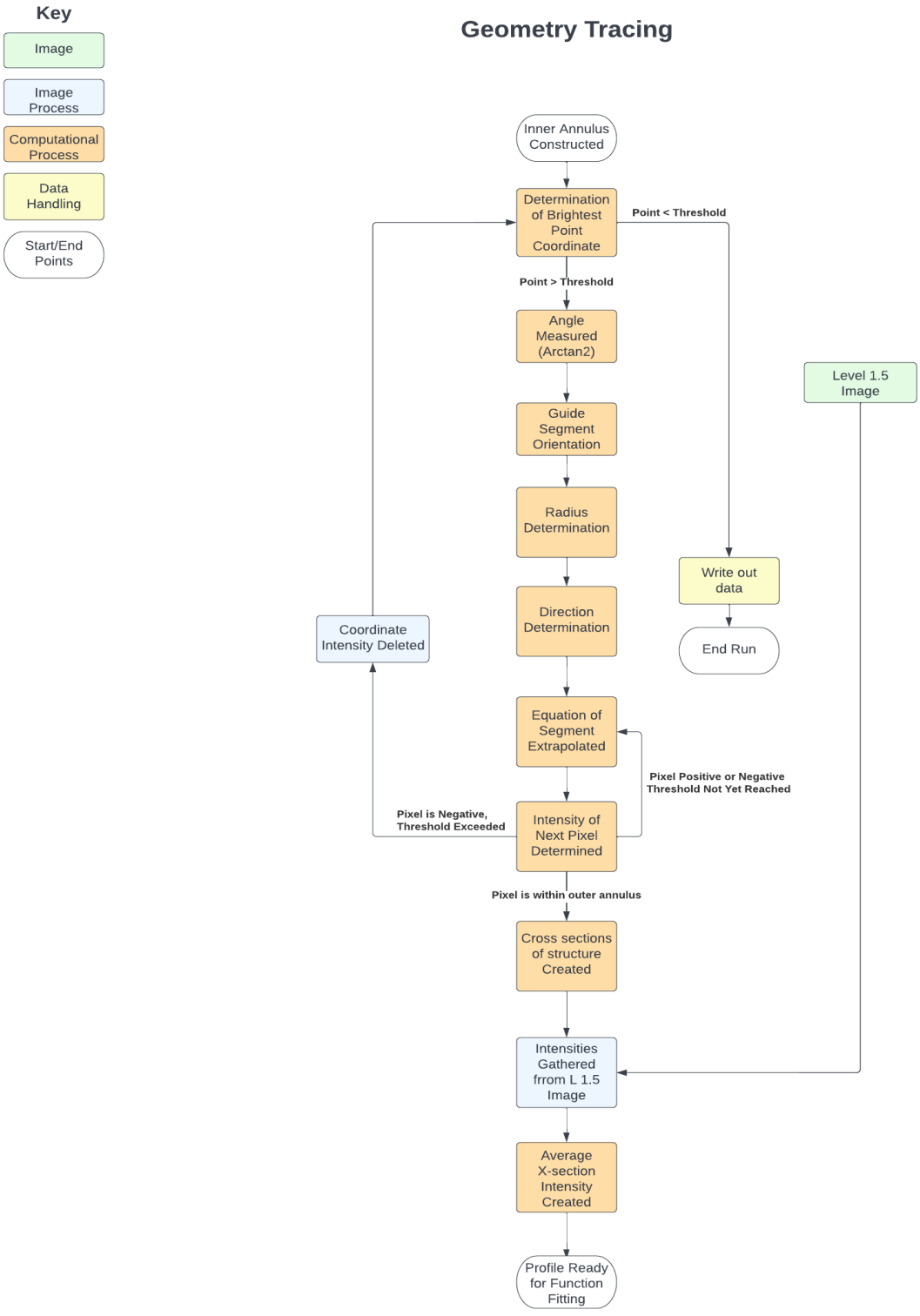

Figure 1: Workflow diagram of the Geometry Tracing element of the COSDA algorithm.

.1.5 Width Fitting Diagram

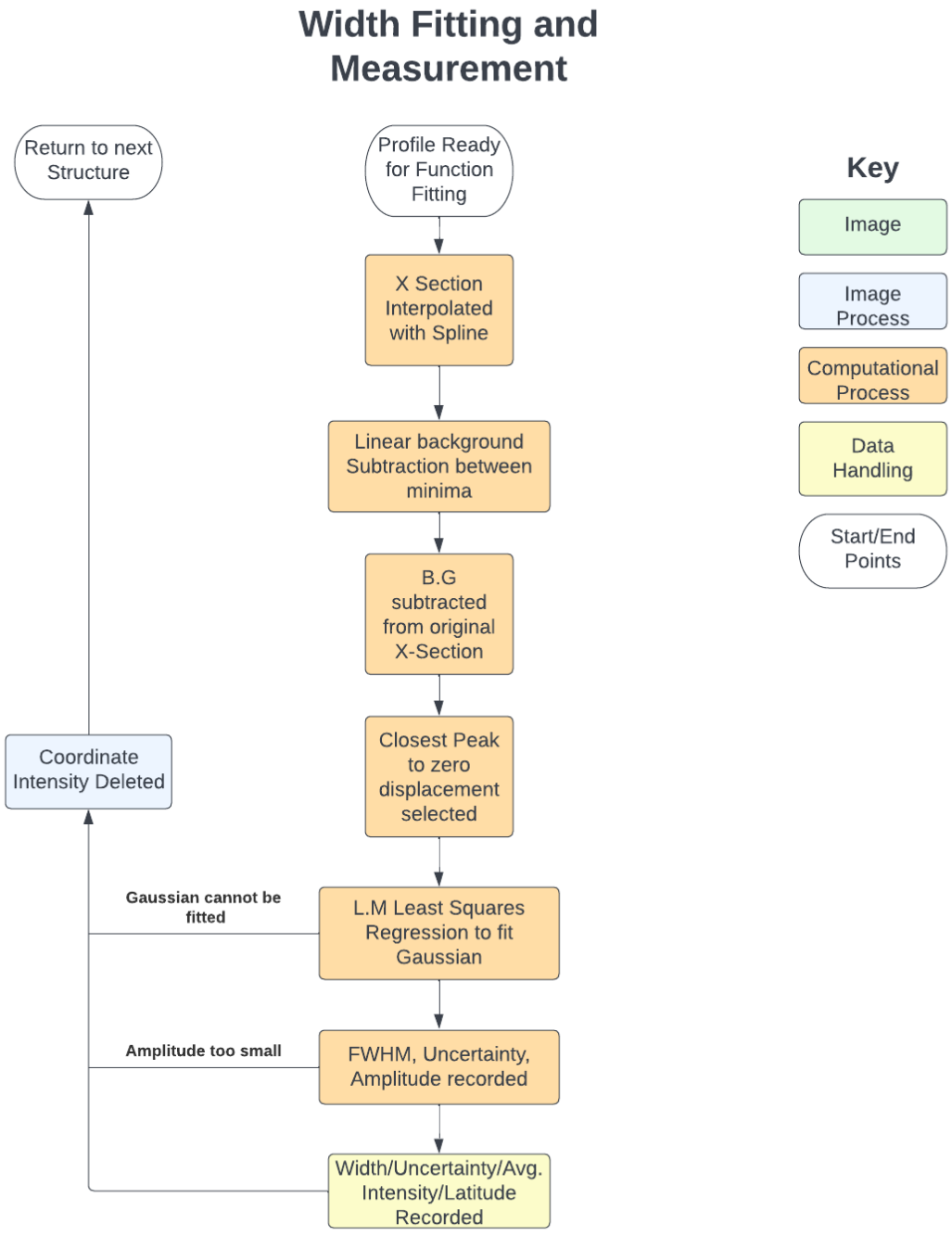

Figure 2: Workflow diagram of the Width Fitting element of the COSDA algorithm.

Bibliography

Aerts C., Christensen-Dalsgaard J., Kurtz D. W., 2010, Asteroseismology

Alfvén H., 1942, , 150, 405

Antonucci E., Harra L., Susino R., Telloni D., 2020, , 216, 117

Armstrong J. A., Fletcher L., 2019, Solar Physics, 294, 80

Aschwanden M., De Pontieu B., Katrukha E., 2013, Entropy, 15, 3007

Aschwanden M. J., 2010, Solar Physics, 262, 399

—, 2012, Astronomy and Astrophysics, 539, A2

Aschwanden M. J., 2016, The Astrophysical Journal Supplement Series, 224, 25

Aschwanden M. J., Aschwanden P. D., 2008, The Astrophysical Journal, 674, 544

Aschwanden M. J., Freeland S. L., 2012, The Astrophysical Journal, 754, 112

Aschwanden M. J., Lee J. K., Gary G. A., Smith M., Inhester B., 2008, Solar Physics, 248, 359

Aschwanden M. J., Peter H., 2017, The Astrophysical Journal, 840, 4

Asensio Ramos A., Díaz Baso C. J., 2019, Astronomy and Astrophysics, 626, A102

Astropy Collaboration et al., 2022, apj, 935, 167

—, 2018, , 156, 123

—, 2013, Astronomy and Astrophysics, 558, A33

Babcock H. W., 1961, The Astrophysical Journal, 133, 572

Bak P., Tang C., Wiesenfeld K., 1987, , 59, 381

—, 1988, Physical Review A, 38, 364

Bame S. J., McComas D. J., Barraclough B. L., Phillips J. L., Sofaly K. J., Chavez J. C., Goldstein B. E., Sakurai R. K., 1992, Astronomy and Astrophysicss, 92, 237

Barnes W. T. et al., 2020, Journal of Open Source Software, 5, 2801

Bell B., Glazer H. G., 1958, Smithsonian Contributions to Astrophysics

BenMoussa A. et al., 2013, Solar Physics, 288, 389

Beveridge C., Priest E. R., Brown D. S., 2004, Geophysical and Astrophysical Fluid Dynamics, 98, 429

Boe B., Habbal S., Druckmuller M., 2020, in AAS/Solar Physics Division Meeting, Vol. 52, AAS/Solar Physics Division Meeting, p. 210.03

Boerner P. et al., 2012, Solar Physics, 275, 41

Borovsky J. E., Denton M. H., 2006, Geophysical Research Letters, 33

Bradski G., 2000, Dr. Dobb's Journal of Software Tools

Bravo S., Stewart G. A., 1997, The Astrophysical Journal, 489, 992

Brooks D. H., Warren H. P., Landi E., 2021, The Astrophysical Journal, 915, L24

Carbonell M., Oliver R., Ballester J. L., 1993, Astronomy and Astrophysics, 274, 497

Carrington R. C., 1859, Monthly Notices of the Royal Astronomical Society, 20, 13

—, 1863, Observations of the Spots on the Sun: From November 9, 1853, to March 24, 1861, made at Redhill. Williams and Norgate

Chitta L. P. et al., 2022, Astronomy and Astrophysics, 667, A166

Clerk Maxwell J., 1865, Philosophical Transactions of the Royal Society of London Series I, 155, 459

Cliver, Edward W., Dietrich, William F., 2013, J. Space Weather Space Clim., 3, A31

Cranmer S. R., Winebarger A. R., 2019, Annual Review of Astronomy and Astrophysics, 57, 157

Dahlburg R. B., Einaudi G., Ugarte-Urra I., Rappazzo A. F., Velli M., 2018, The Astrophysical Journal, 868, 116

Darnel J. M. et al., 2022, Space Weather, 20, e2022SW003044

Dasi-Espuig M., Solanki S. K., Krivova N. A., Cameron R., Peñuela T., 2010, Astronomy & Astrophysics, 518, A7

de Ferrer J. J., 1809, Transactions of the American Philosophical Society, 6, 264

de Toma G., 2011, Solar Physics, 274, 195

DeForest C. E., Lamy P. L., Llebaria A., 2001, The Astrophysical Journal, 560, 490

Del Zanna G., Bromage B. J. I., Mason H. E., 2003, Astronomy and Astrophysics, 398, 743

Delaboudinière J. P. et al., 1995, Solar Physics, 162, 291

Domingo V., Fleck B., Poland A. I., 1995, Solar Physics, 162, 1

Dos Santos L. F. G. et al., 2021, Astronomy and Astrophysics, 648, A53

Eastwood J. et al., 2017, Risk analysis, 37, 206

Edlén B., 1943, , 22, 30

El-Borie M. A., Abdel-halim A. A., El-Monier S. Y., Bishara A. A., 2017, in Journal of Physics Conference Series, Vol. 869, Journal of Physics Conference Series, p. 012077

El-Borie M. A., El-Abshehy M., Talaat S., Taleb W. M. A., 2012, Astrophysics, 55, 127

Fabricius J., 1611, De maculis in sole observatis, et apparente earum cum sole conversione, narratio, cui adjecta est de modo eductionis specierum visibilium dubitatio. Laurentius Leuberlichius

Fraunhofer J., 1814, Memoirs of the Royal Academy of Sciences in Munich, 5, 193–226

Frercks J., Weber H., Wiesenfeldt G., 2009, Studies in History and Philosophy of Science Part A, 40, 143

Fu H., Xia L., Li B., Huang Z., Jiao F., Mou C., 2014, The Astrophysical Journal, 794, 109

Galilei G., Drake S., 1990, Discoveries and opinions of Galileo : including The starry messenger (1610), Letter to the Grand Duchess Christina (1615), and excerpts from Letters on sunspots (1613), The assayer (1623)

García Marirrodriga C. et al., 2021, Astronomy and Astrophysics, 646, A121

Garriott O. K., 1974, Science, 186, 219

Gburek S., Sylwester J., Martens P., 2006, Solar Physics, 239, 531

Grigis P., Su Y., Weber M., 2012, Aia psf characterization and image deconvolution

Grotrian W., 1939, Naturwissenschaften, 27, 214

Gruenwald A., 1887, Chemical News, 56, 232

Hale G. E., Nicholson S. B., 1925, The Astrophysical Journal, 62, 270

Handy B. N. et al., 1999, Solar Physics, 187, 229

Harris C. R. et al., 2020, Nature, 585, 357

Hathaway D., 2005

Hathaway D. H., 2015, Living Reviews in Solar Physics, 12, 4

Hathaway D. H., Wilson R. M., 2006, , 33, L18101

Hewins I. M., Gibson S. E., Webb D. F., McFadden R. H., Kuchar T. A., Emery B. A., McIntosh S. W., 2020, Solar Physics, 295, 161

Heyvaerts J., Priest E., 1984, Astronomy and astrophysics, 137, 63

Higginson A. K., Antiochos S. K., DeVore C. R., Wyper P. F., Zurbuchen T., 2017, The Astrophysical Journal, 837, 113

Higginson A. K., Antiochos S. K., DeVore C. R., Wyper P. F., Zurbuchen T. H., 2017, The Astrophysical Journal, 837, 113

Hoyt D. V., Schatten K. H., 1998, Group Sunspot Numbers: A New Solar Activity Reconstruction. Solar Physics, v. 181, Issue 2, p. 491-512 (1998).

Hurlburt N. et al., 2012, Solar Physics, 275, 67

Inoue S., Kusano K., Büchner J., Skála J., 2018a, Nature Communications, 9, 174

—, 2018b, Nature Communications, 9, 174

Ise R., Cagle E. H., 1974, Acta Astronautica, 1, 1315

Ivanov V. G., Miletsky E. V., 2014, Geomagnetism and Aeronomy, 54, 907

Javaraiah J., 2021, , 366, 16

Joshi B., Bhattacharyya R., Pandey K. K., Kushwaha U., Moon Y.-J., 2015, Astronomy and Astrophysics, 582, A4

Kanella C., Gudiksen B. V., 2019, Astronomy and Astrophysics, 621, A95

Klimchuk J., Deforest C., 2020, The Astrophysical Journal, 900, 167

Klimchuk J. A., DeForest C. E., 2020, The Astrophysical Journal, 900, 167

Kobayashi K. et al., 2014, Solar Physics, 289, 4393

Kosugi T. et al., 2007, Solar Physics, 243, 3

Kramer H. J., 2012a, Sdo satellite mission overview, https://www.eoportal.org/satellite-missions/sdo

—, 2012b, Soho satellite mission overview, https://www.eoportal.org/satellite-missions/soho

Kuckein C., Centeno R., Martínez Pillet V., Casini R., Manso Sainz R., Shimizu T., 2009, Astronomy and Astrophysics, 501, 1113

Lam S. K., Pitrou A., Seibert S., 2015, in Proceedings of the Second Workshop on the LLVM Compiler Infrastructure in HPC, pp. 1–6

Lavasa E., Giannopoulos G., Papaioannou A., Anastasiadis A., Daglis I. A., Aran A., Pacheco D., Sanahuja B., 2021, Solar Physics, 296, 107

Lehtinen J., Munkberg J., Hasselgren J., Laine S., Karras T., Aittala M., Aila T., 2018, arXiv e-prints, arXiv:1803.04189

Leighton R. B., 1969, The Astrophysical Journal, 156, 1

Lemen J. R. et al., 2012a, Solar Physics, 275, 17

—, 2012b, Solar Physics, 275, 17

Levenberg K., 1944, Quart. Appl. Math., 2, 164

Liu J., Nelson C. J., Snow B., Wang Y., Erdélyi R., 2019, Nature Communications, 10, 3504

Lockyer J. N., 1879, Proceedings of the Royal Society of London, 29, 140

López Fuentes M. C., Klimchuk J. A., Mandrini C. H., 2007, The Astrophysical Journal, 657, 1127

Madjarska M. S., 2019, Living Reviews in Solar Physics, 16, 2

Maunder E. W., 1904, , 64, 747

McAteer R. T. J., Aschwanden M. J., Dimitropoulou M., Georgoulis M. K., Pruessner G., Morales L., Ireland J., Abramenko V., 2016, , 198, 217

McComas D. J., Angold N., Elliott H. A., Livadiotis G., Schwadron N. A., Skoug R. M., Smith C. W., 2013, The Astrophysical Journal, 779, 2

McIntosh S. W., Leamon R. J., Egeland R., 2023, Frontiers in Astronomy and Space Sciences, 10

Mercier C., Chambe G., 2015, Astronomy and Astrophysics, 583, A101

—, 2016, Astronomy and Astrophysics, 585, C1

Mikić Z., Lionello R., Mok Y., Linker J. A., Winebarger A. R., 2013, The Astrophysical Journal, 773, 94

Milano L. J., Gómez D. O., Martens P. C. H., 1997, The Astrophysical Journal, 490, 442

Millochau G., Stefánik M., 1906, The Astrophysical Journal, 24, 42

Morgan H., Druckmüller M., 2014, Solar Physics, 289, 2945

Morgan H., Korsós M. B., 2022, The Astrophysical Journal, 933, L27

Moriyasu S., Kudoh T., Yokoyama T., Shibata K., 2004, The Astrophysical Journal, 601, L107

Müller D., Marsden R. G., St. Cyr O. C., Gilbert H. R., Solar Orbiter Team, 2013, Solar Physics, 285, 25

Müller D. et al., 2020a, Astronomy and Astrophysics, 642, A1

—, 2020b, Astronomy and Astrophysics, 642, A1

Mumford S. et al., 2020, Journal of Open Source Software, 5, 1832

Nair S., Nayar S., 2008, Indian Journal of Radio and Space Physics, 37

Nakariakov V. M., Kolotkov D. Y., 2020, Annual Review of Astronomy and Astrophysics, 58, 441

Nath B. B., 2012, The story of helium and the birth of astrophysics. Springer Science & Business Media

Oliver R., Ballester J., 1993, Astronomy and Astrophysics, 274, 497

Owens M. J., Lockwood M., Barnard L. A., Scott C. J., Haines C., Macneil A., 2021, Solar Physics, 296, 1

Pesnell W. D., Thompson B. J., Chamberlin P. C., 2012, Solar Physics, 275, 3

Peter H., Bingert S., Kamio S., 2012, Astronomy and Astrophysics, 537, A152

Peter H. et al., 2013, Astronomy and Astrophysics, 556, A104

Peter H., Dwivedi B. N., 2014, Frontiers in Astronomy and Space Sciences, 1

Poduval B., DeForest C. E., Schmelz J. T., Pathak S., 2013, The Astrophysical Journal, 765, 144

Poduval B., DeForest C. E., Schmelz J. T., Pathak S., 2013, The Astrophysical Journal, 765, 144

Poletto G., 2015, Living Reviews in Solar Physics, 12, 7

Pucci S., Poletto G., Sterling A. C., Romoli M., 2014, The Astrophysical Journal, 793, 86

Rappazzo A. F., 2015, The Astrophysical Journal, 815, 8

Reale F., 2014, Living Reviews in Solar Physics, 11, 4

Reale F., Orlando S., Guarrasi M., Mignone A., Peres G., Hood A. W., Priest E. R., 2016, The Astrophysical Journal, 830, 21

Ring E. F. J., 2000, The Imaging Science Journal, 48, 1

Rochus P. et al., 2020, Astronomy and Astrophysics, 642, A8

Scherrer P. H. et al., 2012, Solar Physics, 275, 207

Schou J. et al., 2012, Solar Physics, 275, 229

Schove D. J., Peng-Yoke H., 1967, Journal of the American Oriental Society, 87, 105

Schwabe H., 1844, Astronomische Nachrichten, 21, 233

Seaton D. B. et al., 2021, Nature Astronomy, 5, 1029

Sharma A. S., Aschwanden M. J., Crosby N. B., Klimas A. J., Milovanov A. V., Morales L., Sanchez R., Uritsky V., 2016, , 198, 167

Shih F., Jing J., Qu M., Wang H., 2008, SCIENTIA SINICA Physica, Mechanica Astronomica

SILSO World Data Center, 2010-2020, International Sunspot Number Monthly Bulletin and online catalogue

Silverman, Sam M., Hayakawa, Hisashi, 2021, J. Space Weather Space Clim., 11, 17

Soon W., Yaskell S., 2003, The Maunder Minimum and the Variable Sun-Earth Connection

Stern R. A., Haisch B. M., Joki E. G., Catura R. C., 1984, in Society of Photo-Optical Instrumentation Engineers (SPIE) Conference Series, Vol. 445, Instrumentation in astronomy V, Boksenberg A., Crawford D. L., eds., pp. 347–357

The SunPy Community et al., 2020, The Astrophysical Journal, 890, 68

Török T., Kliem B., 2003, , 406, 1043

van Driel-Gesztelyi L., Green L. M., 2015, Living Reviews in Solar Physics, 12, 1

Vaquero J. M., Gallego M. C., García J. A., 2002, Geophysical Research Letters, 29, 58

Švestka Z., Uchida Y., ????

Wang J., Yan X., Xue Z., Yang L., Li Q., Chen H., Xia C., Liu Z., 2022, Astronomy and Astrophysics, 659, A76

Wang Y. M., Warren H. P., Muglach K., 2016, The Astrophysical Journal, 818, 203

Watkins N. W., Pruessner G., Chapman S. C., Crosby N. B., Jensen H. J., 2016, , 198, 3

Watson F. T., Fletcher L., Marshall S., 2011, Astronomy and Astrophysics, 533, A14

Wilhelm K. et al., 2011, Astronomy and Astrophysicsr, 19, 35

Williams D. R., 2022, NASA Science Data Coordinated Archive

Williams T., Walsh R. W., Peter H., Winebarger A. R., 2020a, The Astrophysical Journal, 902, 90

Williams T., Walsh R. W., Regnier S., Johnston C. D., 2021, Solar Physics, 296, 102

Williams T. et al., 2020b, 892, 134

—, 2020c, The Astrophysical Journal, 892, 134

Woods T. et al., ????, The solar dynamics observatory, 115

Xie H., Madjarska M., Li B., Huang Z., Xia L., Wiegelmann T., Fu H., Mou C., 2017, The Astrophysical Journal, 842

Xie H., Madjarska M. S., Li B., Huang Z., Xia L., Wiegelmann T., Fu H., Mou C., 2017, The Astrophysical Journal, 842, 38

Xie J., Shi X., Qu Z., 2018, The Astrophysical Journal, 855, 84

Xu Z.-t., 1980, Chinese Astronomy, 4, 406

Yeates A. R., Nandy D., Mackay D. H., 2008, The Astrophysical Journal, 673, 544

Zharkov S., Zharkova V. V., Ipson S. S., 2005, Solar Physics, 228, 377

Zhiming S., Xiaoli Y., Zhongquan Q., Hong-Bo L., 2019, , 490, 5567